# Metal Complexes for Organic Optoelectronic Applications

by

Liang Huang

A Dissertation Presented in Partial Fulfillment
of the Requirements for the Degree
Doctor of Philosophy

Approved June 2017 by the
Graduate Supervisory Committee:

Jian Li, chair
James Adams
Terry Alford

ARIZONA STATE UNIVERSITY

August 2017

ABSTRACT

Organic optoelectronic devices have drawn extensive attention by over the past two decades. Two major applications for Organic optoelectronic devices are efficient organic photovoltaic devices(OPV) and organic light emitting diodes (OLED). Organic Solar cell has been proven to be compatible with the low cost, large area bulk processing technology and processed high absorption efficiencies compared to inorganic solar cells. Organic light emitting diodes are a promising approach for display and solid state lighting applications. To improve the efficiency, stability, and materials variety for organic optoelectronic devices, several emissive materials, absorber-type materials, and charge transporting materials were developed and employed in various device settings. Optical, electrical, and photophysical studies of the organic materials and their corresponding devices were thoroughly carried out. In this thesis, Chapter 1 provides an introduction to the background knowledge of OPV and OLED research fields presented. Chapter 2 discusses new porphyrin derivatives- azatetrabenzylporphyrins for OPV and near infrared OLED applications. A modified synthetic method is utilized to increase the reaction yield of the azatetrabenzylporphyrin materials and their photophysical properties, electrochemical properties are studied. OPV devices are also fabricated using Zinc azatetrabenzylporphyrin as donor materials. Pt(II) azatetrabenzylporphyrin were also synthesized and used in near infra-red OLED to achieve an emission over 800 nm with reasonable external quantum efficiencies. Chapter 3, discusses the synthesis, characterization, and device evaluation of a series of tetradentate platinum and palladium complexesfor single doped white OLED applications and RGB white OLED applications. Devices employing some of the developed emitters demonstrated impressively high

external quantum efficiencies within the range of 22%-27% for various emitter concentrations. And the palladium complex, i.e. Pd3O3, enables the fabrication of stable devices achieving nearly 1000h. at 1000cd/$m^2$ without any outcoupling enhancement while simultaneously achieving peak external quantum efficiencies of 19.9%. Chapter 4 discusses tetradentate platinum and palladium complexes as deep blue emissive materials for display and lighting applications. The platinum complex PtNON, achieved a peak external quantum efficiency of 24.4 % and CIE coordinates of (0.18, 0.31) in a device structure designed for charge confinement and the palladium complexes Pd2O2 exhibited peak external quantum efficiency of up to 19.2%.

ACKNOWLEDGMENTS

I would like to thank my advisor, Dr. Jian Li for providing the opportunity to work on such interesting projects and my committee members Dr. James Adams and Dr. Terry Alford. I would also like to thank the chemists, for the exchanging of ideas and giving me advices on the projects: Dr. Zixing Wang, Dr. Guijie Li, Dr. Zhiqiang Zhu, Dr. Eric Turner, Alicia Wolf, Dr. Lele Wen, Dr. Yunlong Ji, and Dr. Xiaochun Hang. I would also like to thank the wonderful device engineers who helped me fabricate devices and gave me valuable material input: Dr. Tyler Fleetham, Dr. Nathan Bakken, Dr. Jeremy Ecton, Dr. Choong Do Park, Gregory Norby, Kody Klimes, Dr. Barry O'Brien. Finally, I would like to thank my friends and family for their support and in particular my wife for her unlimited patience and words of encouragement.

TABLE OF CONTENTS

Page

CHAPTER Page

LIST OF TABLES

Table Page

LIST OF FIGURES

Figure Page

Figure Page

Figure Page

Figure Page

Figure Page

Figure Page

Figure Page

Figure Page

Figure Page

Figure Page

Figure Page

# CHAPTER 1

# INTRODUCTION

## 1.1 Organic Photovaltaics

In 1839, Edmund Bequerel firstly observed photocurrent by illuminating a silver coated platinum electrode immersed in electrolyte, which is well-known as the photovoltaic effect. In the following several years, researchers are focused on selenium based solar cells until the development of high quality silicon wafers in the 1950s. With the discovery of manufacturing p-n junction silicones, Chapin, Fuller and Pearson pioneered the work of development of the first silicon solar cell in 1954[1], with a efficiency of 6%. And silicon solar cells were firstly commercialized in 1960s for space program applications[2.]

With the awareness of the energy limit and the concerns on pollution of the conventional energies sources, the develetment of renewable energies becomes more and more desireable. Solar energy, which is inexhaustible and environmentally clean, has becoming first choice to replace conventional energies. In the past half century, great efforts have been put on the development of solar cells and significant result has been made. As illustrated in Figure 1. power conversion efficiencies as high as 25.0±0.5% for crystalline silicon cells, 29.1±0.8% for III-V (GaAs) semiconductor cells, and 13.6±0.3% for amorphous silicon devices have been reported and verified by independent test centers[3].However even if crystalline silicon solar cells have nearly reached the theoretical maximum efficiencies, and dramatic reduction in costs over the past few decades, solar cells

are still more expensive than the conventional source of electricity.

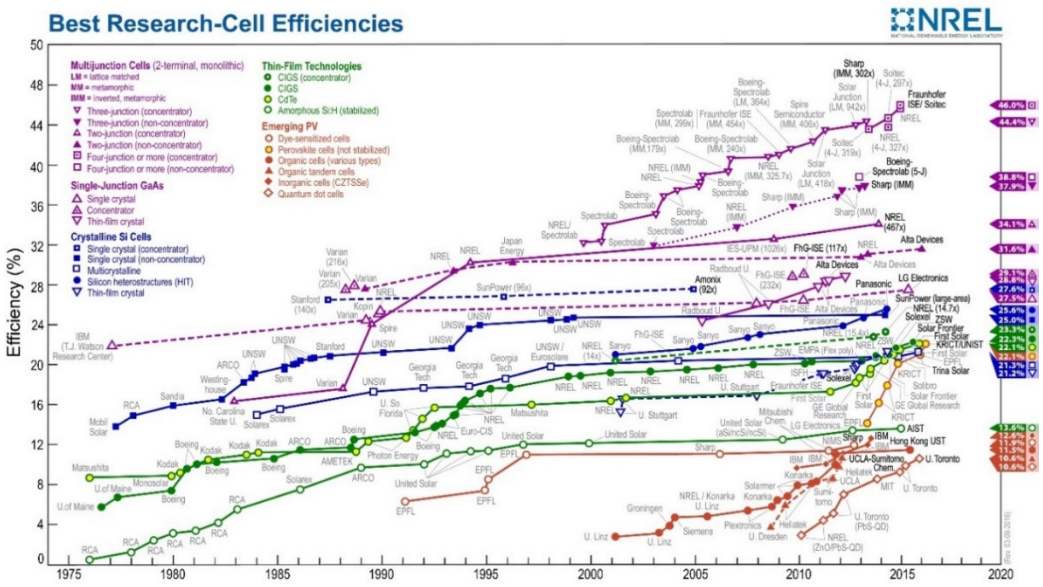


Figure 1 Record research solar cell efficiencies[3].

Organic photovoltaic (OPV), on the other hand has the ability to be produced cheaply in high volumes, has attracted more and more arrentions over the past 20 years. Significant improvement by utilizing conjugated organic molecules for photovoltaic applications has been made. Several companies have developed their own OPV products with decent efficiencies (Figure 2).

(a)  (b) 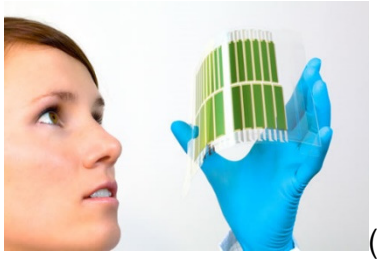 (c) 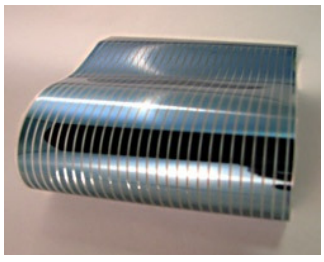

Figure 2 Photos of (a) organic thin-film solar cell modules developed by konarka(5). (b) organic solar cells developed by Heliatek and (c) polymer based solar cell by Solarmer

There are two processing techniques for OPV devices: 1) thermal evaporation for planar bilayer device (PHJ) and bulk-heterojunction (BHJ) device and 2) solution processing (spin-coating, inkjet printing, dip-coating, spraying technique) for BHJ solar cell devices (Figure 3). Because the interfacial area between donor and acceptor layers for the planar bilayer devices is limited and the exciton diffusion length ($L_D$) in these materials is usually up to several orders of magnitude smaller than the absorption penetration depth, only excitons generated at the interface can be separated into free charge carriers [4]. Therefore, the thickness of the D–A layers in these cells is limited to the regime of the exciton diffusion length $L_D$. Bulk-heterojunction (BHJ) device circumvented this problem by blending of donor and acceptor molecules and creating nanoscale phase separation[5,6].

BHJ solar cells are composed of a blend film of a conjugated polymer or a small molecule as donor and a soluble fullerene derivative as acceptor sandwiched between an Indium tin oxide (ITO) anode and a low-work-function metal cathode. The interfacial area (photocurrent generation region) between the active materials is greatly enlarged, thus increased the charge dissociation.

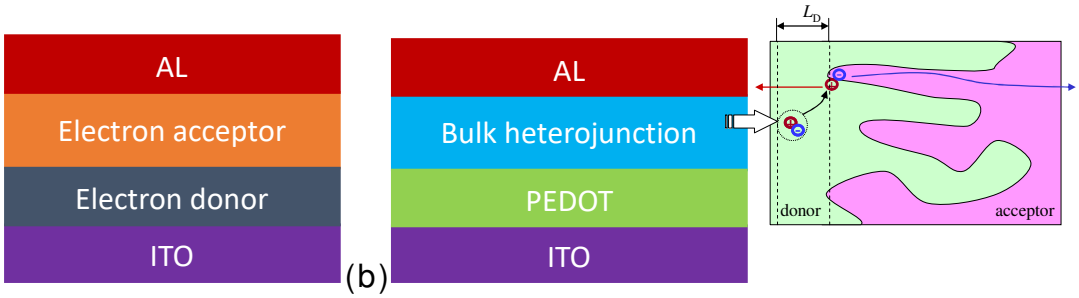


Figure 3 Schmatic illustration of structures of (a) Planar or bilayer OPV device, (b) Bulk-heterojunction OPV device.

## 1.2 Organic solar cell operation

In general, the organic solar cell works in five processes (Figure4): 1. Absorption of light and generation of excitons, 2. Excitons Diffusion, 3. Charge separation, 4. Charge transport, 5. Charge collection.

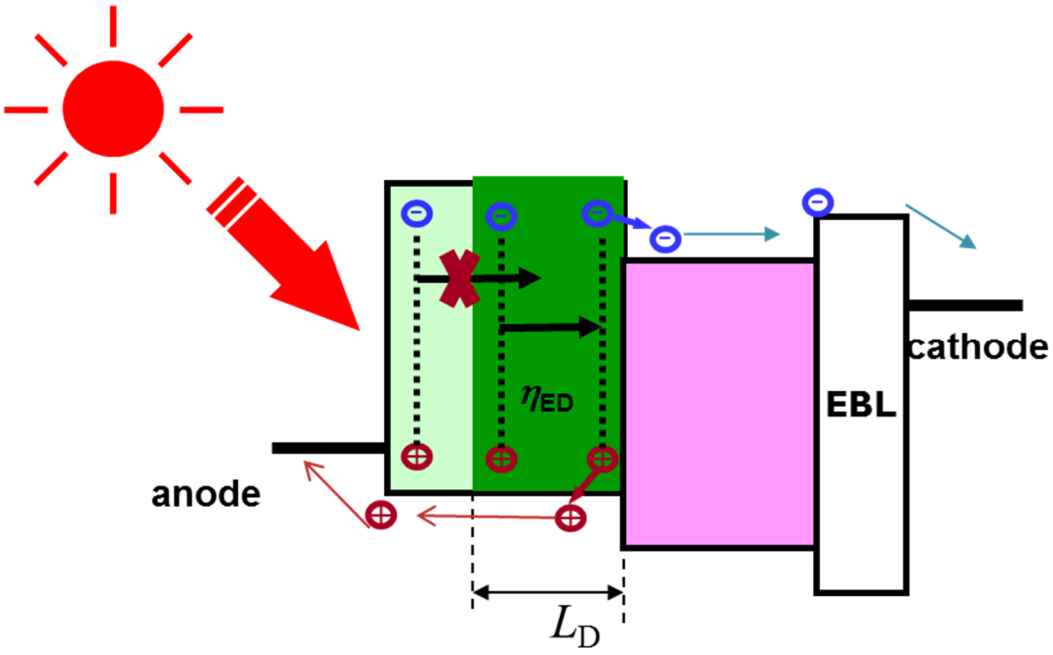


Figure 4 Schematic illustration of operational process inside of the organic solar cells

### 1.2.1 Light absorption

Light absorption is the first step of OPV operation, when light was absorbed by the OPV device, excitons are formed and diffused to the interface of the Donor and acceptor layer. So the absorption spectrum of the photoactive organic layer should overlap the solar emission spectrum as much as possible in order to harvest more light. Also the absorbing layer should be sufficiently thick to absorb most of the incident light. Generally the optical absorption coefficient (α) of organic materials is much higher than that of

crystalline or multicrystalline silicon. For example, zinc phthalocyanine (ZnPc) Solution which is commonly used in bilayer solar cell devices, has a α exceeds $1\times10^5 cm^{-1}$ (Figure 5)

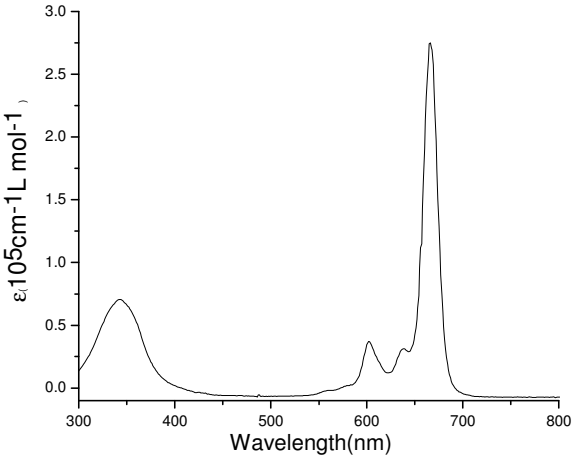


Figure 5 Absorption spectrum of ZnPC in a solution of THF at room temperature.

1.2.2 Exciton transport

Unlike inorganic solar cells which directly forms electrons and holes, excitons are formed in organic solar cells. [7] Ideally, all excitons should transport to the the interface of the active lalyers and form free charge. However there are other competitive decay processes, such as luminescence or radiative recombination to the ground state in the process of exciton transport. $\tau_{EXC}$, the exponential lifetime of an exciton, is determined by the reciprocal value of all radiative and non radiative decay rates together. For an efficient solar cell device, all excitons have to reach the photo-active interface within $\tau_{EXC}$. The exciton dissuion length, $L_D$, is given by: [8]

$$L_D = \sqrt{D_{EXC}\tau_{EXC}}$$

In which $D_{EXC}$ is the diffusion coefficient of the excitons. Since $\tau_{EXC}$ is usually very short for molecular materials, usually only several nanoseconds, $L_D$ is generally limited to 10 nm. In this case, only those excitons formed within the distance of $L_D$ from the interface will contribute to charge separation. Therefore, materials with longer diffusion coefficient of excitons and higher aborption coefficent are desired.

1.2.3 Charge separation

Once the excitons reached the interface of the active layers, charges are created by photoinduced electron transfer. [9] In this process an electron is transferred from an electron donor (D) material to an electron acceptor (A) material with the aid of the additional input energy of an absorbed photon. Electron donor materials usually have lower electron affinity compared with electron acceptors materials. The difference between the electron affinity levels between donor and acceptor materials forms the driving force for the exciton dissociation. In the photoinduced electron transfer process a donor (D•+) and a radical anion of the acceptor (A•-) are formed with the decay of an exciton at the D/A interface.

$$D + A + h\nu \rightarrow \quad D^* + A \quad (\text{or } D + A^*) \rightarrow \quad D^{\bullet+} + A^{\bullet-}$$

There are competitive processes during the charge separation, such as fluorescence or non-radiative decay, the charge-separated state should be the thermodynamically and kinetically favorable pathway for the exciton in order to get an efficient charge generation.

1.2.4 Charge transport

After the charge separation process, mobile charge carriers(electrons and holes) can be transported to the electrodes either by carrier diffusion or electric field induced drift. In order to get efficient charge collection, the charge carrier transit time should be much shorter than the carrier life time. [10]The carrier transit time is determined by charge carrier mobility μ, sample thickness d, and the electric field E inside the film. Impurities in the material will act as traps and kill the charges. Therefore, the development of both high mobility and high purity materials is anticipated for efficient charge transport.

### 1.2.5 Charge collection

Charge carriers are collected at the electrodes. Normally there is a transparent conductive oxide (TCO) usually ITO as anode on one side and a metal contact on the other side as cathode.

## 1.3 Parameters of solar cells.

Current-voltage (J–V) curve is a direct characterization method of a solar cell. Figure 6 shows a J–V curve under dark and incident-light illumination. There are three important parameters shown in the J-V curve: the open circuit voltage (Voc), the short circuit current density (Jsc) and the fill factor (FF). In order to obtain high performance of the solar cells, each of these parameters need to be optimized.

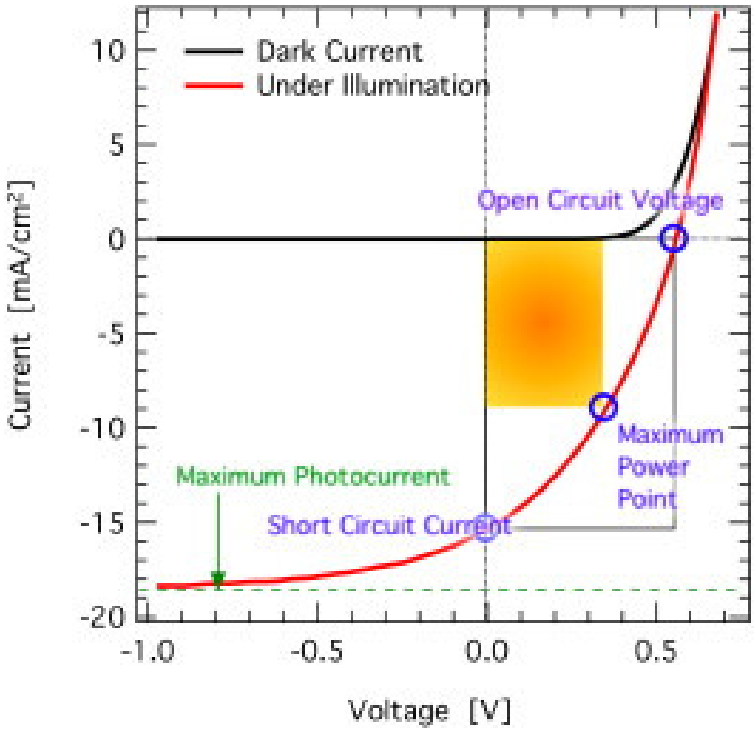


Figure 6 typical J-V curve of OPV devices in dark current or under illumination.

1.3.1 Power conversion efficiency

The power conversion efficiency η of solar cells is defined as

$$\eta = \frac{FF * Voc * Jsc}{Pinc}$$

Where FF is the fill factor, Voc the open circuit voltage, Jsc the short circuit current density and Pinc is the power density of the incident light.

1.3.2 Open-Circuit Voltage (Voc)

Voc is defined as the maximum possible voltage across a photovoltaic cell; the voltage across the cell in sunlight when no current is flowing.

The value of $V_{OC}$ can be expressed by the empirical equation:

$$V_{OC} = e^{-1} \times (|E_{HOMO\ donor}| - |E_{LUMO\ acceptor}| - 0.3eV)$$

Where e is the elementary charge, E is the energy level and 0.3 eV is an empirical value for efficient charge separation[11]. From the equation, Voc can be increased ether by lowering HOMO level of the donor material or increasing the LUMO level of the acceptor material.

The non-radiative recombination between the donor and the acceptor also affects Voc. In order to obtain a maximized Voc, these non-radiative pathways need to be eliminated. [12]

### 1.3.3 Short-Circuit Current Density (Jsc)

Short-Circuit Current Density (Jsc) – This is the current density that flows through an illuminated solar cell when there is no external resistance. The short-circuit current is the maximum current that a device is able to produce. Under an external load, the current density will always be less than Jsc.

$J_{SC}$ is another important parameter that determines the performance of a OPV device. The common strategy for achieving high $J_{SC}$ is to broader the absorption to cover more solar light by narrowing the bandgap of the materials [13] [14]. However, bandgap cannot be extremely lowered because the energy levels also affect Voc. Therefore, a bandgap between 1.3 eV to 1.8 eV is anticipated. The formed charges will not contribute to the photocurrent if they cannot reach the electrodes within the carrier life time. In this case, charge mobility of the material is also very important for higher Jsc.

### 1.3.4 Fill Factor (FF)

Fill Factor (FF) – The ratio of the actual maximum power output and the product of Isc and Voc.

The formula for FF in terms of the above quantities is:

$$FF = \frac{I_{mpp}V_{mpp}}{I_{SC}V_{OC}}$$

FF is affected by many factors, including charge carrier mobility and balance, interface recombination, series and shunt resistances, film morphology and miscibility between the donor and acceptor[15]. From the materials design point of view, planar molecular with good molecular packing and high mobility should be taken into consideration.

## 1.4 Organic solar cell materials

### 1.4.1 Acceptor materials:

The active layer in an organic solar cells device includes two kind of materials: donor material and an acceptor material. Fullerene and its derivatives, C60 and PCBM for example (Figure 7), are common acceptors because of their high electron mobility, good thermal stability, etc. C60 can only processed by vapor deposition method because of its poor solubility. PCBM is soluble in common solvents and so can be used in solution processed devices. In the recent years, $PC_{70}BM$ was also investigated as acceptor material because of its higher lying LUMOs and better absorption [16-18].

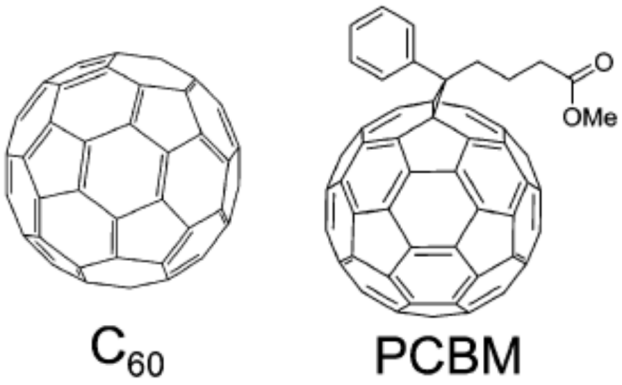


Figure 7 Structure of commonly used acceptor materials

1.4.2 Donor materials

Compared with acceptor materials, donor materials are more diversified, There are several catigories of donor materials and each catigory has thousands of different material designs. Theriefore, much more attention has been applied on the design and synthesis of new donor materials from researchers. Significant improvement has been achieved in the past several years.

Phthalocaynine (Pc), comprising four isoindole units connected by 1,3-aza linkages, is a planar and highly aromatic 18-π-electron macro cycle. Pc derivatives typically exhibit high charge mobility, high absorption coefficient, and excellent thermal. CuPc [19 20], PdPC[21] and ZnPc[22, 23] have been the most common choices to date for application in Pc-based OPV devices, due to longer exciton diffusion length compared to the other Phthalocaynines.

The first organic solar cell was first present by Tang and Albrecht by using microcrystaling chlorophyll-a sandwiched by two metal electrodes, a PCE of 0.001% was achieved [23]. The reason why single layer device has lower PCE is that the exciton dissociation requires a very high applied field (more than 106 $Vcm^{-1}$). [24] In order to circumvent this problem, Tang first introduced bilayer devices using Cu phthalocynine as donor material and perylene-3, 4, 9, 10-bis-benzimidazole (PTCBI) as the acceptor material in 1986, and 0.95% in PCE was obtained

. As the limited donor and acceptor interface, bilayer devices must be very thin to insure the efficient exciton transportation as well as charge separation. A BHJ OPVs based on a mixture of vacuum codeposited CuPc and C60 were fabricated to solve that problem. A PCE up to 3.5% was achieved with the BHJ devices [25]. Later, Forrest et al. fabricated a planar-mixed heterojunction (PMHJ) device in which a mixed layer consisting of CuPc and C60 sandwiched between homogeneous CuPc and C60 layers, and the device afforded a maximum PCE of 5.0%.[26] By fitting the measured EQE to the simulated EQE values using a transfer matrix model, Kim et al. investigated the exciton diffusion length ($L_D$) of Phthalocaynines with different metals with a MPC as donor material and PTCBI as acceptor. $L_D$ values with 5.8, 6.2, 10.1, and 5.6 nm for CuPc, ZnPc, PdPc, and PtPc were estimated.[22]

One of the disadvantages of Phthalocaynines based materials is the high HOMO energy level, which leads to a small Voc (usually 0.5 eV to 0.6 eV). In order to solve this problem, novel Phthalocaynines derivatives with lower HOMO level were sdeveloped. Thompson et al. utilized boron subphthalocyanine chloride(SubPC) which has a much

deep HOMO (-5.6eV) as donor materials and the bilayer deveices with ITO/SubPc /C60 /BCP/Al structure obtained 2.1% PCE with a Voc value of as high as 0.98 eV[27]. By attaching high electron withdrawing fluorine atom to the Phthalocaynines, Meiss et al. fabricated a p-i-n inverted device with $F_4$ZnPC as donor material and C60 as accetor material and a Voc of 0.73eV was achieved with a PCE of 3.6%[28].

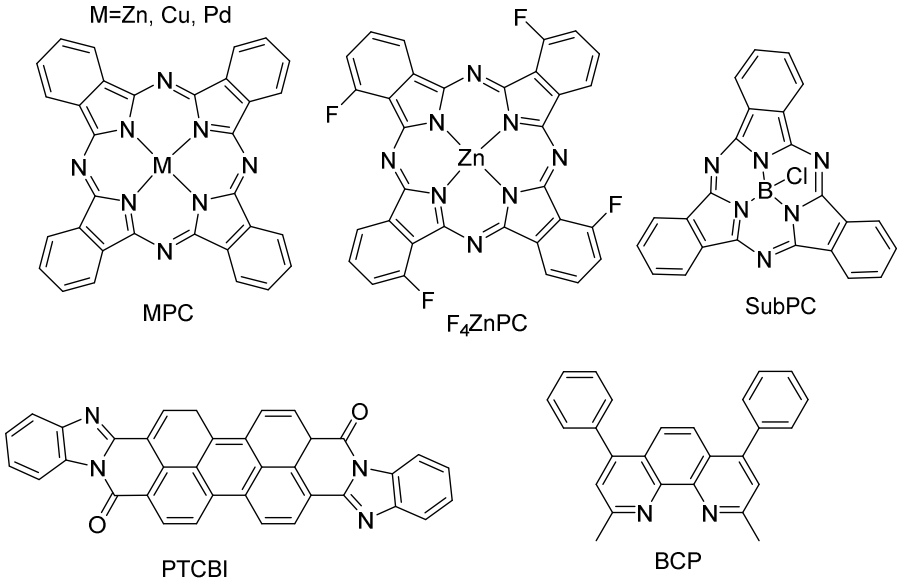


Figure 8 Chemical structures of some molecular absorbers used in vapor deposion PV devices

1.5 Organic light emitting devices (OLEDs)

Organic electroluminescent materials have attracted interest from researchers and electronics manufacturers as potential next generation energy efficient displays and solid state lighting for their benefits of potentially low fabrication cost, high energy efficiency, and the ability to be fabricated in several different form factors on various substrates.

OLEDs have successfully ustilized in high quality smart phones, televisions, monitors, digital cameras, tablet computers, and lighting fixtures [29] Research on material and device design is onging to obtain higher efficient, more affordable, and better performance OLED products. The direct emission process of OLEDs means displays can have lower power consumption, increased contrast, thinner form factors, faster refresh times, and brighter colors.

(a)


(b)


(c)

Figure 9 (a) Flexible OLED roadmap posted by LG Display, pictures of (b) LG OLED TV and (c) Samsung's OLED smartphone

In 1987 Tang et al.[30] reported a ground breaking structure which used indium tin oxide (ITO) as the hole injection electrode, 1,1-bis[di(tolyl)aminophenyl] cyclohexane (TAPC) as a hole transport layer (HTL), tris(8-hydroxyquinolinato) aluminium ($Alq_3$) as the

combined electron transport layer (ETL) and emissive layer (EML), and a magnesium/gold electron injection electrode. The work was significant in several respects. The advent of unipolar TPAC as the HTL allowed for efficient hole transport, as well the blocking of electrons from $Alq_3$. The device was also composed of amorphous films that were 50-100 nm thick, which improved the power efficiency significantly while maintaining conformal coverage. The Au/Mg electrode was significantly more stable that previously reported ones made of more reactive metals. The resulting devices had an EL quantum efficiency of 1%, luminous efficiency of 1 lm/W, and lifetimes around 100 hours. In 1990 Burroughes et al. followed Tang's work and used poly(p-phenylene vinylene) (PPV) as emiting material , producing the first polymer light-emitting diodedevices with EL quantum efficiencies of 8%.[31]

1.5.1 OLED device operation

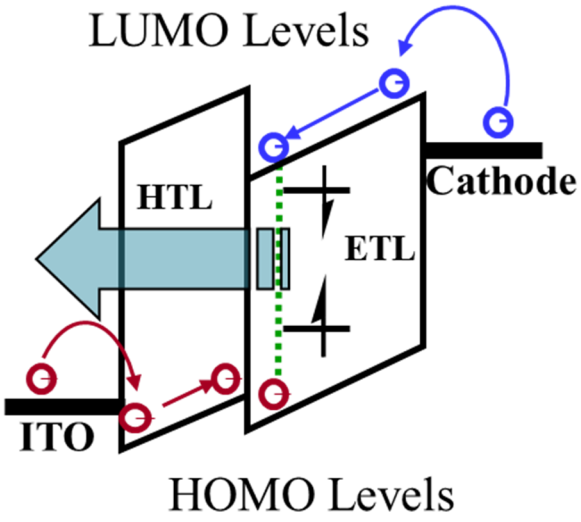


Figure 10.Scehmatic illustration of operation processes inside of OLED devices.

The typical operation of an OLED is shown in Figure 10. After a forward bias is applied, electrons and holes are injected over a small energetic barrier into hole transport and electron transporting layers. Hole injection occurs when one electron is removed from the HOMO of hole-transporters, resulting in a positively charged radical cation. Similarly, the electron transport layer (ETL) is expected to transport electrons from the cathode. The electron transport process adds one electron into the LUMO of electron-transporters, making the ETL molecule a negatively charged radical anion. The HOMO energy is related to the ionization potential and solution oxidation potential, and the LUMO energy is related to the electron affinity and solution reduction potential. Due to differences in charge mobility and the presence of energetic barriers, charges usually build up along the interface of the emissive layer and one of the transport materials. Once a Hole and an electron reach each other, they will form a localized coulombically bound excited state called a Frenkel exciton. The statistical distribution of excitons will be 25% singlets and 75% triplets. The formed excitons can either recombine radiatively, recombine non radiatively, or can transfer its energy to another molecule. The transport of excitons can either occur as a coincident electron and hole exchange with a neighboring molecule or via a long range mechanism, called Förester resonant energy transfer.[32] If the emission energy of a molecule has significant spectral overlap with the absorption spectrum of another molecule, a dipole coupling between the two molecules may occur and a long range radiationless energy transfer process may occur on length scales of the order 10-100Å.[33] Such is commonly the case for transfer of energy from a high bandgap host to a lower bandgap dopant molecules. Consequently, nearly exclusive emission can be achieved from a dopant molecule even at doping concentration of 1% or lower. Upon

localization on the dopant molecule, the emitter can through either fluorescence or phosphorescence process, can transfer its energy to another dopant, or can be quenched by impurities. Therefore, it is very imporant to make sure no impurities or lower energy species are present so that the primary recombination pathway will be through emission from the selected dopant molecule.

### 1.5.2 Solid state lighting

With the rising of efficiency and stability of white OLEDs, they began to be considered as potential candidate for solid state lighting applications. Considering white organic light emitting diodes (WOLEDs) have the potential of being ecofriendly, affordable, and efficient with low power consumption and high color quality, WOLEDs may someday replace existing lighting solutions and become the dominant source of solid state lighting.

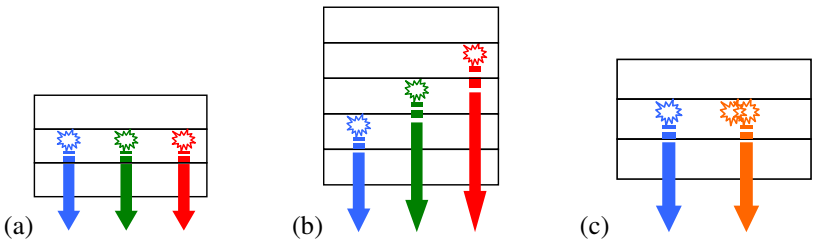


Figure 11 Schemes for three typical WOLEDs architectures: (a) triple-doped emissive layer, (b) multiple emissive layers or multiple-stacked OLEDs; (c) emissive layer with monomer and excimer.

One common approach to achieving WOLEDs with a broad, white-light spectrum is using multiple dopants; to combine single-color sub-elements, either (1) red, green, and blue or (2) blue and orange (Figure 11). This can be achieved either by combining multiple dopants in a single layer or by doping a single dopant in multiple layers. While this approach is capable of achieving high quality white light, it requires a either

additional layers or complicated co-depositions, resulting in a potentially higher manufacturing cost. Also, using multiple emissive materials depends on the precise control over various energy transfer processes within the device which will also significantly complicate the device fabrication. Thus, simpler designs with fewer layers are desired. An alternative to combining several sub-elemental colors to achieve a broad, white-light spectrum is by using a blue or ultraviolet device to excite several phosphors. While down conversion by phosphors design is simple with a potentially more cost effective manufacturing process than WOLEDs containing several sub-elemental colors, it has an inherent limitation in efficiency as the stokes shift in the down-converting process is a source of energy loss. Recently, excimer-based square planar Pt complexes for single doped WOLEDs were developed.[34-36] An exciplex is a metastable complex formed by associative excited state interactions between two different molecules and are known to emit over a wide spectral range. With exciplex as emitting species, some of the square planar Pt complexes were able to emit both blue light itself and the orange light with its exciplex emission. In the chapter 2 of this thesis, a series of novel square planar platinum complexes for single doped white OLEDs will be discussed.

# CHAPTER 2

# AZATETRABENZOPORPHYRINS BASED MATERIALS

## 2.1 Introduction

Since the development of the donor–acceptor heterojunction by Tang[37], many new materials have been synthesized or applied [12,14,38], leading to a steady improvement in the power conversion efficiency to current values of over 11.2% [3]. However, further improvement in the device efficiency, and device lifetime, is still necessary to meet commercial application standards

Metal phthalocyanine (MPc) is a widely studied donor material due to its high hole mobility , strong absorption and high staility. [39,40] However, the OPV devices utilizing MPc was low because of the low Voc reported at around 0.4–0.5 V under normal operating conditions of 1 sun and room temperature.

Porphyrins has been extensively used for dye-sensitized solar cell (DSSC) and high effiecency has been achieved. [41-43] However, the limited absorptivity in the red and near infrared regions of the solar spectrum is the main barrier to incease the power effiecency. On the other side, metal porphyrins were used as red or near infrared emitters in near-infrared OLEDs and have been proven to have high phosphorescent efficiencies.

Azatetrabenzoporphyrins(TBAP) are isoelectronic isomers of phthalocyanine , the structural difference between azatetrabenzoporphyrins and phthalocyanine is one ore more of the carbon atoms at 6, 13, 20,27 position in the phthalocyanine ring being replaced by nitrogrn atoms. So they can be treated as the transition from phthalocyanine to porphyrin, in which all of the four carbon atoms are replaced by nitrogrn atoms. Thus,

azatetrabenzoporphyrins have similar properties with phthalocyanine and porphyrins such as broad and strong absorption, and high hole mobility. But still, the slight structural change change also lead to some differences in photophysical, electrichemical properties. The research of azatetrabenzoporphyrin molecules begun in the 1930s, [44,45]but only one or two of the molecules were proven to be synthesized, and very limited characterization was been done and reported. There was few other reports on azatetrabenzoporphyrin based materials, [46-50] however, the reported reasonable reaction yield of azatetrabenzoporphyrins is not well established. Optimising the synthesizing and characterization of azatetrabenzoporphyrins will fill the blank of many research areas, such as materials chemistry, photophysics etc. and make exploring more properties of the family of phthalocyanine possible. In this chapeter, a modified synthetic method is introduced and all four of the azatetrabenzoporphyrin molecole were synthesized and seperated with high reaction yield. Characterizations such as NMR, electrochemical, photophysics of the obtained azatetrabenzoporphyrin based materials are performed and also compared with phthalocyanine and tetrabenzylporphyrins. Organic solar cell devices are also made using Zinc azatetrabenzoporphyrin materials as donor material and compared with the OPV devices with ZnPc. Free base and Platinum(II) azatetrabenzoporphyrins were also synthesized and Characterized. Near infared OLED were fabricatd using Pt(II) based azatetrabenzoporphyrin materials.

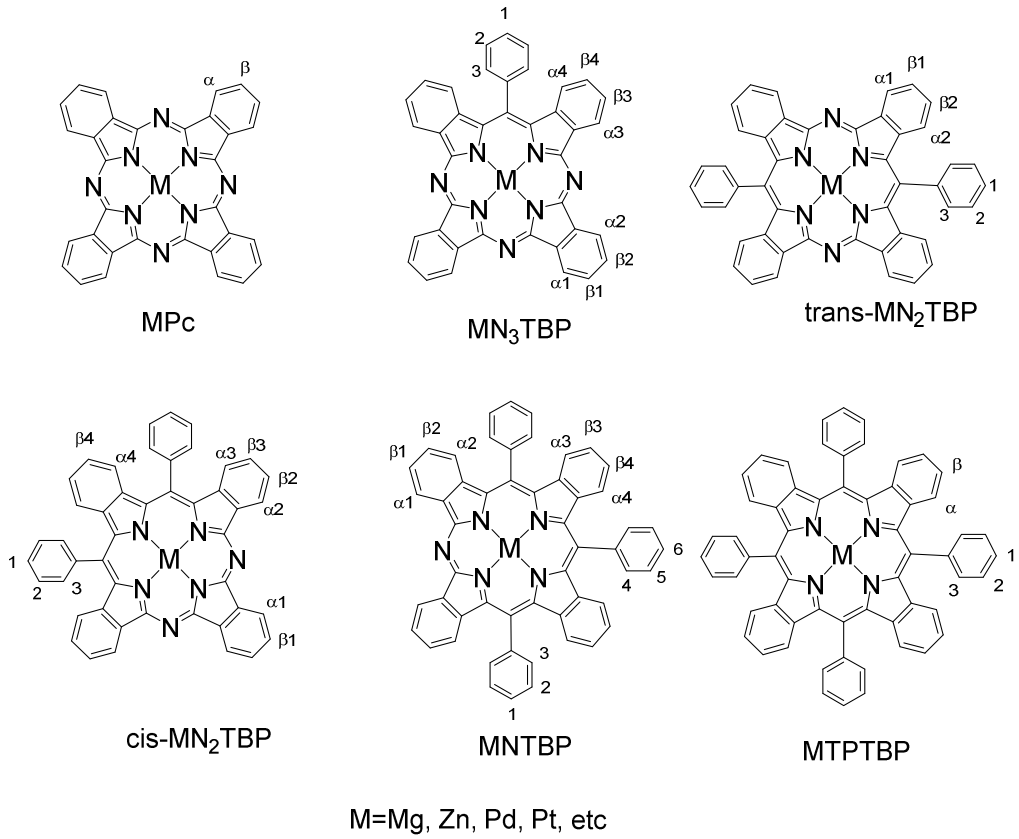


Figure 12 Chemical Structures of MPc, $MN_3TBP$, trans-$MN_2TBP$ , cis-$MN_2TBP$ , MNTBP and MTBP, where α, α1, α2, α3, α4, β, β1, β2, β3, β4 are the hydrogen positions on benzyl group and 1,2,3 are the hydrogen positions on phenyl group.

## 2.2 Synthesis and Structural Characterization

### 2.2.1 General Procedures.

$^1$H NMR spectra were recorded on a 400 MHz Varian Liquid-State spectrometer. NMR samples were dissolved in Hexadeuterodimethyl sulfoxide with 0.03% tetramethylsilane(TMS) as an internal reference. Mass spectra were obtained on an Applied Biosystems Voyager-DE STR matrix-assisted laser desorption/ionization time-of-flight spectrometer (MALDI-TOF). The matrix used for all mass spectra samples was 2,2';5',2''-Terthiophene . The UV-visible spectra were recorded on a Cary 5G UV-vis-NIR spectro-

meter (Varian). Steady state emission experiments at room temperature were performed on a Horiba Jobin Yvon Fluoro- Log-3 spectrometer

Cyclic voltammetry and differential pulsed voltammetry were performed using a CH Instrument 610B electrochemical analyzer. Anhydrous DMF (Aldrich) was used as the solvent under a nitrogen atmosphere, and 0.1 M tetra(n-butyl)-ammonium hexafluorophosphate was used as the supporting electrolyte. A silver wire was used as the pseudo-reference electrode. A Pt wire was used as the counter electrode, and glassy carbon was used as the working electrode. The redox potentials are based on the values measured from differential pulsed voltammetry and are reported relative to a ferrocenium/ferrocene (Fc/Fc) redox couple used as an internal reference (0.45 V vs SCE) The reversibility of reduction or oxidation was determined using cyclic voltammetry. As defined, if peak anodic and peak cathodic currents have an equal magnitude under the conditions of fast scan (100 mV/s or above) and slow scan (50 mV/s), then the process is reversible; if the magnitudes in peak anodic and peak cathodic currents are the same in fast scan but slightly different in slow scan, the process is defined as quasi-reversible; otherwise, the process is defined as irreversible.

2.2.2 Synthesis of Zinc azatetrabenzoporphyrins

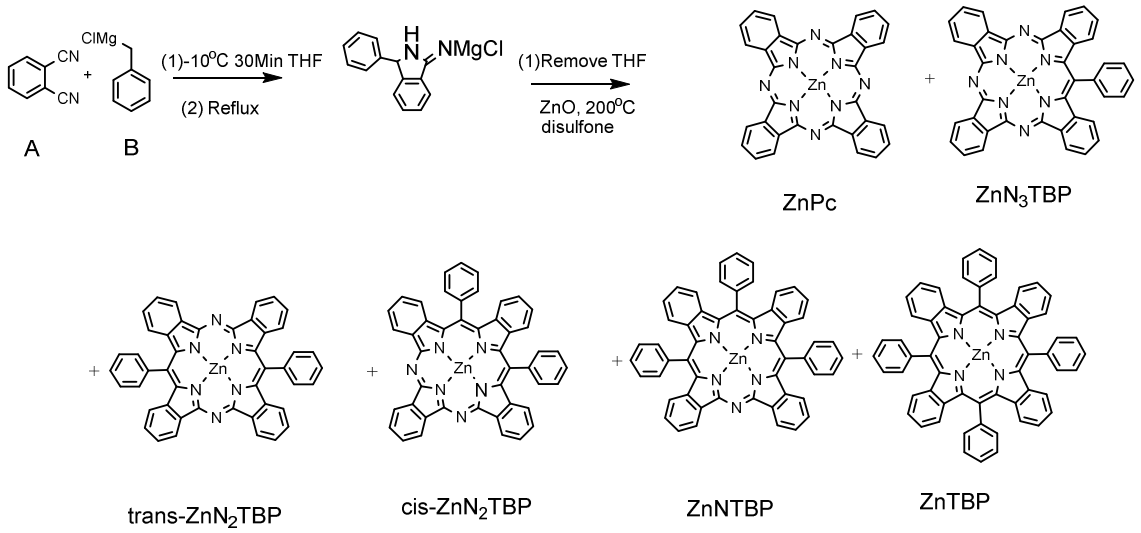


Figure 13 Synthetic routes for ZnPc, $ZnN_3TBP$, trans-$ZnN_2TBP$, cis-$ZnN_2TBP$ , ZnNTBP and ZnTBP , where reaction yield of product depends on thedifferent ratio between starting materials phthalontrile (A) and benzylmagnesium chloride(B).

To a solution of phthalontrile (12.8 g, 100 mmol) in 200 ml THF at -10℃, was added benzylmanesium chloride (25 ml, 50 mmol, 2 M in THF) dropwise in a period of 10 min, the mixture was stirred for 30 min at -10℃ and 1 hour under reflux. The mixture was cooled down to room temperature and THF was removed by flowing nitrogen gas into the solution. ZnO (4 g, 49.4 mmol) and disulfone(50 ml) were added and the mixture was heated to 220℃ for 12 hours. The resulting solution turned from dark brown to dark blue. After cooling to 60℃, the solution was poured to 300 ml of water and filtered. The remaining solid was washed by water for several times to remove disulfone and was dried under vacuum. The solid was washed with 100 ml*3 of THF and the resulting solution was evaporated. The obtained blue solid was firstly purified with silica gel chromatography with DCM to obtain Zinc tetraphenyltetrabenzoporphyrin(ZnTPTBP)

then with DCM/THF 10:1 to obtain the mixture of Zinc 6,20-diaza-13,27-diphenyltetrabenzo-porphyrin(trans-$ZnN_2TBP$) and Zinc 6-aza-13,20,27-triphenyltetrabenzoporphyrin (ZnNTBP) , pure Zinc 6,13-diaza-20,27-diphenyltetrabenzoporphyrin(cis-$ZnN_2TBP$) (685 mg, 0.94 mmol, 3.8% yield) and pure Zinc 6, 13,20-tri-aza-27-triphenyltetrabenzoporphyrin ($ZnN_3TBP$) (3.51 g, 21.04% yield ) and lastly with methanol to afford ZnPC. The trans-$ZnN_2TBP$ and ZnNTBP mixture was further purified using aluminum oxide columnchromatography with DCM/THF 10:1 as eluent to afford pure trans-$ZnN_2TBP$(744 mg, 1.02 mmol, 4.1% yield) and ZnNTBP(747mg, 0.93 mmol, 5.6% yield).

Zinc 6, 13,20-tri-aza-27-triphenyltetrabenzoporphyrin ($ZnN_3TBP$) 1H NMR(400 MHz, DMSO-d6) δ 9.52 (d; 2H), 9.46-9.40 (m; 4H), 8.29-8.23 (m; 4H), 8.18-8.08(m; 3H), 8.04-7.96 (m; 4H), 7.66(t; 4H), 6.95(d, 2H).

Zinc 6,20-diaza-13,27-diphenyltetrabenzoporphyrin(trans-$ZnN_2TBP$.1H NMR (400 MHz, DMSO-d6) δ 9.66 (d; 4H), 8.24-8.18 (m;4H), 8.13 (dd; 2H), 8.07-7.99 (m; 8H), 7.71 (dd; 4H),7.05 (d; 4H).

Zinc 6,13-diaza-20,27-diphenyltetrabenzoporphyrin(cis-$ZnN_2TBP$). 1H NMR (400 MHz, DMSO-d6) δ 9.54 (d; 2H), 9.44 (m;2H; ), 8.26 m; 2H), 8.13-8.05 (m; 6H), 8.01-7.94 (m; 6H), 7.63 (t; 2H), 7.29 (m; 2H),6.97 (m; 2H), 6.78 (d; 2H).

Zinc 6-dza-13,20,27-triphenyltetrabenzoporphyrin (ZnNTBP). 1H NMR (400 MHz, DMSO-d6) δ 9.56 (d; 2H), 8.19-8.10 (m; 6H), 8.10-8.01 (m; 3H), 8.01-7.91 (m; 8H),

7.64 (dd; 2H), 7.30-7.25(m; 4H), 7.10-7.05 (m; 2H), 6.91-6.85(m; 4H).

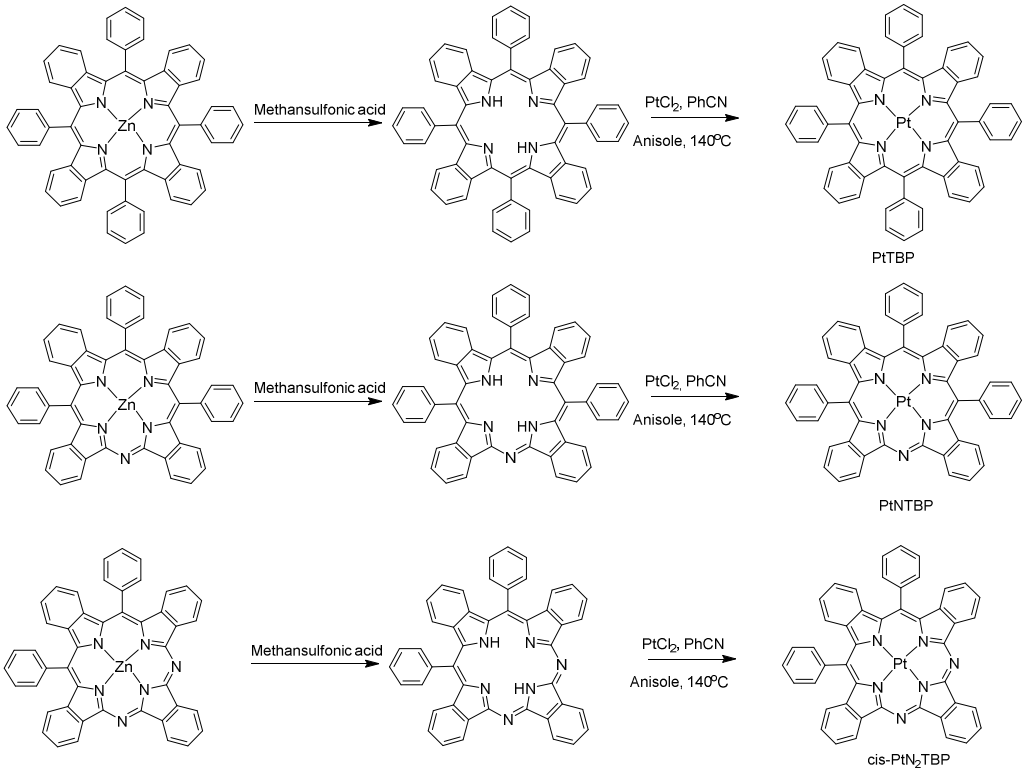


Figure 14 Synthetic routes for PtTBP, PtNTBP and cis-$PtN_2TBP$.

2.2.3 synthesis of free base azatetrabenzoporphyrins

6-Aza-13,20,27-triphenyltetrabenzoporphyrin (H2NTBP). ZnNTBP(100 mg ) was dissolved in 20 mL of methansulfonicacid and the color changed from green to deep red, the mixture was stirred for 30 min at room temperature The solution was poured into 100ml of water, and the the precipitated solid was collected, washed with water for several times, and dired for next step use. Yield: 75 mg, 82%.1H NMR (400 MHz, $CDCl_3$),ppm:9.50(d;2H;),8.25-8.18 (m;6H),8.01-7.79 (m; 11H), 7.61 (t; 2H), 7.30-7.21 (m; 4H), 7.15 (m;2H),7.10 (d; 2H), 6.98(d; 2H).

6,13-Diaza-20,27-diphenyltetrabenzoporphyrin (cis-$H_2N_2$TBP). cis-$ZnN_2$TBP (100 mg ) was dissolved in 20 mL of methansulfonic acid and trifluoromethansulfonic acid (2:1 v/v), the mixture was stirred for 30 min at room temperature The solution was poured into 100 ml of water, and the the precipitated solid was collected, washed with water for several times, and dired for next step use. Yield: 68 mg, 73%.Yield. 1H NMR (400 MHz, $CDCl_3$), ppm: 9.46-9.25 (m; 4H;), 8.23-8.04 (m; 6H;), 7.99 (dd; 2H;), 7.94-7.79 (m; 6H;), 7.53 (m; 2H;), 7.31 (m; 2H;), 7.04 (m; 2H), 6.81 (m; 2H;).

2.2.4 synthesis of Platinum azatetrabenzoporphyrins

. Platinum(II)6-Aza-13,20,27-triphenyltetrabenzoporphyrin (PtNTBP). $H_2$NTBP(150 mg,0.2 mmol) and $Pt(C_6H_5CN)_2Cl_2$ (150 mg,0.3 mmol) were dissolved in 4 mL of diphenylether. The solution was stirred at 160 °C for 12 hours. After the mixture was cooled down to room temperature it was precipitated with hexane (60 ml) and the residue was purified by column chromatography on silica gel with DCM as eluent to afford the desired product as purple solid (130 mg, 68%) $^1$H NMR (400 MHz, $CDCl_3$) :ppm: 9.53 (d; 2H),8.19-8.09(m;6H;), 8.03-7.82 (m; 11H;), 7.56 (dd; 2H;), 7.27 (m; 4H;), 7.11(d;2H;),6.97(d;2H;), 6.93 (d ;2H;).

. Platinum(II) 6,13-Diaza-20,27-diphenyltetrabenzoporphyrin(cis-$PtN_2$TBP). cis-H2N2TBP (140 mg,0.2 mmol) and $Pt(C_6H_5CN)_2Cl_2$ (150 mg,0.3 mmol) were dissolved in 4 mL of diphenylether. The solution was stirred at 160 °C for 12 hours. After the mixture was cooled down to room temperature it was precipitated with hexane (60 ml) and the residue was purified by column chromatography on silica gel with DCM as eluent to afford the desired product as purple solid (80 mg, 44.6%) $^1$H NMR ((400 MHz,

$CDCl_3$): $^1H$ NMR (DMSO-$d_6$, 400 MHz) :ppm: 9.32 (d; 2H;), 9.23(m; 2H;), 8.08-7.96 (m; 6H;), 7.99 (dd; 2H;), 7.89 (dd; 4H;), 7.79 (dd; 2H;), 7.49 (dd; 2H;), 6.92 (m; 2H), 6.64 (d; 2H;).

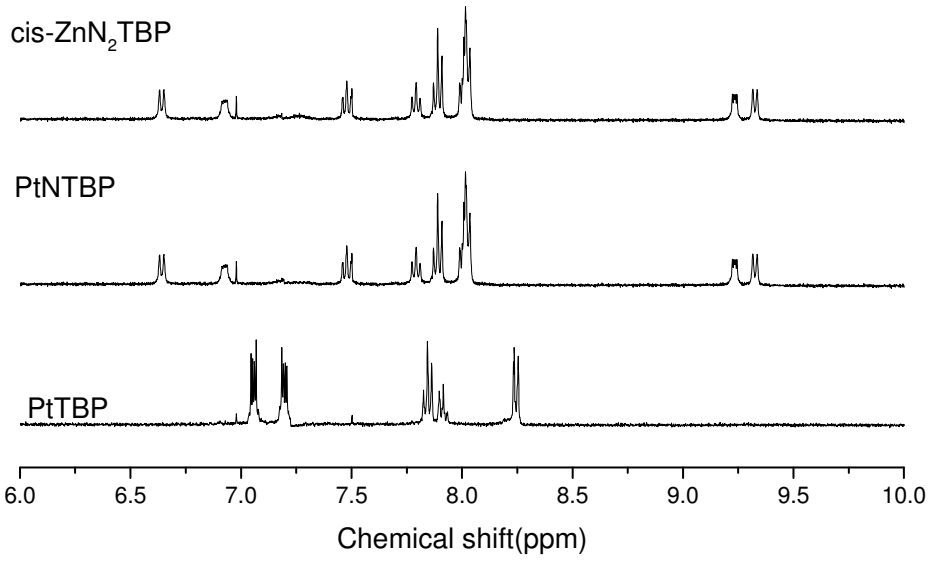


Figure 15 :Proton NMR spectra of cis-$ZnN_2$TBP, PtNTBP and PtTBP in $CDCl_3$

## 2.3 Results and Discussion

### 2.3.1 Synthetic mechanism

Figure 14 shows the synthetic route of the Znic TBAP materials. Phthalontrile was firstly reacted with benzylmagnesium chloride with 4:1 to 1:1 ratio at -10℃ and then refluxed for 1 hour. With the addition of Znic oxide and sulfolane after the removel of THF the mixture was heated to 220°C for 12 hours.

In the previous reports, quinoline was used as the solvent for the second step. [44-46] However, provided the high boiling point of quinoline, it would be difficult to process the

reaction by totally evaporating quinoline through vacuum. In this work, sulfolane was used as the solvent for the second step to replace quinoline, comsidering sulfolane not only has high boiling point to support the reaction at 220 ºC but also is miscible with water. Thereful, sulfolane can be easily removed by washing the resulting solution with water.

It was proposed by Barrett et al. that the addition of Grignard reagent to phthalontrile will form iminoisoindoline derivative as an intermediate product, and the TBAP ring will be formed with iminoisoindoline reacting with the excess phthalontrile. [44,45]Leznoff et al. utilized this method to synthesize a series of tetrabenzotriazaporphyrins and tetranaphthotriazaporphyrin derivatives with moderate yield.[46] However, when we tried to react with benzylmanesium chloride with phthalontrile at room temperature for several hours then add Zinc oxide and react in 220 ºC, only trace of the TBAP product was formed with ZnPc as the main product. Similar result was also detected by Cammidge et al.[51] when they tried to synthesize magnesium based TBAP materials. The possible reason for the low reaction yield is that the iminoisoindoline intermediate was not formed at high yield at room temperature..

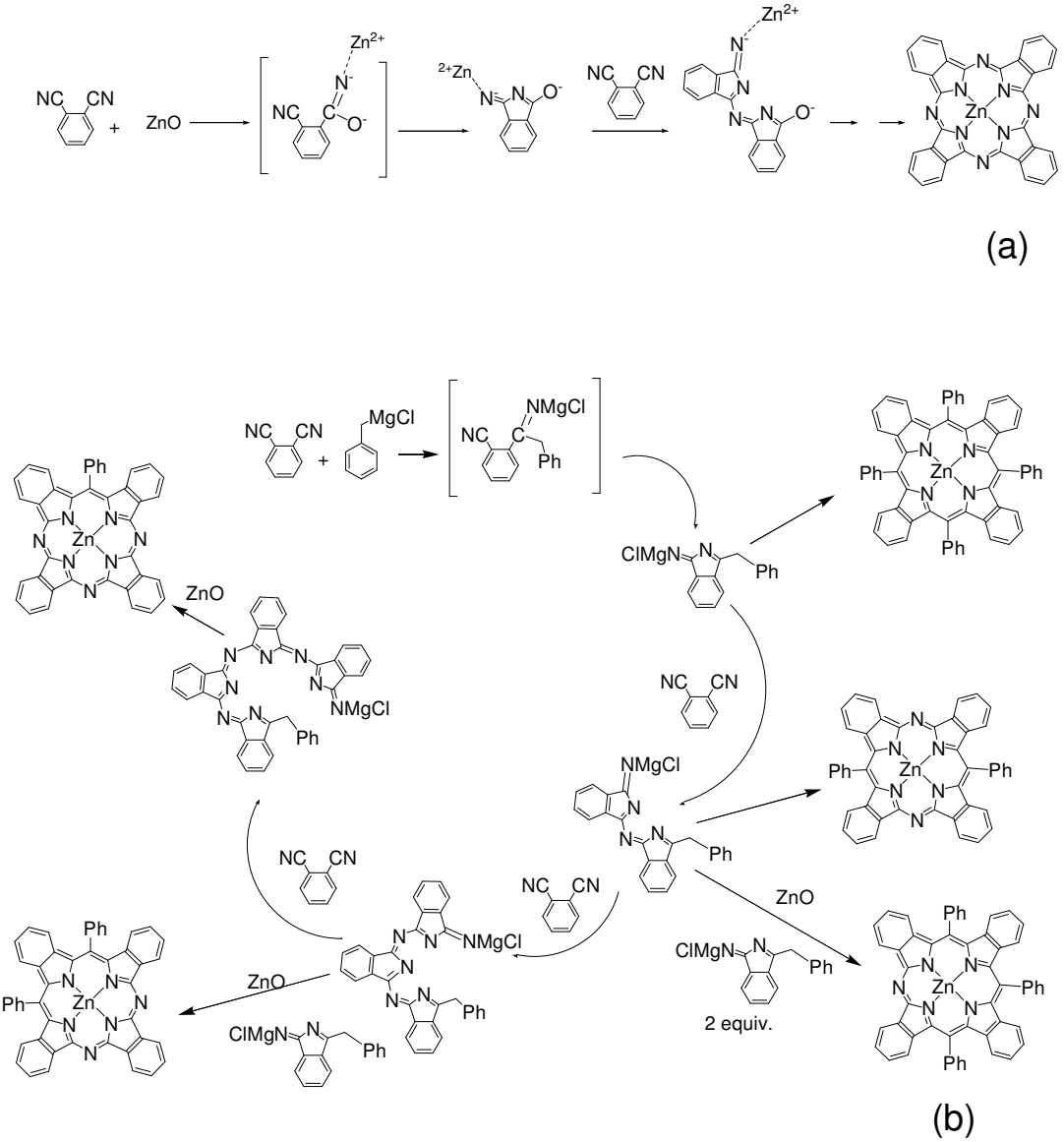


Figure 16 Proposed reaction mechanisms for the synthesis of (a) ZnPc and (b) the group of ZnPc, $ZnN_3TBP$, trans-$ZnN_2TBP$, cis-$ZnN_2TBP$, ZnNTBP and ZnTBP.

The Proposed mechanism for the synthesis is shown in Figure 16(b). By heating the reactant mixture of phthalontrile and benzylmagnesium chloride to refux in THF solution instead of at room temperature for the first step, the reaction yield increased dramatically. More interestingly, by increasing the ratios of the Grignard regent to phthalontrile from 1:4 to 4:4, the content of the trans-$ZnN_2TBP$, cis-$ZnN_2TBP$ and ZnNTBP increased in the product mixture with $ZnN_3TBP$ still as the main product with the reaction similar yield of

other three TBAP derivatives. When the column was flushed with methanol after all the TBAP materials were separated, a large quantity of ZnPc was washed out. This could be explained that after the addition of Zinc Oxide, there are two competitive reactions**Error! Reference source not found.**: iminoisoindoline intermediate reacting with the rest of phthalontrile to form dimmers, trimers and tetramers, and phthalontrile reacting with Znic oxide directly to form ZnPc. Because of the higher reactivity of the reaction between iminoisoindoline derivertives and phthalontrile than the ring closing step, the formation of $ZnN_3TBP$ will be faster than that of the other TBAP derivatives, which lead to higher yield of $ZnN_3TBP$.

Table 1 Summery of reaction yields of ZnTABP materials with different ratios of Girard reagent and phthalonitrile

| Ratios | $ZnN_3TBP$ | *trans*-$ZnN_2TBP$ | *cis-*$ZnN_2TBP$ | ZnNTBP | ZnTBP |
|---|---|---|---|---|---|
| 1:4 | 15% | trace | trace | | |
| 2:4 | 21.0% | 4.1% | 3.7% | 5.5% | 3.6% |
| 3:4 | 18.2% | 4.3% | 4.6% | 7.7% | 4.6% |
| 4:4 | 8.8% | 2.4% | 2.2% | 1.7% | 3.2% |

The TBAP materials in previous reports with Grignard regent route were all magnesium based because Grignard regent also provided magnesium as the metal source. However, the size of magnesium atom is smaller in size to fit the porphyrin rings well. Thus, the demetallization of magnesium based TABP materials can be easily carried out by refluxing in glacial acetic acid. Zinc atom has been proved to have extraordinary template effect in synthesizing porphyrin based materials because of the strong coordination ability with porphyrin rings. [52,53]By adding excess amount of Zinc oxide to the reaction system , only Zinc based TBAP materials were formed without any

magnesium based TBAP materials. All the Zinc TBAP materials are very stable in high temperature and can be sublimed at 380°C to form purple cyrstals.

### 2.2.2 $^1$H NMR spectrum

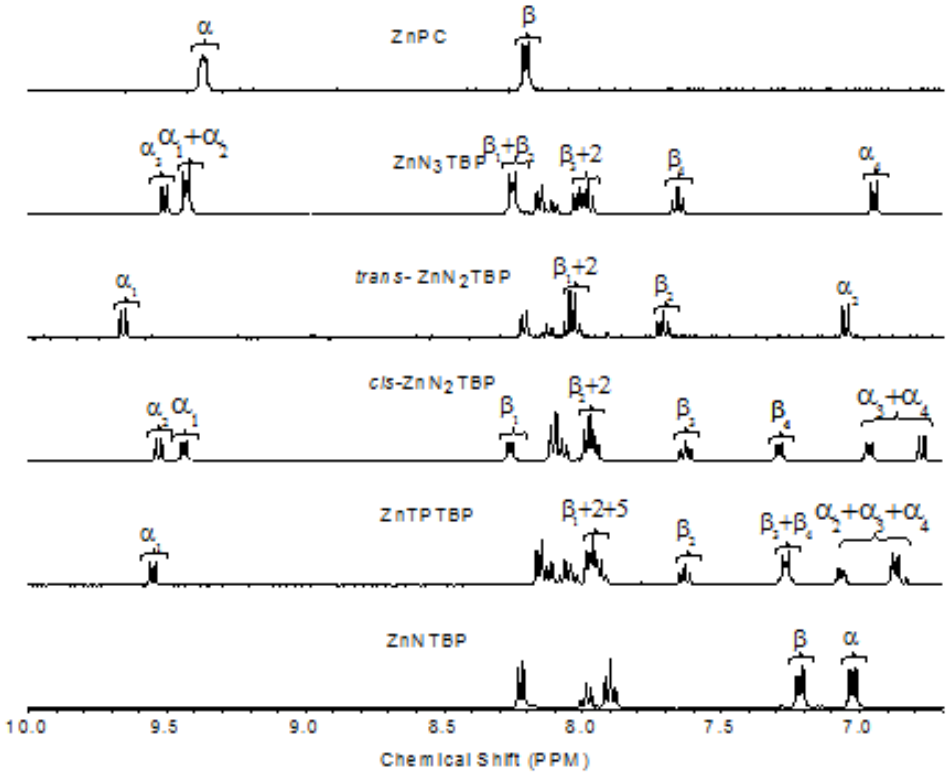


Figure 17 Proton NMR spectra of ZnPc, $ZnN_3TBP$, trans-$ZnN_2TBP$ , cis-$ZnN_2TBP$ , ZnNTBP and ZnTBP in d6-DMSO.

**Error! Reference source not found.**17 shows the $^1$H NMR spectrum of ZnPc, ZnTPTBP and the four ZnTBAP complexes. The employment of aza group break the symmetry of ZnTBAP molecular from D4h (ZnPc and ZnTPTBP) to C2v($ZnN_3TBP$, cis-$ZnN_2TBP$ and ZnNTBP) or D2h(trans-ZnN2TBP). The $^1$H NMR spectrum of the ZnTBAP molecular are much more complicated than that of ZnPc and ZnTPTBP.

However, the four ZnTBAP molecule can be clearly identified because of the difference of chemical shifts.

The chemical shifts of the protons in phthalocyanine and porphyrin complexes are largely effected by the ring current.[54-58] The chemical shift of the protons α and β are in the lower field (9.38ppm and 8.21ppm) for ZnPc is due to the strong ring current of the big ring and greatly deshields the protons. However, because of the shielding effect caused by the meso phenyl group in ZnTPTBP,[59] the chemical shifts of the protons α and β are much higher (7.21ppm and 7.02ppm) than that of ZnPc. The unique hybrid structure of azaporphyrin caused dramatically split of α and β protons. The difference in chemical shifts for protons α of $ZnN_3TBP$, trans-$ZnN_2TBP$, cis-$ZnN_2TBP$ and ZnNTBP are 1028Hz, 1048Hz, 1224Hz and 1076Hz. For the protons on the benzyl groups between aza and methine groups in the TBAPs molecular, the signal of protons α adjacent to the aza group is in lower field than that of phthalocyanine, this may because of the less electron withdrawing ability of the methine group enhanced the ring current deshilding effect. However, the other protons α on the same benzo ring which is close to meso substituted phenyl ring are in higher field, this may because of the shielding effect of the phenyl ring which is perpendicular to the plane of the macrocycle, [60] Because of the higher symmetry of trans-$ZnN_2TBP$ which lead to higher ring current[61], the protons α of trans-$ZnN_2TBP$ is in the lower field compared to those of other TBAP protons.

The protons β1 and β2 on $ZnN_3TBP$ and protons β1 on cis-$ZnN_2TBP$, have a longer distance from the meso substituted phenyl ring, show Pc like signals in the low field with minor difference in shift. Similarly, the protons β3 and β4 on ZnNTBP and protons β4 on

cis-$ZnN_2TBP$ have very similar shift as protons β on TPTBP. For the signals of the rest β protons, their signals located between the shifts of β protons of Pc and TPTBP, which may because of the competition of the shielding effect from the ring current and deshielding effect from the phenyl ring.

2.2.3 Electrochemical Properties

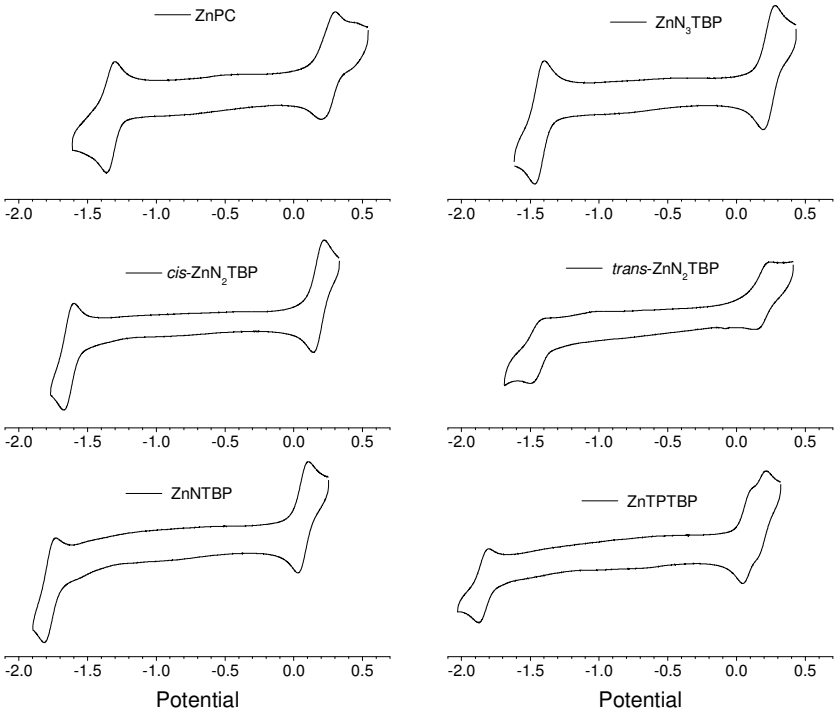


Figure 18 Cyclic voltammetry analysis of ZnPc, $ZnN_3TBP$, trans-$ZnN_2TBP$ , cis-$ZnN_2TBP$ , ZnNTBP and ZnTBP in dimethylformamide with ferrocene used as an internal reference with a scan rate of 100mV/s.

The electrochemical properties of TBAP materials as well as ZnTBP and ZnPc were carried out using cyclic voltammetry, and the values of redox potentials were determined using differential pulsed voltammetry (

). All of the electrochemical data reported here were measured ryelative to an internal ferrocenium/ferrocene reference ($Fc^+/Fc$).

Because the metal centers are not redox active, Oxidation and reduction of these compounds directly involve in the porphyrin rings. Two reversible one electron reduction were detected for ZnPc, $ZnN_3TBP$, and cis-$ZnN_2TBP$. However, for ZnNTBP and ZnTPTBP, which only have one or zero meso aza nitrogen, only have the first reduction reversible. The first reduction potential is increased with derease of the number if aza-

nitrogen group from ZnPc(-1.36eV) to ZnTPTBP((-1.82eV) . This maybe because the aza-nitrogen bridge is more electron withdrawing that the methine group, which makes the molecular with more aza nitrogen groups easier to reduce.

Table 2 Summery of the electrochemical dataof ZnPc, $ZnN_3TBP$, trans-$ZnN_2TBP$ , cis-$ZnN_2TBP$ , ZnNTBP and ZnTBP.

| | $E_{1/2}^{ox}$ (V) | $E_{1/2}^{red}$ (V) | HOMO (eV) | $E_g$(eV) |
|---|---|---|---|---|
| ZnPc | 0.258 | -1.336 | -4.96 | 1.594 |
| $ZnN_3TBP$ | 0.245 | -1.43 | -4.94 | 1.68 |
| *trans*-$ZnN_2TBP$ | 0.2 | -1.44 | -4.88 | 1.64 |
| *cis*-$ZnN_2TBP$ | 0.19 | -1.63 | -4.87 | 1.82 |
| ZnNTBP | 0.14 | -1.71 | - 4.80 | 1.85 |
| ZnTPTBP | 0.16 | -1.87 | -4.82 | 2.03 |

The first oxidation potential increased with the gradual replacement of methine group with aza-nitrogen group, compared to the difference of the reduction potential, the difference of the first oxidation from ZnPc to ZnTPTBP is small, only 0.13eV. The obvious change in the first reduction potential and the small difference in the oxidation potential result in a clear trend of bandgap: From ZnTPTBP to ZnPc, the bandgap decreased from 1.92eV to 1.59eV.

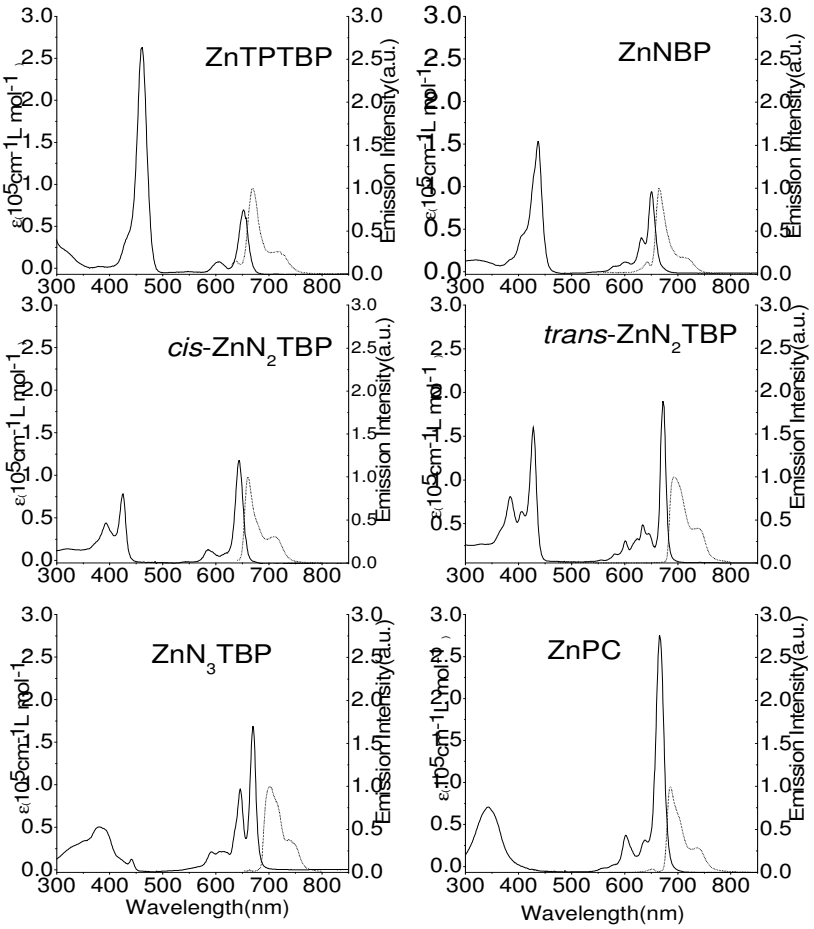


Figure 19 The absorption spectra (solid line) and emission spectra (dotted line) of ZnPc, $ZnN_3TBP$, *trans*-$ZnN_2TBP$ , *cis*-$ZnN_2TBP$ , ZnNTBP and ZnTBP in a solution of DCM at room temperature.

2.2.4 Photophysical Properties

UV-vis absorption spectra and emission spectrum is shown in Figure 19. .The dramastic differences in the peak value and intensity of the UV-vis absorption spectra reveals that the aza substitution has a great impact on the energy levels. The progressively addition of aza nitrogen atoms from ZnTPTBP to ZnPc increased the absorptivity of Q band increased from $0.694\times10^5 m^{-1}cm^{-1}$ (ZnTPTBP)to $2.75\times10^5 m^{-1}cm^{-1}$

(ZnPc) and decreased the intensity of B band from 2.63 $\times 10^5$ $m^{-1}cm^{-1}$ to 0.708$\times 10^5$ $m^{-1}cm^{-1}$

According to Gouterman's four-orbital model, Q band is formed largely because of two transitions: HOMO to LUMO and HOMO to $LUMO^{-1}$ and B band is because of the transitions of $HOMO^{+1}$ to LUMO and $HOMO^{+1}$ to LUMO. The B band is blue shifted from 461 nm (ZnTPTBP) to 342 nm (ZnPc) with the graduate substitute of meso mehine group with aza nitrogen group. This is due to the difference of the electron affinity of meso mehine group and the aza-nitrogen group, and the substitution of methine group with aza-nitrogen groups from ZnTPTBP to ZnPc gradually stabilized the $HOMO^{-1}$.

Table 3 Photophysical properties of ZnPc, $ZnN_3TBP$, trans-$ZnN_2TBP$ , cis-$ZnN_2TBP$ , ZnNTBP and ZnTBP

| | B-band Absorption $\lambda_{max}$ (ε) {nm ($10^5$ $M^{-1}$ $cm^{-1}$)} | Q-band Absorption $\lambda_{max}$ (ε) {nm ($10^5$ $M^{-1}$ $cm^{-1}$)} | $\lambda_{max}$ (nm) | Stokes shift (nm) |
|---|---|---|---|---|
| ZnTPTBP | 461(2.635) | 652(0.694) | 668 | 16 |
| ZnNTBP | 437(1.535) | 632(0.397), 650(0.939) | 664 | 14 |
| *cis*-$ZnN_2TBP$ | 393(0.438), 425(0.784) | 644(1.179) | 667 | 23 |
| *trans*-$ZnN_2TBP$ | 384(0.806), 428(1.599) | 634(0.487), 672(1.901) | 693 | 21 |
| $ZnN_3TBP$ | 381(0.504) | 646(0.947), 670(1.687) | 702 | 32 |
| ZnPC | 342(0.708) | 666(2.75) | 686 | 20 |

Similar to other for low symmetry porphyrins and PCs, both B band and Q band of the TBAP showed clear split because of the decrease in symmetry. The symmetry breaking

will lead to significant difference in ΔLUMO and ΔHOMO values.The split energy of B band from $ZnN_3TBP$ to ZnNTBP is shown in table 3. cis-$ZnN_2TBP$ did not show split in the Q band even though it only has C2v symmetry, this could due to the small the ΔLUMO value of cis-$ZnN_2TBP$. All the Znic TBAP materials are deep red emitters( Figure 19) The Stokes shift for all the materials are very small, only 10 nm to 30 nm. ZnPc, $ZnN_3TBP$ trans-$ZnN_2TBP$ and cis-$ZnN_2TBP$.

2.2.5 Thin Film Absorptions

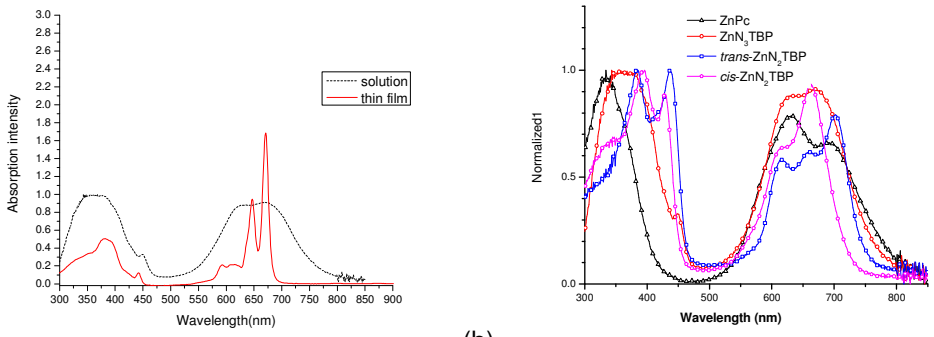


(a) (b)

Figure 20 (a) The absorption spectra of $ZnN_3TBP$ in a solution of tetrahydrofuran (solid) and in neat film (dashed) at room temperature and (b)the absorption spectra of ZnPc(triangles), $ZnN_3TBP$(circles), trans-$ZnN_2TBP$(squares) and cis-$ZnN_2TBP$(pentagon) thin film.

Thin films were vacuum evaporated on glass substrates and the absorption of these thin films was shown in Figure 20(b), The TBAP materials showed extended absorption compared with their solutions, this indicate that they have strong intermolecular interactions even though they have lower symmetry as ZnPc. it is also worth noted that $ZnN_3TBP$ which has very narrow absorption band in solution, exhibit super broad absorption in films(Figure 20(a),). The B band of ZnPc has a tail at bout 450nm in thin films and the peak is at 334 nm, which is at the ultraviolet region. As the ultraviolet light is mostly absorbed by the ozone layer, it cannot contribute much to solar cell. B band of

TBAP materials showed red shift compared to ZnPc. The thin films of $ZnN_3TBP$ trans-$ZnN_2TBP$ and cis-$ZnN_2TBP$ have absorption peaks at 356 nm, 385 nm and 389 nm respectively with a large part of their absorption over 400 nm with tails extended to around 500 nm.

## 2.3 Organic Solar Cell Devices

$ZnN_3TBP$ and trans-$ZnN_2TBP$ and cis-$ZnN_2TBP$ were first evaluated in a bi-layer solar cell device with a general structure of ITO/donor(20 nm)/ C60 (30 nm)/PTCDI(10 nm)/BCP(14 nm)/Al N,N'-Dihexyl-perylene-3,4,9,10-bis(dicarboximide) (PTCDI) was added as an interfacial layer between the $C_{60}$ acceptor layer and the bathocuproine (BCP) exciton blocking layer to improve the electron injection.[62] For comparison, control devices were fabricated simultaneously with zinc phthalocyanine (ZnPc)) as donor materials. Devices with different donor thickness(5 nm, 10 nm, 15 nm and 20 nm) were fabricated and the results are summarized in Table 4. The current density versus voltage (J-V) characteristics measured under both dark and 1 sun AM1.5G simulated illumination are shown in Figure 21.

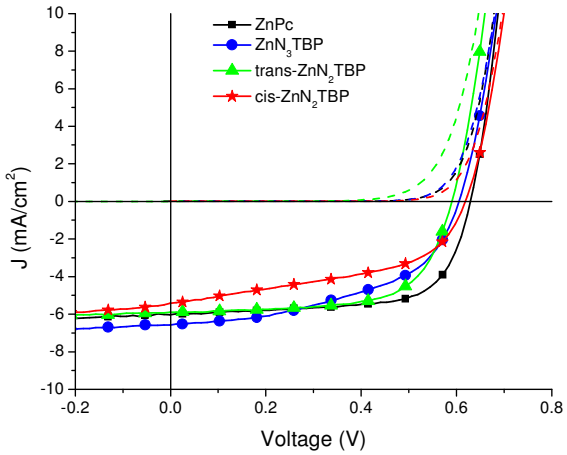


Figure 21 Current-voltage characteristics of ZnPc (squares), $ZnN_3TBP$ (circles) and trans-$ZnN_2TBP$ (triangles) and cis-$ZnN_2TBP$(stars) based bilayer solar cells under dark (open) and 1sun AM 1.5G simulated illumination (solid) in a general device structure of ITO/donor(20 nm)/ C60 (30 nm)/PTCDI(10 nm)/BCP(14 nm)/Al.

The reasonable photocurrent and diode behavior demonstrate that select azatetrabenzoporphyrins can function as donor-type materials in a bilayer device with $C_{60}$ as an acceptor-type material. , the $ZnN_3TBP$ device has a $J_{SC}$ of 6.56 mA/cm$^2$, a FF of 0.50 and a $V_{OC}$ of 0.60 V, leading to a high $\eta_p$ of nearly 2.4%; the trans-$ZnN_2TBP$ device has a $J_{SC}$ of 5.9 mA/cm$^2$, a FF of 0.65 and a $V_{OC}$ of 0.59 V, leading to a high $\eta_p$ of nearly 2.3%; the cis-$ZnN_2TBP$ device has a $J_{SC}$ of 5.4 mA/cm$^2$, a FF of 0.49 and a $V_{OC}$ of 0.61 V, leading to a high $\eta_p$ of nearly 1.65%. . In comparison, ZnPc based devices had $J_{SC}$ of 6.02 mA/cm$^2$, FF of 0.67, $V_{OC}$ of 0.62 V and $\eta_P$ of 5.57 % which are comparable to the literature reports on the same materials.[63,64]

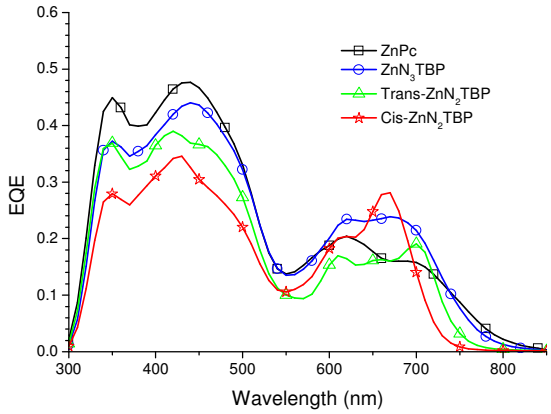


Figure 22 Plots of External quantum efficiency(EQE) vs the wavelength (λ) for ZnPc (squares), $ZnN_3TBP$ (circles) and trans-$ZnN_2TBP$ (triangles) and cis-$ZnN_2TBP$(stars) based based bilayer solar cells with a general structure of ITO/donor(20 nm)/C60(30 nm)/PTCDI(10 nm)/BCP(14 nm)/Al. The data is reported under AM1.5G 1 sun conditions.

To further explore the differences in short circuit current, the device EQE, as a function of wavelength was determined from the photocurrent output generated in the device from an incident monochromatic light source using an Optronic Lab OL750 series spectroradiometer. The EQE was determined by comparing this photocurrent to the monochromatic beam intensity measured using a calibrated Si photodetector. The EQE spectra of these devices are shown in Figure 22. The integration of the EQE spectra with the standard AM1.5G solar spectrum was also used to determine short circuit current to account for the spectral mismatch from the solar simulator. The EQE of the B band region(300 nm to 550 nm) decreased from ZnPc $ZnN_3TBP$ and trans-$ZnN_2TBP$) to cis-$ZnN_2TBP$, which is matching the trend of the adorability of them, however, the EQE of the Q band region (550 nm to 800 nm) did not all follow this trend.

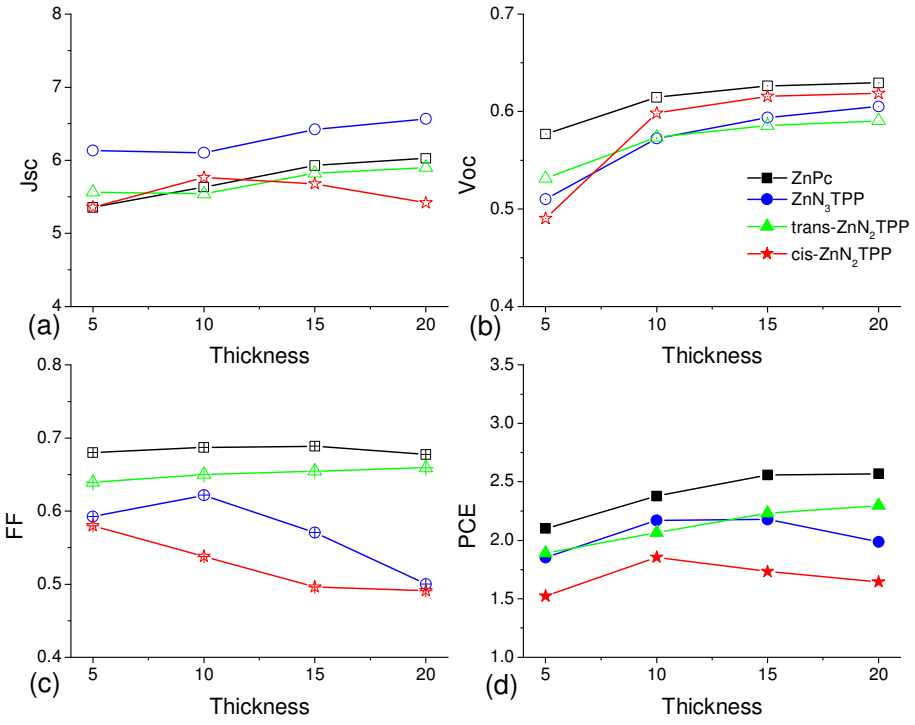


Figure 23 Plots of (a) $J_{sc}$ vs donor thickness (b) $V_{oc}$ vs donor thickness (c) Fill factor vs donor thickness and (d) PCE vs donor thickness for ZnPc (squares), $ZnN_3TBP$ (circles), trans-$ZnN_2TBP$ (triangles) and cis-$ZnN_2TBP$(stars) based bilayer solar cells with a general device structure of ITO/donor(x nm)/C60(30 nm)/PTCDI(10 nm)/BCP(14 nm)/Al, where x ranges from 5 to 20 nm. The data are reported under 1sun AM 1.5G conditions.

The device performance parameters given in Figure 23 shows big changes in $V_{OC}$ for all four donor materials from 5 nm to 10 nm but small changes from 10nm to 20nm. Also, the devices for all four donor materials showed minimal changes in $J_{SC}$,. Additionally, the $ZnN_3TBP$ and cis-$ZnN_2TBP$ device demonstrated a more pronounced drop in FF compared to those of ZnPc and trans-$ZnN_2TBP$ devices. These trends are likely due to the minimal stacking of the the $ZnN_3TBP$ and cis-$ZnN_2TBP$ molecules resulting in reduced intermolecular orbital overlap leading to a slower charge hopping process and a lower mobility.

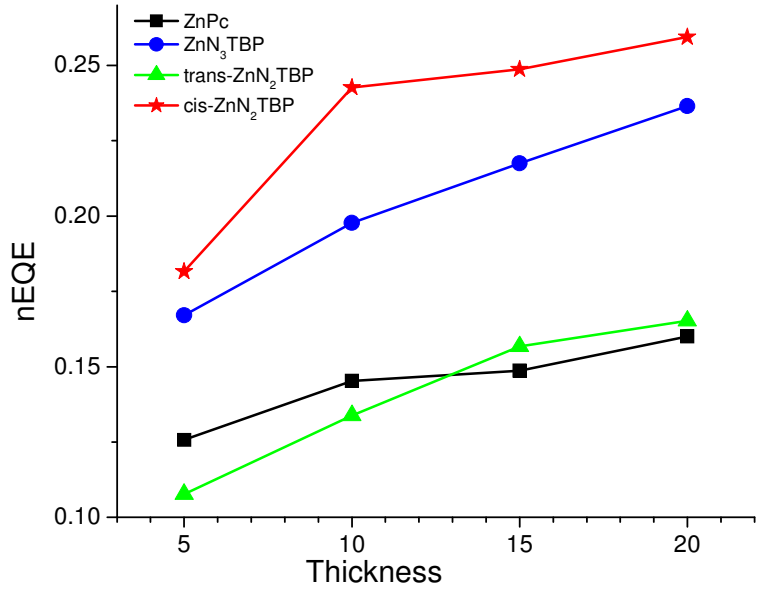


Figure 24 Peak external quantum efficiency as a function of layer thickness for ZnPc (squares), $ZnN_3TBP$ (circles) and trans-$ZnN_2TBP$ (triangles) and cis-$ZnN_2TBP$(stars) based bilayer solar cells with a general structure of ITO/donor(x nm)/C60(30 nm)/PTCDI(10 nm)/BCP(14 nm)/Al, where x ranges from 5 to 20 nm. The data is reported under 1sun AM 1.5G conditions.

By calculating the changes of fraction of External quantum efficiency (nEQE) value at light wavelength of 650 nm with various thicknesses, the exciton diffusion length can estimated. As only the exctons which arrived to the interface of donor and acceptor active layers can contribute to the EQE, so nEQE will increase as the thickness increased within $L_D$, however, when the thickness become larger than the $L_D$, the increase of nEQE will gradually slow down and finally nEQE will begin to decrease. So, $L_D$ can be found at the point that the increase of nEQE begin to drop. Figure 24 shows the value of nEQE changes with the thickness of different donors at a certain wavelength. It is clear to find that the EQE of ZnPc is in the range of 10 nm to 15 nm and the $ZnN_3TBP$ has the longest $L_D$ with about 20 nm. cis-$ZnN_2TBP$ has the lowest EQE which is lower than 10nm. This also verified by the J-V data.

Table 4 Performance parameters of devices for ZnPc, $ZnN_3TBP$, trans-$ZnN_2TBP$ and cis-$ZnN_2TBP$ in the device structure of ITO/donor(x nm)/C60(30 nm)/PTCDI(10 nm)/BCP(14 nm)/Al, where x ranges from 5 to 20 nm. The data are reported under 1sun AM 1.5G conditions.

| Donor material | Thickness | $J_{sc}$ | $V_{oc}$ | FF | PCE | nEQE |
|---|---|---|---|---|---|---|
| ZnPc | 20 | 5.95 | 0.47 | 0.54 | 1.50 | 0.16 |
| | 15 | 5.78 | 0.43 | 0.55 | 1.38 | 0.15 |
| | 10 | 5.92 | 0.42 | 0.56 | 1.38 | 0.15 |
| | 5 | 5.44 | 0.41 | 0.63 | 1.41 | 0.13 |
| $ZnN_3TBP$ | 20 | 6.57 | 0.60 | 0.50 | 1.99 | 0.24 |
| | 15 | 6.42 | 0.59 | 0.57 | 2.18 | 0.22 |
| | 10 | 6.10 | 0.57 | 0.62 | 2.17 | 0.20 |
| | 5 | 6.13 | 0.51 | 0.59 | 1.85 | 0.17 |
| *trans*-$ZnN_2TBP$ | 20 | 5.90 | 0.59 | 0.66 | 2.30 | 0.17 |
| | 15 | 5.82 | 0.59 | 0.65 | 2.23 | 0.16 |
| | 10 | 5.54 | 0.57 | 0.65 | 2.07 | 0.13 |
| | 5 | 5.56 | 0.53 | 0.64 | 1.89 | 0.11 |
| *cis*-$ZnN_2TBP$ | 20 | 5.42 | 0.62 | 0.49 | 1.65 | 0.26 |
| | 15 | 5.68 | 0.62 | 0.50 | 1.73 | 0.25 |
| | 10 | 5.76 | 0.60 | 0.54 | 1.86 | 0.24 |
| | 5 | 5.36 | 0.49 | 0.58 | 1.52 | 0.18 |

## 2.4 Platinum (II) azatetrabenzoporphyrins for Near-Infrared Organic Light Emitting Diodes

One potential application of Organic light emitting diodes is the development of near-infrared OLEDs for a variety of possible applications such as telecommunications, laser, and sensors.[65-67] Approaches to achieve such emission have focused on rare-earth complexes, low band gap polymers, organic fluorescent dyes, or heavy transition metal complexes. Lanthanide complexes[65,68] have demonstrated a wide range of tunable emission to wavelengths up to over 1500 nm, but they typically suffer from low efficiencies resulting from poor energy transfer between the f-orbitals and the organic chelating ligands. Low band gap polymers and organic dyes have also shown very low external quantum efficiencies of much less than 0.1%.[69,70] Amongst the most promising classes of materials is that of phosphorescent transition metal complexes of platinum,[71-75] iridium,[76,77] and osmium.[78,79] Lee et al.[77] demonstrated the room-temperature near-infrared phosphorescence emission of iridium complexes and Jabbour et al.14 reported the moderately efficient emission from Ir complexes in device setting using a highly conjugated cyclometalated ligand achieving an emission with a peak at 720 nm and an EQE of 0.1%.

Motivated by the high efficiencies of the narrow red-emitting phosphorescent complex, PtOEP, there has been an enormous interest in platinum porphyrin complexes due to their high chemical and thermal stability, narrow emission bandwidth and relatively high EQE in NIR OLEDs.[74] Thompson and co-workers reported the NIR device based on platinum (II) tetraphenyltetrabenzoporphyrin (PtTPTBP) and achieved an EQE of 8.5% with the emission at 772 nm. However, the achievement of efficient NIR emission in the range of

~1000 nm which is required for communication purposes has been elusive. The dominant strategy for color tuning deeper into the infrared region has focused on the method of expanding π-conjugation of the porphyrin ring.[73] Sommer and coworkers achieved an electroluminescent (EL) emission peak at 900 nm and the maximum EQE of 3.8% using platinum (II) tetraphenyltetranapthoporphyrin (PtTPTNP).[80] However, further increasing the conjugation of the benzyl ring will lead to a molecular weight too high for stable sublimation, which makes this route nearly impossible to reach over 1000 nm emission. Alternatively, phthalocyanines(Pc) based metal complexes, which replace all the meso carbon atoms in the porphyrin ring with nitrogen atoms, are another route to achieve the emission in the IR region. NIR OLEDs based on PdPc and PtPc have been previously reported with the EL emission at 1025 nm and 966 nm, respectively.[81] Nevertheless, the low efficiencies of less than 0.3 % prohibit the success of these materials. Recently, Borisov et al.[66] synthesized Pt (II) azatetrabenzoporphyrins by replacing a number of meso carbon atoms ($C_1$-$C_3$) with nitrogen atoms on the tetrazebzonporphyrin ring. Also, they demonstrated the potential applications of Pt (II) complexes as oxygen-sensing materials by examining the photophysics of Pt (II) azatetrabenzoporphyrins.[66] In order to examine the potential application of Pt (II) aza-triphenyltetrabenzoporphyrin (PtNTBP) and Pt (II) cis-diaza-diphenyltetrabenzoporphyrin (cis-Pt$N_2$TBP) as near-infrared emitting materials, NIR OLEDs with the maximum EQE of 2.8 % and the peak electroluminescence (EL) at 848 nm in a multilayer thermal vacuum evaporated OLED was demonstrated. Also, a single layer solution-processed polymer light emitting diode (PLED) shows the maximum EQE of 0.33 % with the peak EL at 844 nm.

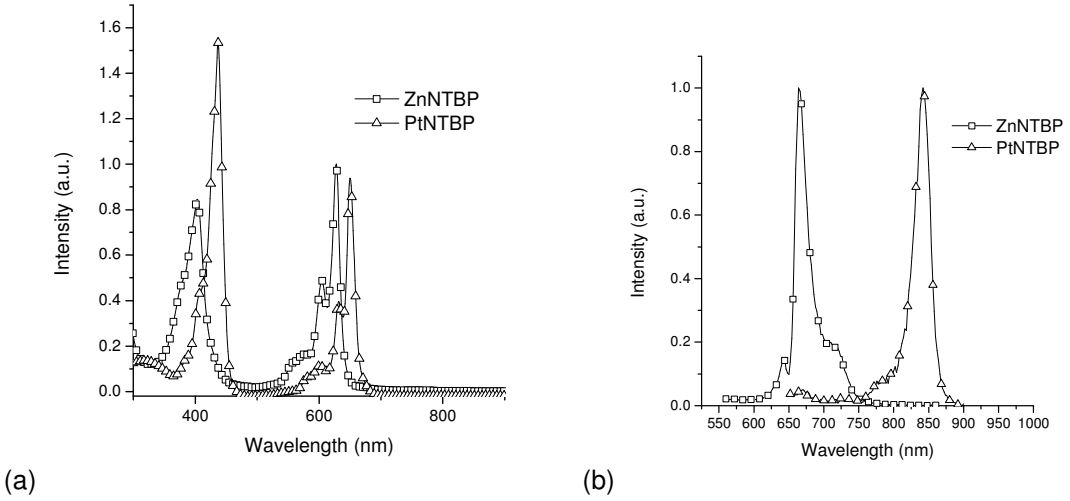


Figure 25 (a)Emission and (b) absorption spectra of ZnNTBP (square), PtNTBP( triangles) ) in a dilute solution of tetrahydrofuran at room temperature.

The absorption and PL spectra of ZnNTBP and PtNTBP are shown in Figure 26 (a) and Figure 26 (b), the absorption peak of both Q band and B band of PtNTBP is slightly blue shifted compared with ZnNTBP. However, the photoluminescent emission peak of PtNTBP is dramatically shifted to the near infrared region up to 842 nm while ZnNTBP has a PL emission at 664 nm, which is still in the deeo red light region. This correspond well with the PL spectra of ZnTBP and PtTBP,.

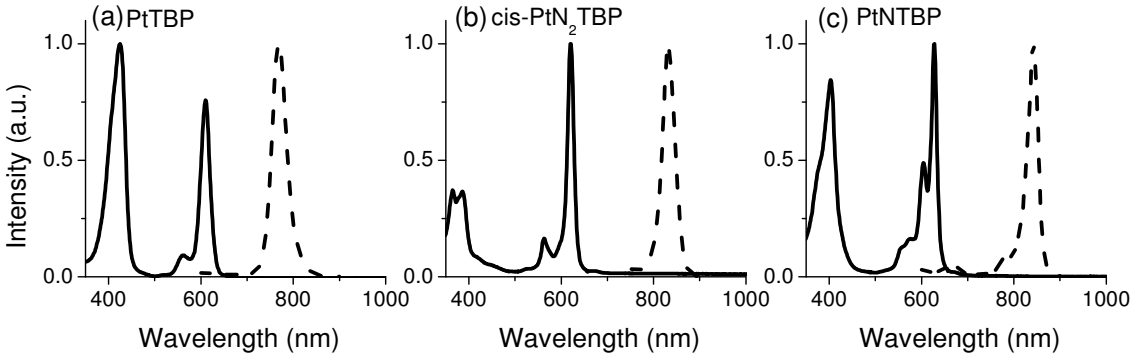


Figure 26 Absorption (solid) and emission spectra (dashed) of (a) PtTBP, (b) PtNTBP and (c) cis-$PtN_2TBP$ in a dilute solution of tetrahydrofuran at room temperature.

The absorption and PL spectra of PtNTBP and cis-$PtN_2TBP$ are compared with those of PtTPTBP in Figure 26 (a) and (b), respectively. The replacement of meso carbon atoms with nitrogen atoms leads to the hypsochromic shift of Soret band accompanied by the decrease in the peak intensity of the absorption spectra. The Soret band around 400nm that is associated with the $S_o \rightarrow S_2$ transition shows a hypsochromic shift from 425 nm to 403 nm for the monoaza-substituted PtNTBP, and from 425 nm to 387 nm for the diaza-substituted cis-$PtN_2TBP$. Also, the substitution of nitrogen atoms leads to the stabilization of LUMO energy, therefore, the Q-bands due to $S_o \rightarrow S_1$ transition will exhibit bathochromic shift. The Q-band of PtNTBP shows a bathochromic shift from 610 nm to 628 nm, in the meanwhile, cis-$PtN_2TBP$ exhibits a small bathochromic shift of the Q-band from 610 nm to 620 nm. This less bathochromic shift about 8 nm for cis-$PtN_2TBP$ can be attributed to the decrease in π-conjugation of meso-phenyl substituents and is in agreement with the previous literature.[66] Moreover, the introduction of the nitrogen atom(s) in the porphyrin ring leads to shifting to lower energy photoluminescent emission due to the stabilization of the LUMO energy level of the porphyrin ring. The monoaza-substituted PtNTBP complex exhibits a 72 nm bathochromic shift in the PL spectrum from 770 nm to 842 nm. The substitution of the second nitrogen atom to form cis-$PtN_2TBP$, however, results in the 60 nm bathochromic shift of PL spectrum from 770 nm to 830 nm. This may be due to the localization of triplet state in only the half of the azaporphyrin ring containing a single nitrogen atom and a meso-carbon atom. In which case, the addition of the second nitrogen atom of cis-$PtN_2TBP$ will only indirectly affect this localized triplet state much, but more study is needed to fully uncover the factors leading to these emission characteristics.

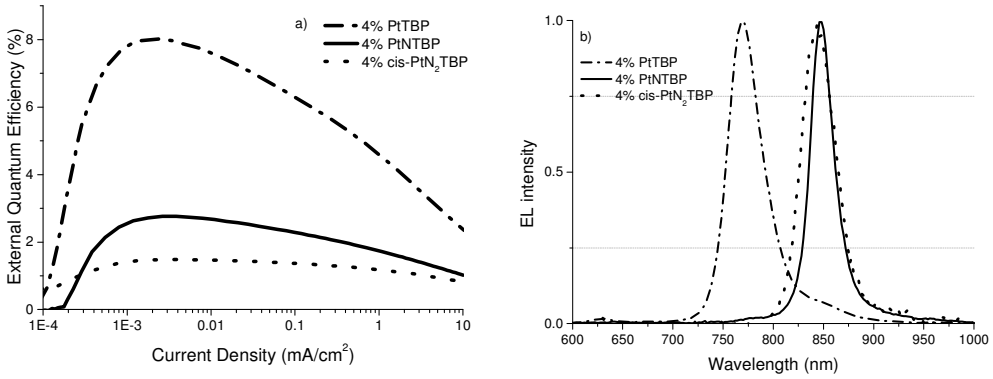


Figure 27 a) External quantum efficiency vs. current density and b) electroluminescent spectra for devices of PtTBP (dash-dot), PtNTBP (solid) and cis- PtN2TBP (dot) in the structure of ITO/PEDOT:PSS/NPD (30 nm)/TAPC (10 nm)/ $Alq_3$: 4% dopant (25 nm)/BCP (40 nm)/Al.

Figure 27 (a) shows the plot of EQE vs. current density (inset: the plot of electroluminescence intensity vs. voltage) of NIR-OLEDs fabricated by thermal vacuum evaporation process. As shown in the EQE vs. current density plot, the device using PtTPTBP demonstrates the maximum EQE of 8.0% and the maximum EL intensity of 4.98 $\mu W/cm^2$ at 8.0 V which is similar to the previous literature report.[58] The device employing PtNTBP, however, shows a decrease in the maximum EQE to 2.8% and the maximum EL intensity of 0.60 $\mu W/cm^2$ at 8.0 V. Also, the device employing cis-$PtN_2TBP$ shows an even greater loss demonstrating only the maximum EQE of 1.5 % and the maximum EL intensity of 0.48 $\mu W/cm^2$ at 8.0 V. This decrease in EQE is in accordance with the previously reported trends of decreasing photoluminescent quantum yields ($\Phi$) and decay time ($\tau$) with the substitution of meso-phenyl rings by nitrogen atoms in Pt (II) tetrabenzooporphyrin complexes.[66] The photoluminescence quantum yields and decay times of PtTPTBP were known to be 0.51 and 47 $\mu s$ at $\lambda_{max}$ = 770 nm. However, the substitution of meso-phenyl rings by nitrogen atoms results in the decrease of the photoluminescence quantum yields and decay times of PtNTBP ($\Phi$ = 0.22 and $\tau$ =

0.40 μs at $\lambda_{max}$ = 844 nm) and cis-$PtN_2TBP$ ($\Phi$ = 0.17 and $\tau$ = 0.20 μs at $\lambda_{max}$ = 841 nm). Despite the decrease in EQE values compared to the device with PtTPTBP, the devices employing PtNTBP and cis- $PtN_2TBP$ demonstrate significant promise in their EL spectra. As shown in Figure 27 (b), the device with monoaza-substituted PtNTBP complex exhibits a dramatic bathochromic shift of nearly 80 nm in the EL spectrum from 770 nm to 848 nm. Also, the device with cis-$PtN_2TBP$ shows the EL spectrum shift from 770 nm to 846 nm. Furthermore, the FWHM of PtNTBP was significantly narrowed to 27 nm compared to 40 nm for PtTPTBP. The combination of the spectral narrowing and the 80 nm bathochromic shift to lower energy EL emission demonstrates the substantially improved optical characteristics of PtNTBP for NIR applications. It is also encouraging that the PtNTBP device shows much better device performance than the previously reported tetrazatetrabenzoporphyrin based material, PtPc,[81] while still exhibiting a large bathochromic shift in the EL spectrum, striking a balance between the two parameters.

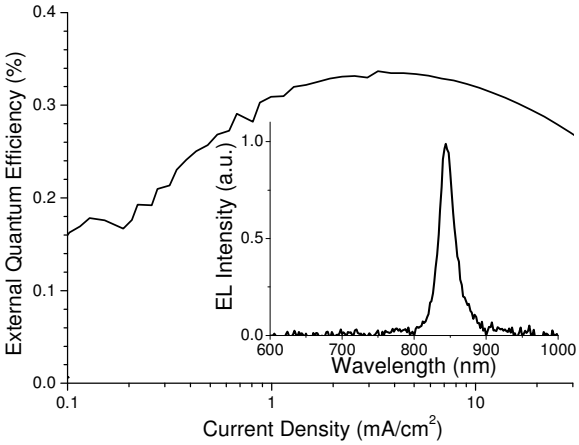


Figure 28 External quantum efficiency vs. current density and the EL spectrum (inset) for the PLED device of PtNTBP.

In order to evaluate the potential application of the solution-processed azatetrabenzoporphyrin (NTBP) devices, solution-processed single-layer PLEDs are prepared and compared with the multi-layer vacuum deposited devices. Because PtNTBP demonstrates a relatively higher EQE in a multi-layer device setting and emits beyond 800 nm in the EL spectrum, PtNTBP is selected. Solution-processed single-layer PLEDs are of interest because of the potential to develop light emitting devices that can be fabricated in high throughput processes with a very simple structure eliminating the need for successive materials depositions which are on order of 5-8 layers in typical OLED devices. One of the most important parameters for the development of solution-processed devices is the solubility of the emissive material in order to achieve the desired dopant concentration. PLEDs with PtNTBP are fabricated by dissolving the emitter in chlorobenzene (CB). However, during the casting procedure of the PtNTBP solution on a substrate using a glass fiber filter (0.45 μm pore size), a significant proportion of the undissolved PtNTBP is filtered. As a consequence, the devices fabricated by the solution of PtNTBP in CB demonstrates the minimal intensity of an EL spectrum. However, when PtNTBP is dissolved in tetrahydrofuran (THF), then mixed with the PVK-PBD solution in CB, the device performance improves dramatically. As shown in Figure 28, the PLED fabricated by the solution of PtNTBP and the PVK-PBD demonstrates the maximum EQE of 0.33% and a peak EL at 844 nm. The poor device efficiencies of PLEDs can be attributed to the relatively high resistivity of polymer host PVK-PBD, inefficient charge confinement within the emissive layer due to the absence of charge blocking layers, and imprecise control of charge transport. Thus, for the further improvements on the device performance, it will require to incorporate the state-of-the-art polymer host materials or

adjust the ratio between the host and the electron transporting materials. Nevertheless, the results of this work demonstrate the possibility to fabricate solution-processed NIR devices with azatetrabenzoporphyrins material

## Conclusion

By modifying the synthetic route, the reaction yield of metal azatetrabenzoporphyrins is dramaticaly increased. Zinc and Platinum azatetrabenzoporphyrins was achieved in large amount. A synthetic mechanism was firstly introduced. NMR, Cyclic voltammetry, absorption, emission was Characterized and compared with ZnPc and Zn porphyrin. Furthermore, $ZnN_3TBP$ and trans-$ZnN_2TBP$ and cis-$ZnN_2TBP$ were first evaluated in a series of bilayer solar cell devices and were compared with ZnPC based devices with the device structures of ITO/donor(5nm~20 nm)/ C60 (30 nm)/PTCDI(10 nm)/BCP(14 nm)/Al. The result of the OPV device with azatetrabenzoporphyrins as donor materials is comparable with ZnPc based OPV devices. Highest $\eta_p$ of 2.18% was achieved with 15 nm $ZnN_3TBP$ as donor materials in OPV devices, 2.3% for 20 nm trans-$ZnN_2TBP$ based OPV devices, and 1.86% for 10 nm cis-$ZnN_2TBP$ based OPV devices. While with same device structure, ZnPc got highest $\eta_p$ of 1.5%.

The fabrication of near infrared OLEDs with efficient EL emission near 850nm is demonstrated by using, PtNTBP and cis-$PtN_2TBP$, exhibit EL emission peaks at 848nm and 846nm with the maximum external quantum efficiencies of 2.8% and 1.5%, respectively. These results also demonstrate an alternative route for a color tuning strategy by replacing the meso-carbon groups with nitrogen groups in a porphyrin ring to shift the EL emission peak nearly 80nm to the infrared region. Furthermore, the

combination of the spectral narrowing and the bathochromic shift to lower energy EL emission demonstrates the potential application of PtNTBP emitter for NIR applications. Also, a solution-processed single-layer PLED utilizing PtNTBP emitter exhibits the maximum EQE of 0.33% and a peak EL at 844 nm, demonstrating a possibility for solution-processed NIR devices based on azatetrabenzoporphyrins.

# CHAPTER 3

# TETRADENTATE PLATINUM AND PALLADIUM COMPLEXES FOR WHITE OLEDS

## 3.1 Introduction

The potential for high power efficiency and potentially low fabrication cost makes WOLEDs highly desirable candidates to replace inefficient incandescent or fluorescent bulbs and compete with expensive inorganic lighting technologies.[82] Most of the best reported WOLEDs have employed multiple emissive materials either as a single layer with multiple emissive dopants, in multiple emissive layers, or through the combination of fluorescent and phosphorescent materials.[83-93] With these structures, typically employing iridium complexes, WOLEDs have achieved external quantum efficiencies over 20%, color rendering index (CRI) over 80, and power efficiencies over 100lm/W when advanced outcoupling techniques are employing.[94] However, the strategy of using multiple emissive materials depends on the precise control over various energy transfer processes within the device which can significantly complicate the device fabrication and have significant tradeoffs between device efficiency and emission color.[95] Furthermore, the precise color balance of WOLEDs containing multiple emissive materials can be significantly perturbed by variations in the driving conditions, or through different aging processing of the various materials.[96] Thus, it is strongly desired to achieve an efficient WOLED containing a single emissive material which is efficient, stable, and can be fabricated within a single emissive layer.

One major approach to achieve single doped white OLEDs is through the exploitation of the excimer emission properties of square planar complexes for a broad white

emission.[34,97,98] In excimer based OLEDs, white emission is achieved through the combination of blue emission from an isolated dopant molecule and orange-red emission of two or more closely stacked dopant molecules. Much of the existing reports of excimer based white OLEDs employ either bidentate or tridentate cyclometalating ligands, both of which have typically demonstrated EQE less than 20% and often poor CRI or CIE coordinates.[99-101] One exception is the recent development of platinum(II) bis(methyl-imidazolyl)benzene chloride (Pt-16) resulted in a device with peak EQE of 20.1%, CRI of 80, and CIE of (0.33,0.33).[36, 101,102] However, it was demonstrated that the monomer species of Pt-16 was inefficient, leading to a lower overall efficiency and an unavoidable tradeoff between optimal color and highest efficiency. Furthermore, the N^C^N complexes and other tridentate analogs require $Cl^-$ or other monoanionic ligands as the fourth coordinating ligand which may be potentially unstable so a new molecular design motif is needed.[103.104] In this chapter, a series of tetradentate Pt complexes based on a phenyl methyl-imidazole emissive ligand were synthesized (Figure 29) which demonstrate efficient emission from both the excimer and monomer achieving a peak EQEs of 24% ± 2% for all three emitters at concentrations from 2% to 16%. The effect of small structural changes to the ligand on the monomer and excimer emission properties were also studied with this class of emitters as well as the operational stability of an excimer emitting species. A device employing Pt2O2, in particular, achieved a device operational lifetime to 80% initial luminance estimated at over 200 hours at 1000cd/$m^2$ while also achieving 12.5% peak EQE, CIE of (0.46,0.47), and a CRI of 80. Based on this concept, a new excimer emitting Pd(II) complex (Pd3O3) was also synthesized and discussed in the second section in this chapter. The last section in the chapter, A novel

green light emitting material(PtOO8) was synthesized and utilized for all platinum complex based

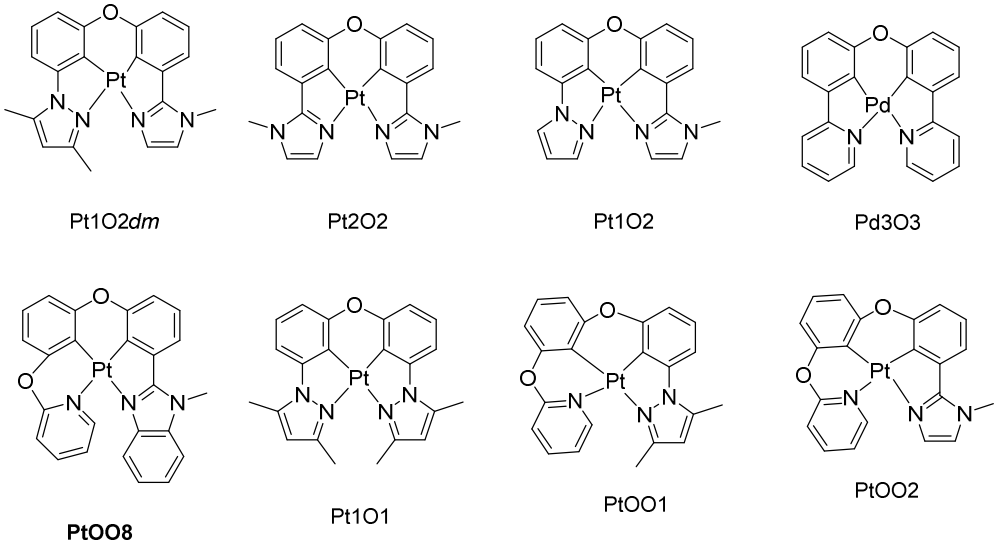


Figure 29 Chemical structures and abbreviations of Pt complexes discussed in this chapter

3.2 Synthesis and Structural Characterization

All commercial reagents were purchased and used as received without further purification. $K_2PtCl_4$ was purchased from Aldrich Chemical. $^nBu_4NBr$ and CuI were purchased from Aldrich Chemical. Silica gel (40-60μm) was purchased from Agela Technologies and BDH. The solvent, N,N-Dimethylacetamide (DMAc), was purchased from Sigma Aldrich.

$^1H$ spectra were recorded at 400 MHz, $^{13}C$ NMR spectra were recorded at 100 MHz on Varian Liquid-State NMR instruments in DMSO-$d_6$ solutions. $^1H$ NMR spectra were recorded with residual solvent peak (δ = 2.50 ppm) as internal reference; $^{13}C$ NMR spectra were recorded with DMSO-d6 (δ = 39.52 ppm) as internal reference. The following abbreviations (or combinations thereof) were used to explain $^1H$ NMR ultiplicities: s = singlet, d = doublet, t = triplet, m = multiplet. Mass spectra were

recorded on a Voyager DE-STR MALDI-TOF mass spectrometer from Applied Biosystems. Photoluminescent emission spectra were performed on a Horiba Jobin Yvon FluoroLog-3 at room temperature and 77K in a solution of dichloromethane. The absolute PL quantum efficiency measurements of doped thin films were carried out on a Hamamatsu C9920 system equipped with a xenon lamp, integrating sphere and a model C10027 photonic multi-channel analyzer. The redox potentials are based on the values measured from differential pulsed voltammetry using a CHI610B electrochemical analyzer in a solution of anhydrous DMF (Aldrich) with 0.1 M tetra(n butyl) ammonium hexafluorophosphate as the supporting electrolyte and are reported relative to a ferrocene/ferrocenium (Fc/Fc+) redox couple used as an internal reference. A silver wire was used as the pseudo reference electrode, a Pt wire was used as the counter electrode, and glassy carbon was used as the working electrode.

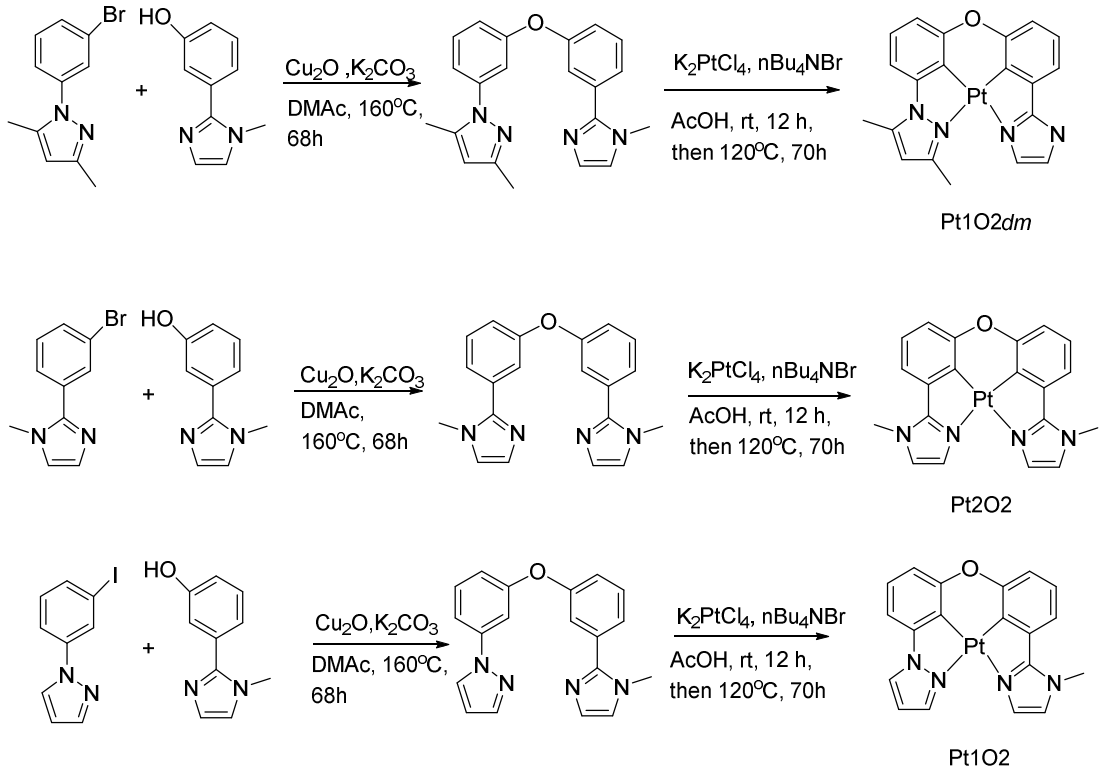


Figure 30 Synthetic routes for Pt1O2dm, Pt2O2 and Pt1O2

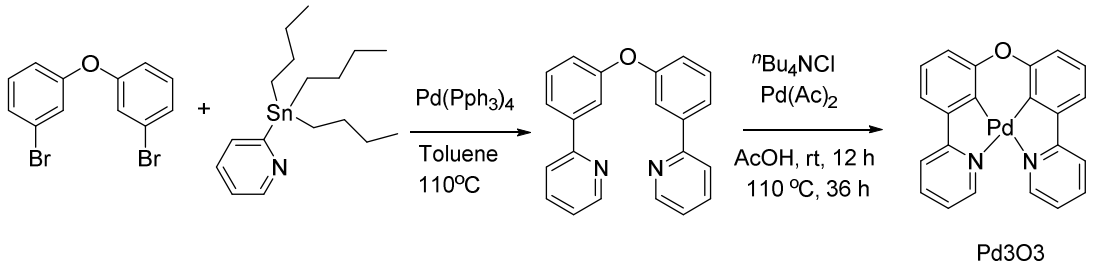


Figure 31 Synthetic route for Pd3O3.

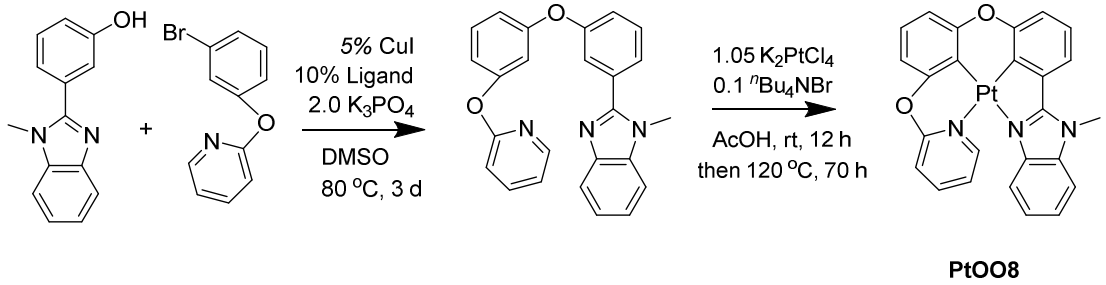


Figure 32 Synthetic route for PtOO8.

Synthesis of 3,5-dimethyl-1-(3-(3-(1-methyl-1*H*-imidazol-2-yl)phenoxy)phenyl)-1*H*-pyrazole: To a three-neck round bottom flask were added 1-(3-bromophenyl)-3,5-dimethyl-1*H*-pyrazole (810 mg, 3.3 mmol), 3-(1-methyl-1*H*-imidazol-2-yl)phenol (520mg, 3 mmol), $Cu_2O$ (43.2 mg, 0.3 mmol) and $K_2CO_3$ (1.04 g, 7.5 mmol). The flask was evacuated and backfilled with nitrogen for three times and DMAc (60 ml) was added under the protection of nitrogen, the reaction mixture was stirred at 160 $^oC$ under nitrogen atmosphere for 68 hours. After cooling to room temperature, the solid was filtered off through a pad of celite. The filtrate was poured into water, extracted with ethyl acetate (50 ml × 3). The combined organic layer was dried with anhydrous $Na_2SO_4$, filtered and concentrated under reduced pressure. The residue was purified by column chromatography on silica gel (DCM: methanol 15:1) to afford the desired product as light brown solid (825 mg, 80%) $^1H$ NMR (DMSO-$d_6$, 400 MHz): δ 2.15 (s, 3H), 2.30 (s, 3H), 3.75 (s, 3H), 6.05 (s, 1H), 6.96 (d, $J$ = 1.2 Hz, 1H), 7.06 (dd, $J$ =, 8.0, 2.8 Hz, 1H), 7.12-7.17 (m, 2H), 7.25 (d, $J$ = 0.8 Hz, 1H ), 7.28 (dd, $J$ =, 8.0, 2.0 Hz, 1H), 7.35-7.38 (m, 1H), 7.47-7.55 (m, 3H).

Synthesis of Pt1O2d*me* To a 100 ml three-neck round bottom flask were added 3,5-dimethyl-1-(3-(3-(1-methyl-1*H*-imidazol-2-yl)phenoxy)phenyl)-1*H*-pyrazole (172 mg, 0.5 mmol), potassium tetrachloroplatinate (218 mg, 0.52 mmol) and $^nBu_4NBr$(16.1 mg, 0.05 mmol). The flask was evacuated and backfilled with nitrogen for three times and acetic acid (30 ml) was added under the protection of nitrogen. The reaction mixture was stirred at ambient temperature for 12 hours and then followed at 120 $^oC$ for another 70 hours under nitrogen atmosphere. After cooling to room temperature, the mixture was poured into 50 ml of water. The precipitate was collected through filtration, washed with water for three

times and dried in air. The collected solid was purified by column chromatography on silica gel using dichloromethane as eluent to obtain a crude product, recrystallized in dichloromethane and ether to afford the desired platinum compound as a yellow solid (205 mg, 77%). $^1$H NMR (DMSO-$d_6$, 400 MHz): δ ): δ 2.67 (s, 3H), 2.74 (s, 3H), 4.10 (s, 3H), 6.43 (s, 1H), 6.90 (d, $J$ = 7.6 Hz, 1H), 7.01 (d, $J$ =, 8.0, 1H), 7.14-7.23 (m, 2H), 7.26 (d, $J$ = 8 Hz, 1H ), 7.44-7.50 (m, 3H). $^{13}$C NMR (DMSO-$d_6$, 100 MHz): δ 14.44, 14.81, 35.61, 106.66, 110.01, 112.73, 113.06, 116.37, 117.32, 123.48, 123.81, 123.89, 123.94, 128.51, 137.89, 141.34, 147.21, 150.25, 150.51, 151.46, 155.58. MS (MALDI) for $C_{21}H_{18}N_4OPt$ $[M]^+$: calcd 537.1, found 537.4.

Synthesis of 1-methyl-2-(3-(3-(1-methyl-1*H*-imidazol-2-yl)phenoxy)phenyl)-1*H*-imidazole: To a three-neck round bottom flask were added 2-(3-bromophenyl)-1-methyl-1*H*-imidazole (1.14 g, 4.0 mmol), 3-(1-methyl-1*H*-imidazol-2-yl)phenol (765 mg, 4.4 mmol), $Cu_2O$ (57.2 mg, 0.4 mmol) and $K_2CO_3$ (1.38 g, 10 mmol). The flask was evacuated and backfilled with nitrogen for three times and DMAc (80 ml) was added under the protection of nitrogen, then the reaction mixture was stirred at 160 $^o$C under nitrogen atmosphere for 68 hours. After cooling to room temperature, the solid was filtered off through a pad of celite. The filtrate was poured into water, extracted with ethyl acetate (50 ml×3). The combined organic layer was dried with anhydrous $Na_2SO_4$, filtered and concentrated under reduced pressure. The residue was purified by column chromatography on silica gel (DCM: methanol 15:1) to afford the desired product as light brown solid (1.05 g, 80%). $^1$H NMR (DMSO-$d_6$, 400 MHz): δ 3.75 (s, 6H), 6.95 (s, 2H), 7.13 (d, $J$ = 8.0 Hz, 2H), 7.24 (s, 2H), 7.35 (s, 2H), 7.46-7.54 (m, 4H).

synthesis of Pt 2O2: To a 100 ml three-neck round bottom flask were added 1-methyl-2-(3-(3-(1-methyl-1*H*-imidazol-2-yl)phenoxy)phenyl)-1*H*-imidazole (165 mg, 0.5 mmol), potassium tetrachloroplatinate (218 mg, 0.52 mmol), and $^{n}Bu_4NBr$(16.1 mg, 0.05 mmol). The flask was evacuated and backfilled with nitrogen for three times and acetic acid (30 ml) was added under the protection of nitrogen. The reaction mixture was stirred at ambient temperature for 12 hours and then followed at 120 °C for another 70 hours under nitrogen atmosphere. After cooling to room temperature, the mixture was poured into 50 ml of water. The precipitate was collected through filtration, washed with water for three times and dried in air. The collected solid was purified by column chromatography on silica gel using dichloromethane as eluent to obtain a crude product, recrystallized in dichloromethane and ether to afford the desired platinum compound as a yellow solid (215 mg, 82%). $^{1}$H NMR (DMSO-$d_6$, 400 MHz): δ 4.07 (s, 6H), 6.97 (d, $J$ = 8.4 Hz, 2H), 7.14 (dd, $J$ = 15.6, 8.0 Hz, 2H), 7.37 (d, , $J$ =7.2 Hz, 2H), 7.45 (s, 2H), 7.53 (d, $J$ =1.2 Hz, 2H). ). $^{13}$C NMR (DMSO-$d_6$, 100 MHz): δ 35.15, 116.30, 117.25, 123.20, 126.70, 123.58, 138.19, 150.98, 155.70. MS (MALDI) for $C_{20}H_{16}N_4OPt$ $[M]^+$: calcd 524.1, found 524.2.

Synthesis of 1-(3-(3-(1-methyl-1*H*-imidazol-2-yl)phenoxy)phenyl)-1*H*-pyrazole: To a three-neck round bottom flask were added 1-(3-iodophenyl)-1*H*-pyrazole (972 mg, 3.6 mmol), 3-(1-methyl-1*H*-imidazol-2-yl)phenol (520 mg, 3 mmol), $Cu_2O$ (43.2 mg, 0.3 mmol) and $K_2CO_3$ (1.04 g, 7.5 mmol). The flask was evacuated and backfilled with nitrogen for three times and DMAc (60 ml) was added under the protection of nitrogen, the reaction mixture was stirred at 160 °C under nitrogen atmosphere for 68 hours. After cooling to room temperature, the solid was filtered off through a pad of celite, the filtrate

was poured into water, then extracted with ethyl acetate (50 ml× 3). The combined organic layer was dried with anhydrous $Na_2SO_4$, filtered and concentrated under reduced pressure. The residue was purified by column chromatography on silica gel (DCM: methanol 15:1) to afford the desired product as a pale solid (762 mg, 80%). $^1$H NMR (DMSO-$d_6$, 400 MHz): δ 3.76 (s, 3H), 6.53-6.57 (m, 1H), 6.99 (dd, $J$ = 8.4, 1.6 Hz, 1H), 7.14-7.20 (m, 1H), 7.18-7.52(m, 7H), 7.66 (dd, $J$ = 7.6, 0.8 Hz, 1H), 7.73 (d, $J$ = 1.6 Hz, 1H), 8.55 (d, $J$ = 2.0 Hz, 1H).

Synthesis of Pt1O2 To a 100 ml three-neck round bottom flask were added added 1-(3-(3-(1-methyl-1*H*-imidazol-2-yl)phenoxy)phenyl)-1*H*-pyrazole (380 mg, 1.2 mmol), potassium tetrachloroplatinate (524 mg, 1.26 mmol) and $^n$Bu$_4$NBr (38 mg, 0.12 mmol). The flask was evacuated and backfilled with nitrogen for three times and acetic acid (60 ml) was added under the protection of nitrogen. The reaction mixture was stirred at ambient temperature for 12 hours and then followed at 120 $^o$C for another 70 hours under nitrogen atmosphere. After cooling to room temperature, the mixture was poured into 100 ml of water. The precipitate was collected through filtration, washed with water for three times and dried in air. The collected solid purified by column chromatography on silica gel using dichloromethane as eluent to obtain a crude product, recrystallized in dichloromethane and ether to afford the desired platinum compound as a yellow solid 220 mg, 36%). $^1$H NMR (DMSO-d6, 400 MHz): δ 4.08 (s, 3H), 6.80 (dd, J = 6.5, 2 Hz, 1H), 6.91 (d, J = 7.6 Hz, 1H), 7.01 (d, J = 8.4 Hz, 1H), 7.14-7.20 (m, 2H), 7.41 (d, J = 8.0 Hz, 2H), 7.48 (d, J = 1.2 Hz, 1H), ), 7.65 (d, J = 1.2 Hz, 1H), ), 8.38 (d, J = 1.6 Hz, 1H), 8.79 (d, J = 3.5 Hz, 1H). 13C NMR (DMSO-d6, 100 MHz): δ 35.19, 105.88, 107.78, 113.16, 116.01, 116.59, 117.54,

123.71, 123.81, 123.92, 124.51, 126.81, 128.30, 138.12, 141.37, 146.09, 150.98, 151.71, 155.35. MS (MALDI) for C19H14N4OPt [M]+: calcd 509.1, found 509.3.

Synthesis of 2-(3-(3-(pyridin-2-yl)phenoxy)phenyl)pyridine To a 100 mL three-neck round-bottom flask were added 1-bromo-3-(3-bromophenoxy)benzene (656 mg, 2 mmol) and 2-(tributylstannyl)pyridine (1.76 g, 4.8 mmol), the flask was evacuated and backfilled with nitrogen for three times, Tetrakis(triphenylphosphine)palladium(0) (115 mg, 0.1 mmol) and Toluene (20 mL) was added under the protection of nitrogen, the reaction mixture was stirred at 110 $^{o}$C under nitrogen for 24 hours. After cooling to room temperature, the mixture was poured into 50 mL of water and extracted with ethyl acetate (100 mL*3), the combined organic layer was dried with anhydrous Na2SO4 and concentrated under reduced pressure. Purification by column chromatography (hexane: ethyl acetate=5:1) afford the desired product as white solid (550 mg, 84%) 1H NMR (DMSO-d6, 400 MHz): 7.16 (dd, J = 8.0 Hz, 2.4 Hz, 2 H), 7.33-7.38 (m, 2 H), 7.54 (t, J = 7.6 Hz, 2 H), 7.79 (m, 2 H), 7.85-7.91(m, 4 H), 7.98(d, J = 8 Hz, 2 H), 8.63(d, J = 4.4 Hz, 2 H)

Synthesis of Palladium (II) 2-(3-(3-(pyridin-2-yl)phenoxy)phenyl)pyridine(Pd3O3). 2-(3-(3-(pyridin-2-yl)phenoxy)phenyl)pyridine (470 mg, 1.45 mmol), $Pd(OAc)_2$ (348 mg, 1.55 mmol), and n-$Bu_4NBr$(48 mg, 0.149 mmol) were added into a 100ml three-neck round-bottom flask, then 30ml acetic acid was added. The mixture was bubbled with nitrogen for 30 minutes then stirred at ambient temperature for 12 hours. The mixture was heated in an oil bath at a temperature of 110 $^{o}$C for another 72 hours. 100 ml of water was added

after the mixture was cooled down to room temperature. The precipitate was collected through filtration, washed with water for three times then dried in air. The collected solid was purified through column chromatography on silica gel using dichloromethane as eluent to afford the desired Palladium complex Pd3O3 as a light yellow solid 390 mg in 63% yield. 1H NMR (DMSO-d6, 400 MHz): 7.16 (d, J = 7.6 Hz, 2 H), 7.27 (t, J = 8.0 Hz, 2 H), 7.55 (t, J = 6.4 Hz, 2 H), 7.74 (d, J = 7.2 Hz 2 H), 8.09-8.15 (m, 2 H), 8.28 (d, J = 8.4 Hz, 2 H), 8.96(d, J = 5.2 Hz, 2 H),

Synthesis of 2-(3-methoxyphenyl)-1-methyl-1H-benzo[d]imidazole :To a three-neck round-bottom flask, added 1-iodo-3-methoxybenzene(2.24g, 12.0 mmol, 1.2 eq), 1-methyl-1H-benzo[d]imidazole(1.32 g, 10.0 mmol, 1.0 eq), Pd(dppf)Cl2 (410 mg, 0.5 mmol, 0.05 eq), triphenylphosphine(262 mg, 1.0 mmol, 0.1 eq) and Ag2CO3(5.52 g, 20.0 mmol, 2.0 eq). The flask was evacuated and backfilled with nitrogen for three times and then CH3CN (60 mL) was added under the protection of nitrogen. The mixture was stirred at a temperature of 60-70$^{o}$C for 24 hours. After cooling to room temperature, the solid was filtered off with a pad of celite, the filtrate was poured into water and extracted with ethyl acetate (50 mL×3). The combined organic layer was dried with anhydrous Na2SO4, filtered and the filtrate was concentrated under reduced pressure. The residue was purified by column chromatography (eluent: hexane: ethyl acetate = 5:2) to afford the desired product 2-(3-methoxyphenyl)-1-methyl-1H-benzo[d]imidazole 5 as white solid 1.4 g in 61% yield. 1H NMR (DMSO-d6, 400 MHz): δ 3.84 (s, 3H), 3.89 (s, 3H), 7.10-7.15 (m, 1H), 7.24 (td, J = 7.6, 1.2 Hz, 1H), 7.30 (td, J = 7.2, 1.2 Hz 1H), 7.36-7.42 (m, 2H), 7.49 (t, J = 8.0 Hz, 1H), 7.61 (d, J = 8.0 Hz, 1H ), 7.68 (d, J = 8.0 Hz, 1H).

Synthesis of 3-(1-methyl-1H-benzo[d]imidazol-2-yl)phenol :2-(3-Methoxyphenyl)-1-methyl-1H-benzo[d]imidazole 5 (1.4 g, 62 mmol), acetic acid (15 mL) and HBr (15 mL) were added to a 100 mL three-neck round-bottom flask the mixture was refluxed for 24 hours. After cooling to room temperature, the mixture was diluted with water and then Na2CO3 was added slowly to neutralize the acid and the resulting suspension was filtered off. The collected solid was washed with water for three times, dried in air under reduced pressure to get the desired product 3-(1-methyl-1H-benzo[d]imidazol-2-yl)phenol 6 as a white powder 1.3 g in 95% yield. 1H NMR (DMSO-d6, 400 MHz): δ 3.88 (s, 3H), 6.96-7.02 (m, 1H), 7.19-7.26 (m, 2H), 7.34-7.45 (m, 3H), 7.69 (d, J = 8.4 Hz, 1H), 7.75 (d, J = 7.6 Hz, 1H), 9.93 (s, 1H).

Synthesis of 1-methyl-2-(3-(3-(pyridin-2-yloxy)phenoxy)phenyl)-1H-benzo[d]imidazole To a 100 mL three-neck round-bottom flask, added 3-(1-methyl-1H-benzo[d]imidazol-2-yl)phenol 6 (336 mg, 1.5 mmol, 1.0 eq), 2-(3-bromophenoxy)pyridine (450 mg, 1.8 mmol, 1.2 eq), CuI (29 mg, 0.15 mmol, 0.1 eq), 2-Picolinic acid (37 mg, 0.3 mmol, 0.2 eq) and K3PO4 (639 mg , 3 mmol, 2.0 eq). The flask was evacuated and backfilled with nitrogen for three times and DMSO (30 mL) was added under the protection of nitrogen. The mixture was stirred at 80 ºC for three days. After cooling to room temperature, the mixture was poured into 100 mL of water and extracted with ethyl acetate (100 mL×3), the combined organic layer was dried with anhydrous Na2SO4, filtered and the filtrate was concentrated under reduced pressure. The residue was purified by column chromatography (dichloromethane: methanol = 20:1) to afford the desired product as white solid 460 mg in 78% yield. 1H NMR (DMSO-d6, 400 MHz): δ 3.86 (s, 3H), 6.87 (t, J = 2.4 Hz, 1H), 6.91-

6.95 (m, 2H), 7.04 (d, J = 8.4 Hz, 1H), 7.11-7.15 (m, 1H), 7.22-7.32 (m, 3H), 7.44 (t, J = 8.0 Hz, 1H), 7.49 (s, 1H), 7.57-7.69 (m, 4H), 7.82-7.87 (m, 1H), 8.13-8.15 (m, 1H).

Synthesis of 1-methyl-2-(3-(3-(pyridin-2-yloxy)phenoxy)phenyl)-1H-benzo[d]imidazole platinum(PtOO8):1-Methyl-2-(3-(3-(pyridin-2-yloxy)phenoxy)phenyl)-1H-benzo[d]imidazole (460 mg, 1.17 mmol, 1.0 eq), K2PtCl4 (510 mg, 1.23 mmol, 1.05 eq), and nBu4NBr (38 mg, 1.17mmol, 0.1 eq) were added to a 100 mL three-neck round-bottom flask. The flask was evacuated and backfilled with nitrogen, this evacuation and backfill procedure was repeated for another twice. Then solvent acetic acid (60 mL) was added under the protection of nitrogen. The reaction mixture was stirred at room temperature for 12 hours and then fellowed at a temperature of 120 ºC for another 70 hours. After cooling to room temperature, water (50 mL) was added. The precipitate was collected through filtration, washed with water for three times and dried in air. The collected solid was purified by column chromatography on silica gel using dichloromethane as eluent afford a crude product, which recrystallized in dichloromethane and ether to afford the desired platinum compound PtOO8 as a yellow solid 570 mg in 83%. 1H NMR (DMSO-d6, 400 MHz): δ 4.31 (s, 3H), 6.90 (dd, J = 8.0, 2.0 Hz, 1H), 6.93 (d, J = 8.4 Hz, 1H), 7.06 (d, J = 8.0 Hz, 1H), 7.10 (d, J = 7.6 Hz, 1H), 7.27-7.30 (m, 3H), 7.37-7.42 (m, 2H), 7.61 (d, J = 8.0 Hz, 1H), 7.80 (d, J = 8.0 Hz, 1H), 7.89 (d, J = 8.0 Hz, 1H), 8.22-8.27 (m, 1H), 8.94 (dd, J = 5.6, 2.0 Hz, 1H). MS (MALDI) for C25H17N3O2Pt [M]+: calcd 586.1, found 586.2.

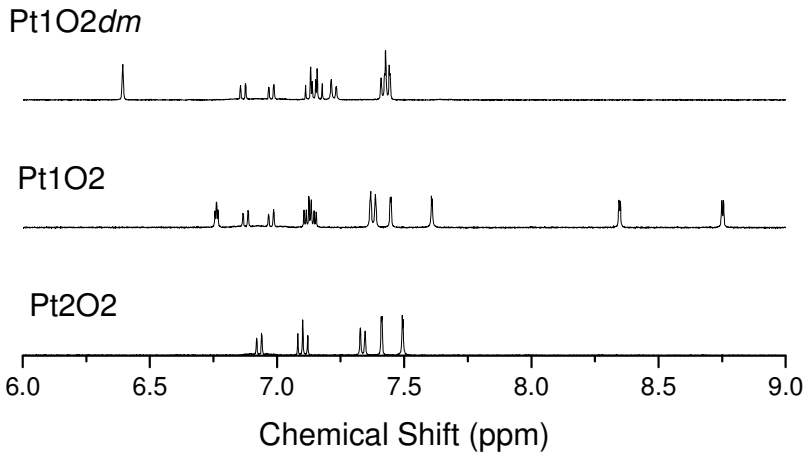


Figure 33 $^{1}$H NMR spectra (DMSO-d6, 400 MHz) of Pt1O2dm, Pt1O2 and Pt2O2.

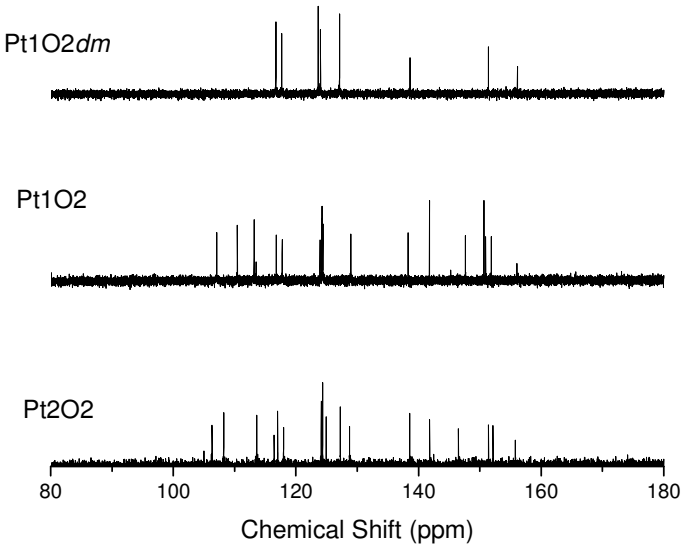


Figure 34 $^{13}$C NMR spectra (DMSO-d6, 400 MHz) of Pt1O2dm, Pt1O2 and Pt2O2.

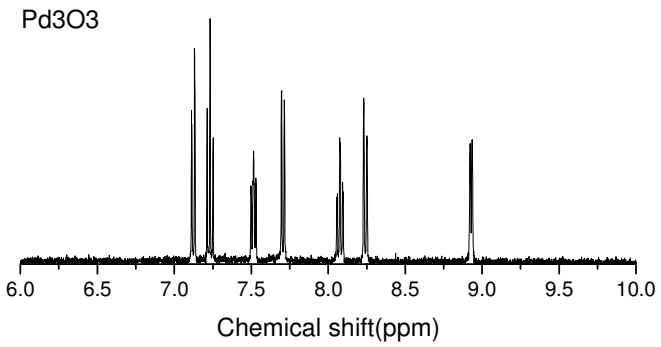


Figure 35 . $^{1}$H NMR spectra (DMSO-d6, 400 MHz) of Pd3O3.

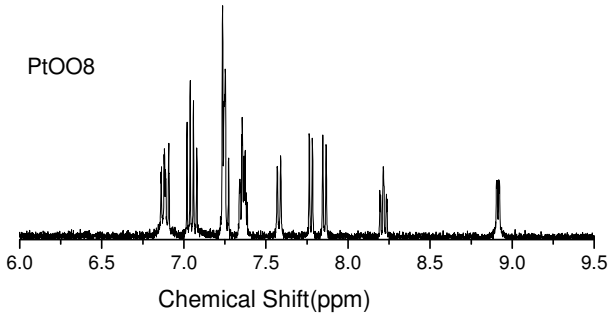


Figure 36 $^{1}$H NMR spectra (DMSO-d6, 400 MHz) of PtOO8.

3.3 Result and Discussion

3.3.1 Photophysical Properties

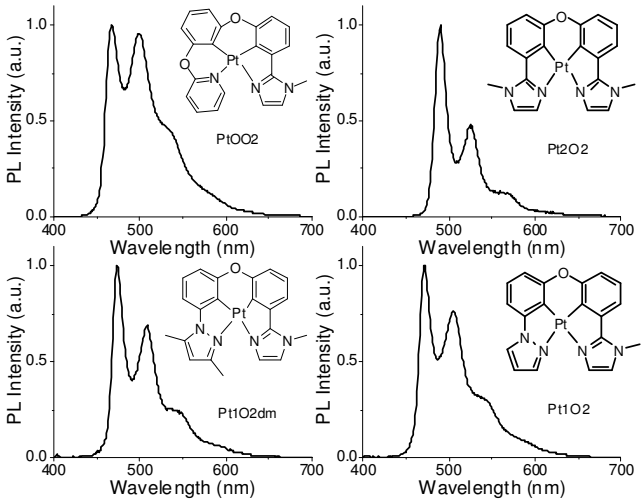


Figure 37 The chemical structures (inset) and emission spectra of PtOO2, Pt1O2, Pt2O2 and Pt1O2dm at room temperature in a solution of $CH_2Cl_2$

The previously reported blue emitter PtOO2 (Figure 37a) demonstrated a broad blue emission with emission onset just below 450 nm and a primary emission peak at 470 nm which should serve well for stable and efficient white lighting due to its blue color and compatibility with the triplet energy of many stable host materials.[105] However, no excimer formation is observed for this complex due to the out of plane distortion of this class of tetradentate emitters. Recently, a symmetric tetradentate platinum complex, Pt7O7, employed a new design motif which improved the planarity for enhanced molecular stacking and demonstrated both efficient monomer and excimer emission.[106]

Following the symmetric, planar backbone exhibited in Pt7O7, the complex Pt2O2 (Figure 37 b) was synthesized. Despite retaining the same phenyl methyl-imidazole cyclometalating ligand as PtOO2, the primary emission peak of Pt2O2 was red shifted by 20nm to 490nm which reduces the blue component of the emission spectrum, but such a molecule may still prove useful as an excimer based white OLED.

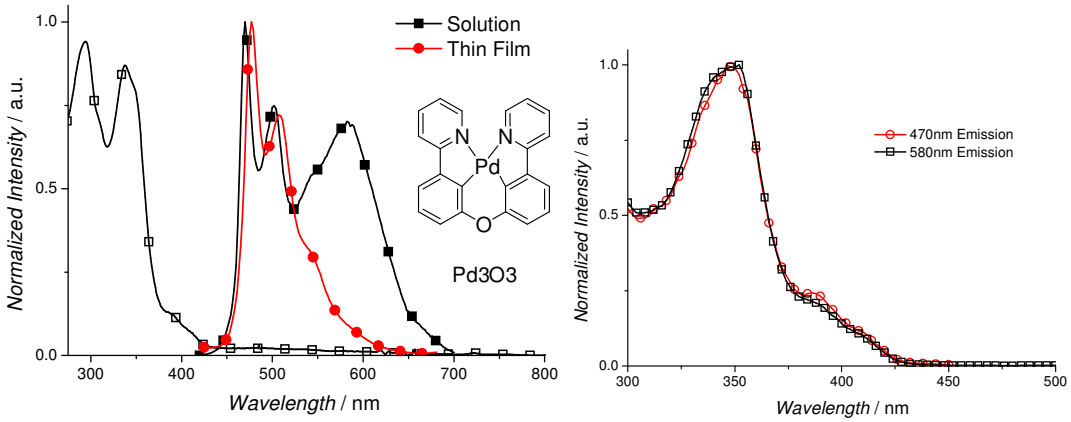


Figure 38 (a)The chemical structure (inset) and absorption (open squares) and PL spectra of Pd3O3 in a solution of DCM (solid squares) and a 1% doped 26mCPy film (solid circles). (b) Excitation spectra for a solution of Pd3O3 in dichloromethane with emission measured at 470nm (circles) and 580nm (squares).

Both a dilute solution of Pd3O3 in dichloromethane (DCM) and a dilute thin film (1% by weight) in 2,6-bis(N-carbazolyl) pyridine (26mCPy) were prepared for spectral analysis. The absorption of the solution is shown in Figure 38 (a). The strong absorption peaks below ~360nm are assigned to $^1\pi$-$\pi^*$ transitions, localized on the phenyl-pyridine ligands. The small shoulder in the 360-450 nm range is assigned to singlet metal to ligand charge transfer ($^1$MLCT) transitions. Both the thin film and solution sample show molecular emission peaks in 450-550 nm range. The spectrum of the 1% Pd3O3 doped thin film shows an emission onset near 450 nm with a primary emission peak at 477 nm and a second peak at 507 nm. Unfortunately, due to strong intermolecular interactions, all

prepared solutions formed suspensions of small molecular aggregates. Consequently, the solution sample contained a large, broad aggregate emission which peaks at 582nm. This low energy emission band is attributed to excimer emission which is supported by the excitation spectra which showed a shared origin for both the monomer and aggregate emission Figure 38 (b).

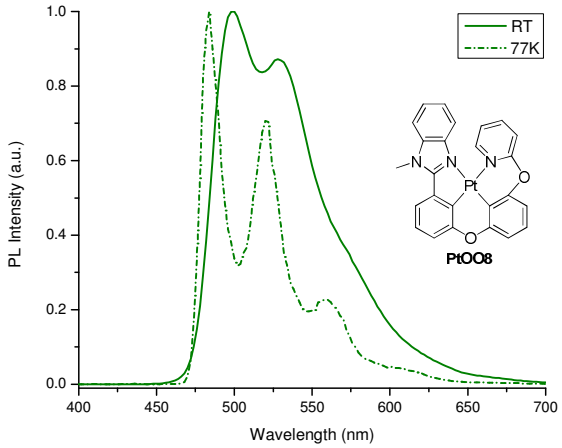


Figure 39. Room temperature (solid) and 77K (short dash dot) emission spectra and chemical structure (inset) of PtOO8.

PtOO8 complexes is highly luminescent in degassed solution, emitting green light (Figure 39). The vibrionic progressions found at cryogenic temperatures for PtOO8 remain intact.

3.3.2 Tetradentate Platinum Complexes for Efficient and Stable Excimer Based White OLEDs

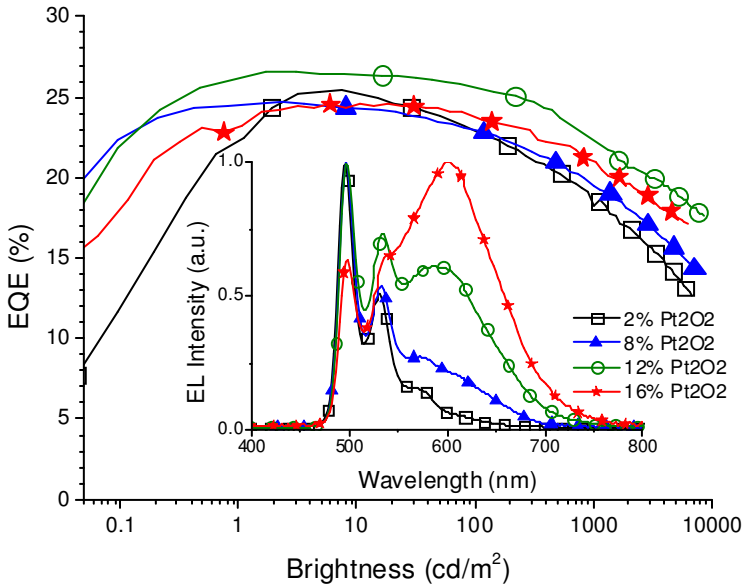


Figure 40 The EQE versus brightness plots for Pt2O2 devices in the structure: ITO/HATCN (10nm)/NPD (40nm)/TAPC (10nm)/x% Pt2O2: 26mCPy (25nm)/DPPS (10nm)/BmPyPB (40nm)/LiF (1nm)/ Al for 2% (squares), 8% (triangles), 12% (circles), and 16% (stars). The corresponding EL spectra are inset.

Devices of Pt2O2 were fabricated in the structure of ITO/HATCN(10 nm)/NPD(40 nm)/TAPC(10 nm)/x% Pt2O2: 26mCPy(25 nm)/DPPS(10 nm)/BmPyPB(40 nm)/LiF/Al where HATCN is 1,4,5,8,9,11-hexaazatriphenylene-hexacarbonitrile, NPD is N,N'-diphyenyl-N,N'-bis(1-naphthyl)-1,1'-biphenyl-4,4"-diamine, TAPC is di-[4-(N,N-di-toylyl-amino)-phyenyl]cyclohexane, 26mCPy is 2,6-bis(N-carbazolyl) pyridine, DPPS is diphenyl-bis[4-(pyridin-3-yl)phenyl]silane, and BmPyPB is 1,3-bis[3, 5-di(pyridin-3-yl)phenyl]benzene.[22] For blue OLED devices with primarily monomeric emission character, the dopant concentration was controlled to be around 2% (w/w) to minimize the formation of excimers. The monochromatic devices demonstrated a very high peak EQE of 25.4% shown in Figure 40 and Table 5 and a peak power efficiency of 57.0 Lm/W. These efficiencies represent electron to photon conversion efficiencies approaching unity and are amongst the highest of any OLEDs without light outcoupling

techniques. The electroluminescent spectrum, shown in the inset to Figure 40, demonstrated green emission with a primary peak at 496nm and CIE coordinates of (0.231, 0.565).

Table 5 Performance parameters of devices in the structure: ITO/HATCN (10nm)/NPD (40nm)/TAPC (10nm)/x% emitter:26mCPy (25nm)/DPPS (10nm)/BmPyPB(40)/LiF/Al

| | | | | Peak | | | 1000 cd/m$^2$ | | |
|---|---|---|---|---|---|---|---|---|---|
| Dopant | Conc. (% w/w) | CIE$^{\dagger}$ | CRI$^{\dagger}$ | $\eta_{EQE}$ (%) | $\eta_{PE}$ (Lm/W) | $\eta_{A}$ (Cd/A) | $\eta_{EQE}$ (%) | $\eta_{PE}$ (Lm/W) | $\eta_{A}$ (Cd/A) |
| Pt2O2 | 2 | (0.231,0.565) | -- | 25.4 | 57.1 | 70.6 | 18.2 | 27.2 | 50.5 |
| | 8 | (0.327,0.536) | 42 | 24.6 | 58.5 | 66.6 | 19.6 | 28.2 | 52.9 |
| | 12 | (0.411,0.512) | 58 | 26.5 | 61.4 | 69.8 | 20.1 | 29.8 | 52.9 |
| | 14 | (0.450,0.489) | 68 | 24.1 | 50.9 | 59.6 | 21.4 | 29.9 | 52.8 |
| | 16 | (0.475,0.478) | 72 | 22.4 | 48.7 | 53.6 | 19.2 | 25.0 | 46.0 |
| Pt1O2 | 2 | (0.215,0.438) | -- | 24.1 | 47.6 | 55.8 | 16.9 | 20.0 | 38.9 |
| | 8 | (0.359,0.455) | 61 | 23.6 | 51.4 | 61.9 | 17.7 | 24.7 | 46.5 |
| | 12 | (0.454,0.480) | 61 | 23.1 | 53.5 | 64.7 | 18.5 | 27.5 | 51.6 |
| | 16 | (0.485,0.479) | 57 | 22.6 | 48.7 | 63.2 | 19.3 | 28.8 | 53.9 |
| Pt1O2 $me_2$ | 2 | (0.229,0.440) | -- | 26.5 | 58.0 | 68.0 | 17.6 | 24.2 | 45.3 |
| | 4 | (0.318,0.496) | 44 | 26.7 | 68.3 | 80.3 | 17.6 | 28.5 | 53.1 |
| | 6 | (0.354,0.513) | 45 | 24.7 | 69.0 | 76.9 | 17.7 | 31.0 | 55.1 |
| | 12 | (0.416,0.528) | 44 | 24.2 | 68.2 | 78.7 | 20.4 | 35.7 | 66.2 |
| | 16 | (0.422,0.531) | 42 | 24.2 | 69.0 | 79.9 | 20.6 | 35.4 | 67.9 |

As the Pt2O2 dopant concentration is increased to 8%, 12%, and 16% the formation of a broad, red-shifted emission peak appears in the EL spectra (Figure 40 inset) which is attributed to the increased formation of excimers at the higher concentrations. This is in contrast to the observed concentration behavior of many other tetradentate platinum complexes such as PtOO2 and analogs.[105] This can be explained by the suspected planar nature of the Pt2O2 molecules compared to the twisted, non-planar geometry of PtOO2

shown in the previous report.[107] Ultimately, an orange-white emission with CIE coordinates of (0.48,0.48) and CRI of 72 is achieved at a concentration of 16% Pt2O2. These moderate CRI values are achieved in spite of the lack of a portion of the blue emission spectrum due to the broad and balanced emission color across the rest of the visible range. Furthermore, it is very encouraging that both the monomer and excimer species are very efficient as evidenced by the very high peak EQE values at all concentrations with the highest achieved peak EQE value of 26.5% for 12% Pt2O2 doped devices and remaining as high as 24.6% for 16% doped devices. These high efficiencies are comparable or superior to the previously reported Pt7O7 emitter indicating that this design motif is both extremely efficient and color tunable through small structural modifications.[106]

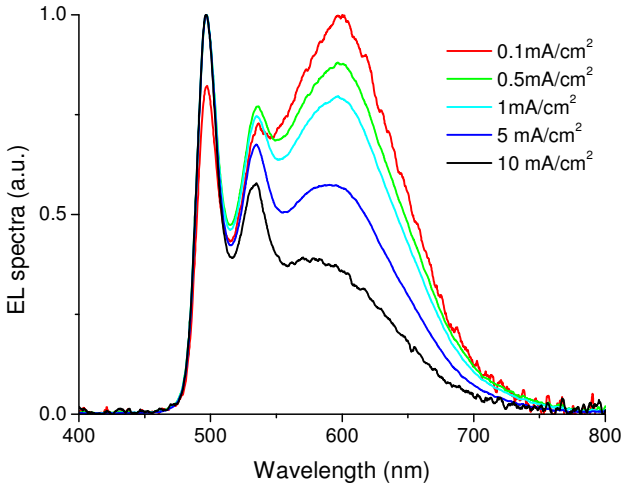


Figure 41 The EL spectra as a function of current density for the device: ITO/HATCN (10nm)/NPD (40nm)/TAPC (10nm)/14% Pt2O2: 26mCPy (25nm)/DPPS (10nm)/BmPyPB (40nm)/LiF (1nm)/ Al.

The high efficiency of this emitter is further supported by the photoluminescent quantum yields (PLQY) of 0.84 and 0.61 in thin films at dopant concentrations of 2% and 14%, respectively. Nevertheless, the PLQY may give only part of the story since it is possible

that a significant portion of excimers are generated directly from charge transfer between neighboring anion and cation species as opposed to going through an excited monomer intermediate. The existence of charge transfer generated excimers in these devices is evidenced by the large current density dependence in the emission spectrum (Figure 41) in contrast to many previous reports of excimer emitters. Uncovering the nature of excimer formation and the effect of molecular structure on the various formation mechanisms is a challenging and important task and is under continued study.

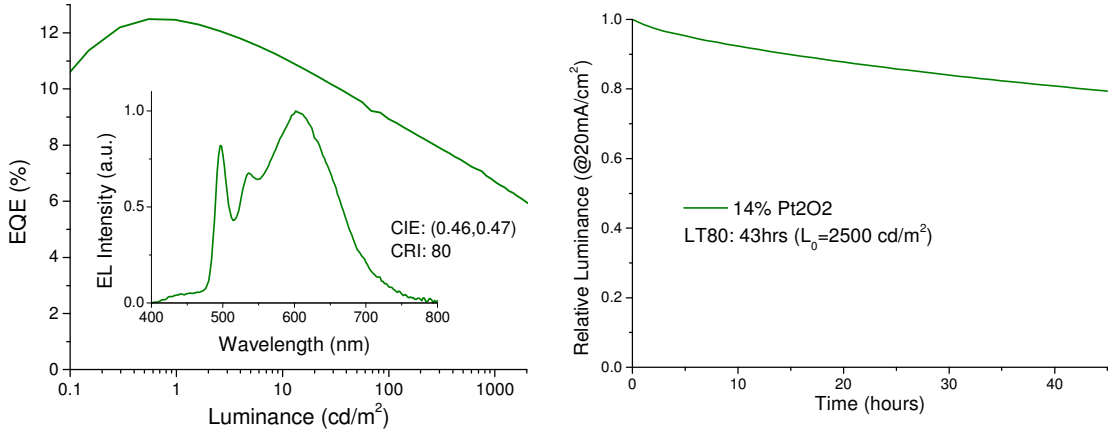


Figure 42. Plots of (a) EQE vs. luminance and EL spectrum at 1mA/cm$^2$ (inset) and (b) luminance intensity versus time at a constant driving current of 20mA/cm$^2$ and $LT_{80}$ values are given in the inset for the device of ITO/HATCN (10nm)/NPD (40nm)/ 16% Pt2O2: CBP (25nm)/BAlq (10nm)/Alq (30nm)/LiF (1nm)/ Al.

To further explore the effectiveness of excimer emitting platinum emitters, such as Pt2O2, as a commercially viable white light source, the device operational lifetime must also be evaluated. Unfortunately, many of the organic materials including the electron and hole blockers are known to dramatically reduce device stability due to electrochemical degradation.[108] In particular, the efficient device structure employing

TAPC and DPPS layers is unsuitable for device operational lifetime testing, as demonstrated previously.[109] Consequently, a known stable, albeit inefficient, structure of ITO/HATCN (10nm)/NPD (40nm)/ 16% Pt2O2: CBP (25nm)/BAlq (10nm)/Alq (30nm)/ LiF/Al can be used, where CBP is 4,4'-bis(N-carbazolyl) biphenyl, BAlq is bis(2-methyl-8-quinolinolato) (biphenyl-4-olato)aluminum and Alq is tris-(8-hydroxyquinoline) aluminum.[110] The resulting external quantum efficiency shown in Figure 42a is reduced to 12.5% due to the lack of state of the art blocking or transport materials resulting in charge imbalance or poor charge and exciton confinement. Furthermore, the large roll-off in the efficiency is attributed to the charge imbalance between the transport of the electrons and holes as the materials and device structure was selected to optimized stability rather than electrical properties. Nevertheless, such an efficiency is much higher that most previous reports employing a similar device structure.The EL spectra (Figure 42 a inset) shows similar emission to that observed in the efficient device structure except with the addition of a small peak between 400-500 nm indicating poor exciton confinement. Remarkably, this small deep blue peak complimented the warm white Pt2O2 color to yield a CRI of 80 and CIE of (0.46,0.47). Accelerated lifetime testing was preformed on the device by driving it at a constant current of 20mA/cm$^2$ corresponding to an initial luminance of 2520 cd/m$^2$. The device demonstrated a lifetime to 80% of initial luminance (LT80) of 43 h at these elevated conditions. This corresponds to 207 h at 1000cd/m$^2$ or over 10,000 h at 100cd/m$^2$ using the conversion equation $LT(L_1)=LT(L_0)*(L_0/L_1)^{1.7}$ where $L_0$ is the measured luminance and $L_1$ is the desired luminance.[111] Further application of state of the art stable host, charge and exciton blocker, and charge transport materials may yeild even greater lifetimes.[112,113] The

acheivement of stable and efficient Pt2O2 doped white devices with peak EQE of 12.5%, CRI of 80 and LT80 of over 200 h at 1000cd/m$^2$ is greater than that previously acheived for Pt7O7 and represents a significant step towards the possible commercializaiton of single doped OLED for solid state lighting.[106]

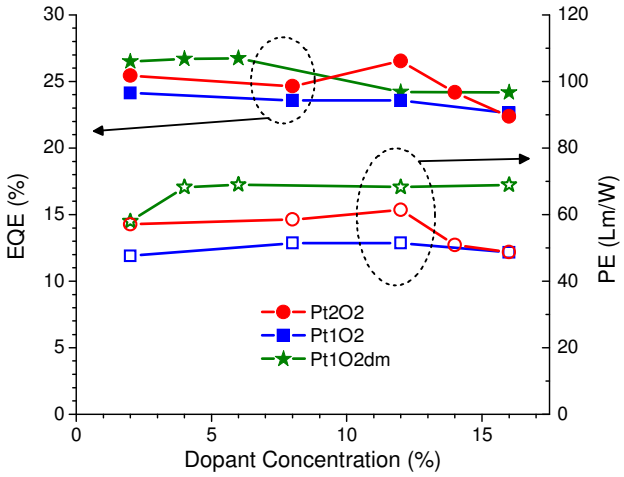


Figure 43 Plots of peak EQE (solid symbols) and peak power efficiency (open symbols) vs emitter concentration for Pt1O2, Pt2O2, and Pt1O2dm based devices with a general structure of ITO/HATCN (10nm)/NPD (40nm)/TAPC (10nm)/x% Dopant: 26mCPy (25nm)/DPPS (10nm)/BmPyPB (40nm)/LiF (1nm)/ Al

Devices with various concentrations of Pt1O2 and Pt1O2me$_2$ where fabricated in the structure: ITO/HATCN(10 nm)/NPD(40 nm)/TAPC(10 nm)/x% emitter: 26mCPy(25 nm)/DPPS(10 nm)/BmPyPB(40 nm)/LiF/Al. As shown in Figure 43 and Table 5, both Pt1O2 and Pt1O2dme are also very efficient across all tested concentrations. The peak external quantum efficiency ranged from 22.6% to 24.1% for Pt1O2 and 24.2% to 26.7% for Pt1O2dme while the power efficiency ranged from 47.6 to 51.4 Lm/W and 58.0 to

69.0 Lm/W respectively. These results further demonstrate the high efficiencies of both the monomer and excimer species characteristic for this class of emitters.

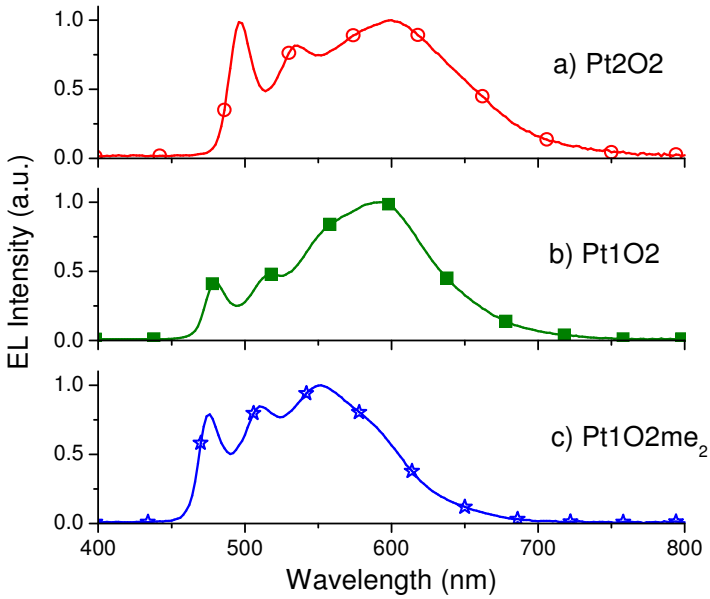


Figure 44 The EL spectra for white devices of a) 14% Pt2O2, b) 12% Pt1O2, and c) 6% $Pt1O2me_2$ in the structure: ITO/HATCN (10nm)/NPD (40nm)/TAPC (10nm)/x% Dopant: 26mCPy (25nm)/DPPS (10nm)/BmPyPB (40nm)/LiF (1nm)/ Al.

The emission spectra for white devise of Pt2O2, Pt1O2, and $Pt1O2me_2$ are shown in Figure 44 for concentrations of 14%, 12%, and 6% respectively. In accordance with the difference in the PL spectra, the monomer emission peak of both Pt1O2 (480nm) and $Pt1O2me_2$ (476nm) is blue shifted relative to Pt2O2 (496nm). The excimer emission peak on the other hand, is only slightly blue shifted for Pt1O2 (592 nm) compared to Pt2O2 (600 nm) although it is more narrow. This similarity in excimer emission is as expected due to the similarity in shape and planarity of the two molecules.[114] The excimer emission of $Pt1O2me_2$, on the other hand, was significantly blue shifted to 556 nm. This

shift may be related to distortion of the molecule due to the methyl group on the 5 position of the pyrazole which can modify the stacking orientation or increase the intermolecular spacing between the two dopant molecules. It is interesting however, that Pt1O2me$_2$ is capable of exhibiting such strong excimer character despite this potential geometric distortion, with nearly dominant excimer character at a Pt1O2dme concentration of only 8%. More synthetic and characterization efforts are needed to elucidate the relationship between the molecular structure, the excimer emission energy, and the concentration dependence. Thus, the choice of cyclometalating ligand needs to be carefully selected to control the influence on the energy of the monomer species as well as control the effect of steric groups on the geometry and stacking of the complexes.

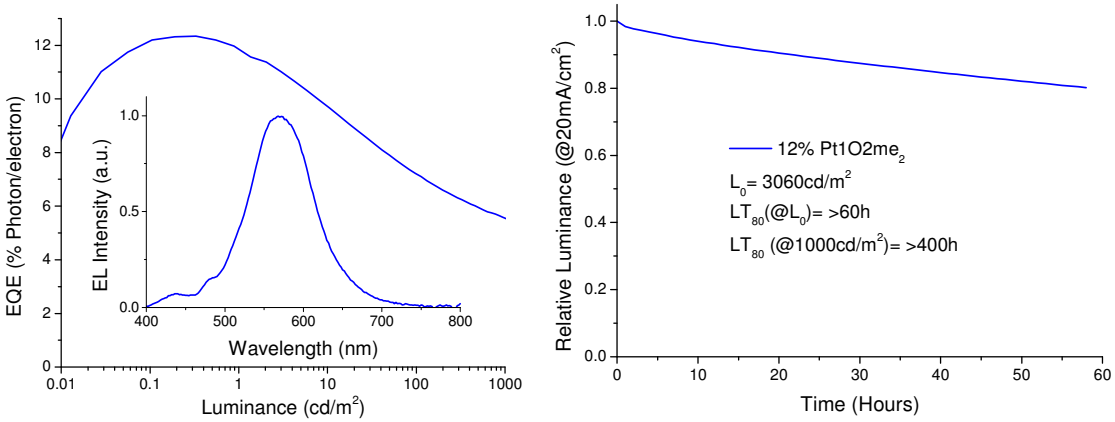


Figure 45 Plots of (a) EQE vs. luminance and EL spectrum at 1mA/cm$^2$ (inset) and (b) luminance intensity versus time at a constant driving current of 20mA/cm$^2$ and LT$_{80}$ values are given in the inset for the device of ITO/HATCN (10nm)/NPD (40nm)/ 12% Pt1O2me$_2$: CBP (25nm)/BAlq (10nm)/Alq (30nm)/LiF (1nm)/ Al.

An additional consequence of the efficient excimer emission at low concentrations for Pt1O2dme is the opportunity to explore the stability of the isolated excimer emissive species in a device setting. Device operational lifetime measurements were carried out for devices of the structure: ITO/HATCN (10nm)/NPD (40nm)/ 12% Pt1O2me$_2$: CBP (25

nm)/BAlq (10 nm)/Alq (30 nm)/ LiF/Al. These devices exhibited nearly exclusive excimer emission which peaked at 567nm yielding an orange color with CIE coordinates of (0.43, 0.50) as shown in Figure 45 (a). The devices were also moderately efficient with a peak EQE of 12.3%, which is similar to that achieved with Pt2O2 in the stable device structure. For operational lifetime testing, devices were driven at a constant current of 20mA/cm$^2$ which corresponds to an initial luminance of 3060 cd/m$^2$. The device demonstrated an LT80 over 60h. which corresponds to over 400h. at 1000cd/m$^2$, which is amongst the highest for any Pt emitters. This long lifetime demonstrates that the excimer species can be very stable and should serve as a benchmark for future excimer based devices.

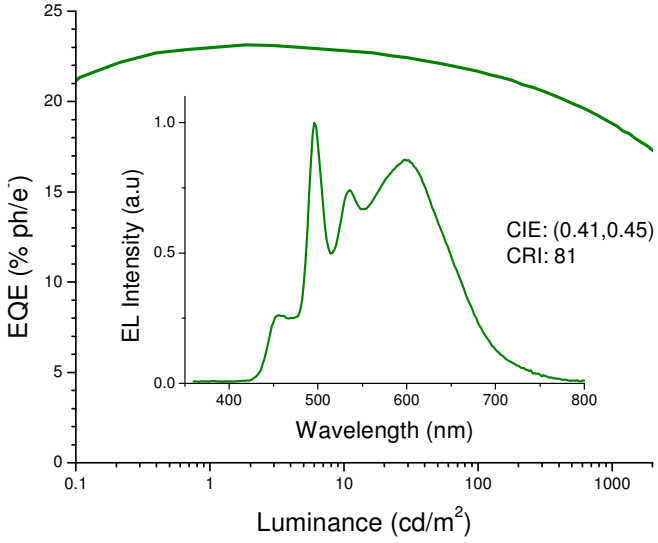


Figure 46 EQE vs. Luminance and EL spectra at 1mA/cm$^2$ (inset) for the multiple emissive layer white device in the structure: ITO/HATCN (10nm)/NPD (40nm)/TAPC (10nm)/16% Pt2O2:26mCPy (10nm)/6% PtON1:26mCPy (15nm)/DPPS (10nm)/BmPyPB(40)/LiF/Al.

Due to the limited spectral coverage in the blue region, these Pt complexes can used as emitters in white devices employing multiple emissive layers to achieve a high efficiency and a high quality of white light. Due to the broad spectral coverage of the monomer and excimer emission, efficient OLEDs with emission covering most of the visible spectrum can be acheived using only 2 emissive materials. This is greatly desired compared to white OLEDs containing 3 or more emissive layers since the optimiztion of charge transport and energy transfer processes in white OLEDs becomes increasingly complex with additional layers.[115] Multilayer white OLEDs containing Pt2O2 and the previously reported deep blue emitter, PtON1, are fabricated in the structure ITO/HATCN(10 nm)/NPD(40 nm)/TAPC(10 nm)/ 16% Pt2O2: 26mCPy (10nm)/6% PtON1: 26mCPy/DPPS(10 nm)/BmPyPB(40 nm)/LiF/Al (15nm).[31] The external quantum efficiency, shown in Figure 46, peaked at 23.1% and the power efficiency peaked at 49.7 Lm/W. The device had low roll-off at high current densities remaining at 18.8% EQE and 24.2 Lm/W at 1000cd/$m^2$. The emission spectrum showed a moderate deep blue contribution from PtON1 which dramatically improved the CRI to 81 and the CIE coordinates to (0.41,0.45). Further optimization and color balance of such devices is likely to yeild much greater performance but this demonstration underlines the importance of incoprorating the deep blue portion of the emission spectrum.

### 3.3.3 Efficient and Stable Single-Doped White OLEDs Using a Palladium-Based Excimer Emitter

Pd(II) complexes also have the potential for efficient excimer based white emission due to their square planar geometry.[116-118] However, Pd(II) complexes have received significantly less attention than their Ir and Pt analogs. This is partially because Pd complexes have typically been non emissive or weakly emissive due to their low radiative decay rates and low lying MC states providing non-radiative decay pathways.[119,120] Furthermore, none of the previous reports of Pd emitters, to our knowledge, have demonstrated efficient excimer emission. In this report, we develop an efficient excimer emitting Pd(II) complex, Pd3O3 which utilizes a rigid and planar molecular design to acheive efficient blue and white emission while remianing aligned with stable molecular designs. This complex demonstrated efficiencies comparable to its Pt analogs but with higher emission energy and high operational stability. Efficiencies as high as 24.2% were achieved for Pd3O3 devices and one device achieved a peak EQE of 19.9% and a device operational lifetime of nearly 1000hrs at 1000cd/$m^2$. This performance establishes Pd complexes as an emerging class of emissive materials and demonstrates their potential for stable, efficient, and simplified white OLEDs.

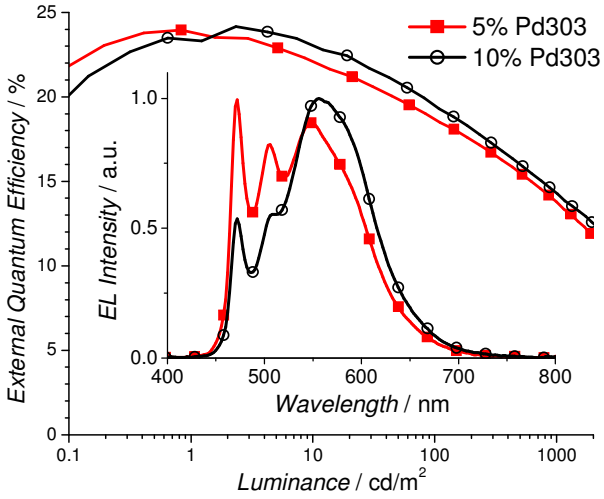


Figure 47 External quantum efficiency versus luminance and electroluminescent spectra for Pd3O3 device with 5% (squares) and 10% (circles) dopant concentrations in the structure: ITO/HATCN/NPD/TAPC/x% Pd3O3:26mCPy/DPPS/BmPyPB/LiF/Al.

The emission spectra in the inset to Figure 47 shows a monomer emission peak at 472nm and a broad excimer peak at 550-600nm. At the dopant concentration of 5%, the excimer peak and monomer peak are approximately equal heights yielding warm white light with CIE coordinates of (0.34, 0.47) and CRI of 53. When the concentration of Pd3O3 is increased to 10% the excimer emission broadens and increases to approximately twice the height of the monomer emission. Consequently, the emission is orange with CIE coordinates of (0.39, 0.50) and a CRI of 52. It should also be noted that the monomer to excimer emission balance occurs at a much lower dopant concentration than many of the reported platinum complexes, yielding an emission spectrum with non-ideal CIE coordinates.[121,122] This is due to the preferential stacking of Pd3O3 molecules which was also reflected in the poor solubility of Pd3O3.[34,99] Furthermore, the excimer emission drops off rapidly at 600 nm missing a significant portion of the red spectrum leading in part to the low CRI. Modifying the planar geometry nature of Pd3O3 molecules by adding steric substitutional groups or using bulky bridging ligands will

allow stronger molecular interaction between emissive materials and the host molecules and can tune the monomer and excimer emission colors to yield more ideal white color.[114,123]

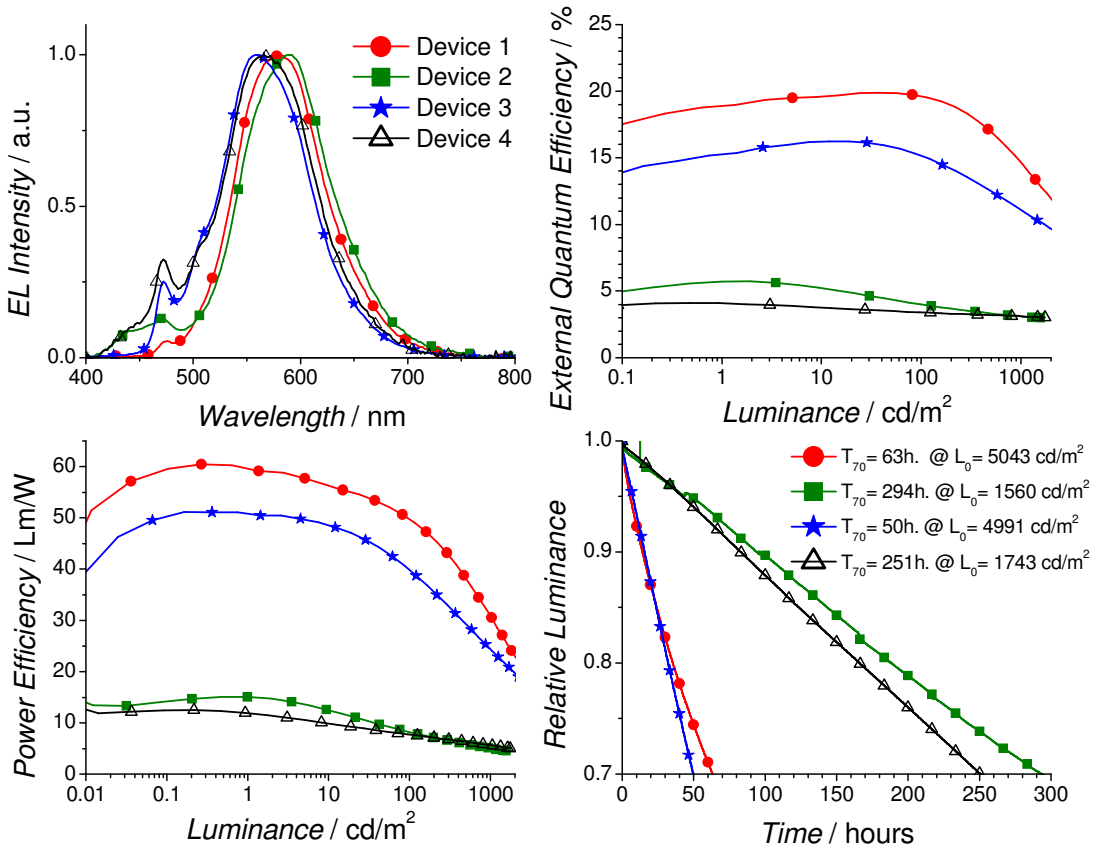


Figure 48 (a) Electroluminescent spectra, (b) external quantum efficiency versus luminance, (c) power efficiency versus luminance and d) electroluminescent intensity versus operational lifetime for Pd3O3 in Device 1 (circles), Device 2 (squares), Device 3 (stars), and Device 4 (triangles). The device operational lifetime was measured at a constant drive current of 20mA/cm$^2$

Currently, there are very few reports on the operational lifetime of white OLED devices and even less is known about the operational stability of excimer based WOLEDs. Due to the known instability of the TAPC and DPPS blocking materials, separate Pd3O3 devices were fabricated in four different stable device structures:

Device 1: ITO/HATCN/ NPD/TrisPCz /10% Pd3O3:mCBP/BAlq/BPyTP/LiF/Al

Device 2: ITO/HATCN/ NPD/10% Pd3O3:mCBP/BAlq/BPyTP/LiF/Al

Device 3: ITO/HATCN/ NPD/TrisPCz /10% Pd3O3:26mCPy/BAlq/BPyTP/LiF/Al

Device 4: ITO/HATCN/ NPD/10% Pd3O3:26mCBP/BAlq/BPyTP/LiF/Al

Where TrisPCz is 9,9′,9″-triphenyl-9H,9′H,9″H-3,3′:6′3″-tercarbazole, mCBP is 3,3-di(9*H*-carbazol-9-yl)biphenyl, BAlq is bis(2-methyl-8-quinolinolato)(biphenyl-4-olato)aluminum, and BPyTP is 2,7-di(2,2′-bipyridin-5-yl)triphenylene, which are selected based on the previous literature reports related to stable fluorescent and phosphorescent devices.[124] The devices were fabricated with a fixed dopant concentration of 10% in order to study the stability of OLEDs with emission originating primarily from the Pd3O3 emitters. As seen in Figure 48 (a), the resulting spectra are dominated by the broad excimer emission, highlighting the importance of reducing excimer formation at a moderate dopant concentration to achieve a balanced spectrum. Devices which had no TrisPCz blocking layer (Device 2 and 4) had significant emission in the 400-450nm range indicating a partial NPD emission due to possible electron leakage or exciton energy transfer to the hole-transporting NPD layer. Consequently, the EQE of the devices without TrisPCz have low peaks EQEs in the range of 4-6%. On other hand, the devices with TrisPCz were very efficient reaching peak EQEs and power efficiencies of 19.9% and 60.5 lm/W for Device 1 and 16.2% and 51.2 lm/W for Device 3. The roll-off for these devices were also less significant than for the previous efficient structures with EQE values of 14.6% and 11.1% at 1000cd/m$^2$ for the Device 1 and Device 3, respectively.

The device operational lifetimes of all 4 stable devices were measured at accelerated conditions by driving the devices at a constant current of 20mA/cm$^2$. Devices

without TrisPCz demonstrated a very long operational lifetime to 70% of initial luminance ($LT_{70}$) of 294 h. at an initial luminance of 1560 cd/$m^2$ for Device 2 and 251 h. at an initial luminance of 1743 cd/$m^2$ for Device 4. When TrisPCz was used, the device operational lifetimes dropped as has been reported previously for devices using a TrisPCz blocking layer due to possible charge built-up at the interface of EML/EBL.Nevertheless, moderately high operational lifetimes were achieved; 63h. (@ 5043cd/$m^2$) for Device 1 and 50h. (@ 4991cd/$m^2$) for Device 3. Furthermore, approximating these accelerated testing results at practical luminance of 1000cd/$m^2$ yields lifetimes of 986 h. for Device 1 and 769 h. for Device 3 respectively. These high lifetimes (close to 1000 h.) and high power efficiency (close to 30 lm/W without any outcoupling enhancement) at practical luminance, approaches the minimum commercialization requirement with appropriate lamination quality. Furthermore, with incorporation of light outcoupling techniques, doubling the luminance at a given driving condition could be reasonably expected to yield lifetimes in the range of 2500-3500h. at 1000cd/$m^2$. Our progress represents a substantial improvement upon previous reports of Pt-based excimers which demonstrated less than 100h. for Pt7O7 or 400h. for Pt1O2$me_2$ at 1000cd/$m^2$ both of which were only in the range of 8-12% efficient

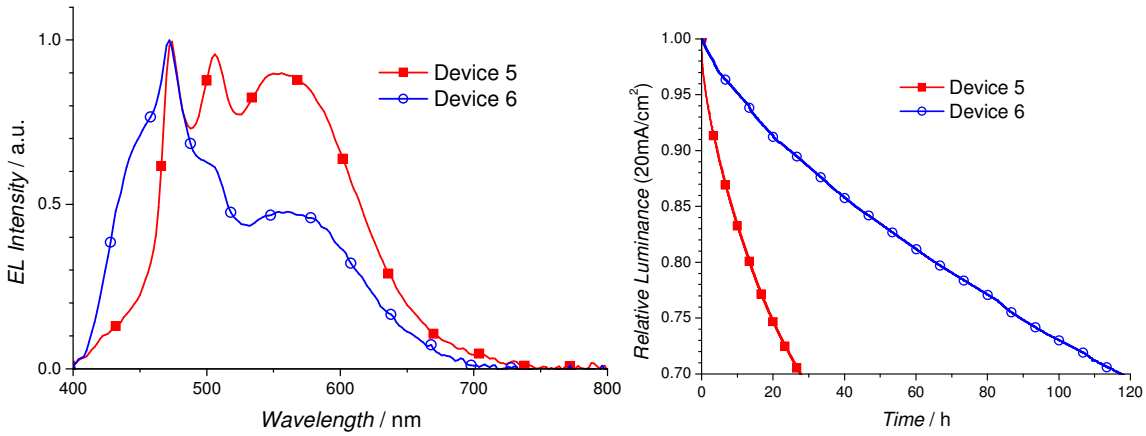


Figure 49. (a) Electroluminescent spectra, and ( b) operational lifetime for Pd3O3 in Device 5 (squares) and Device 6 (circles). The device operational lifetime was measured at a constant drive current of 20mA/cm$^2$

Despite the strides made to improve efficiencies and operational lifetimes, the color quality of the stable devices was poor due to the ease of aggregation of Pd3O3 molecules. Thus, devices were made which attempt to balance the monomer and excimer emission in the structure:

Device 5: ITO/HATCN/ NPD/TrisPCz/2% Pd3O3:mCBP/BAlq/BPyTP/LiF/Al

Device 6: ITO/HATCN/ NPD/2% Pd3O3:mCBP/BAlq/BPyTP/LiF/Al

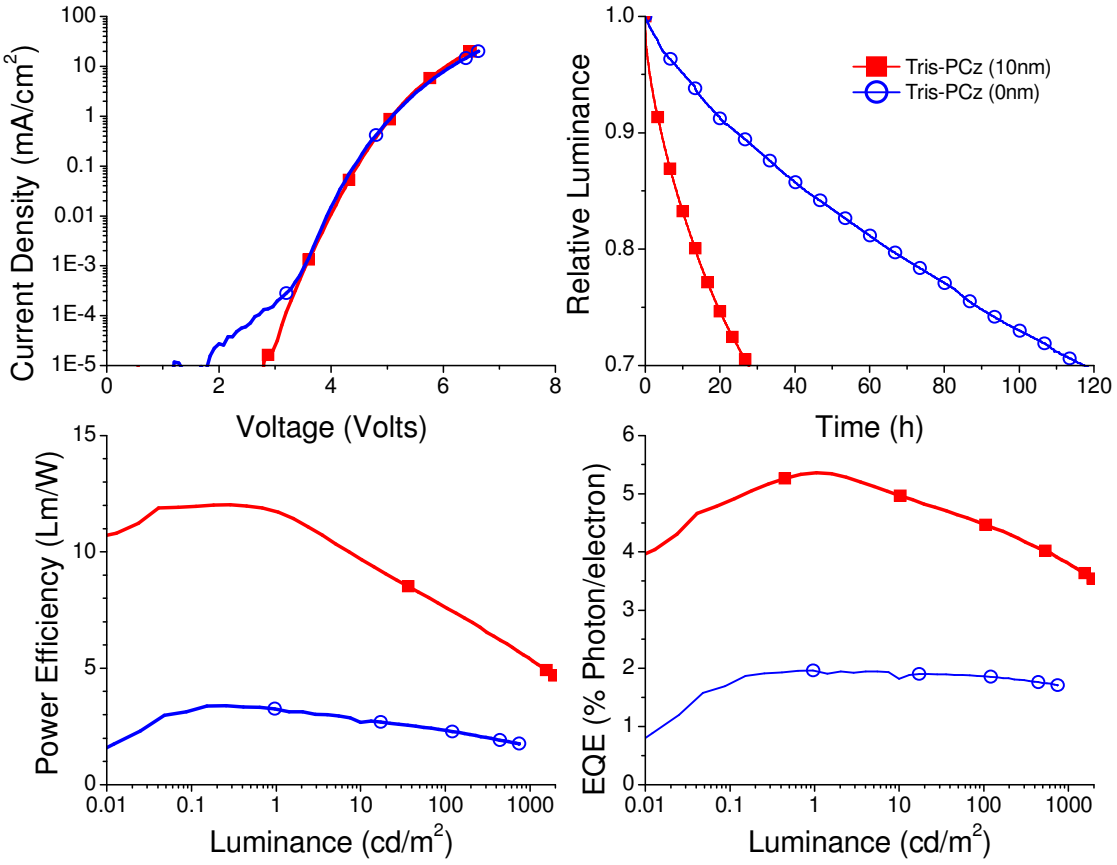


Figure 50 (a) Current density-voltage characteristics, (b)operational lifetime , (c) power efficiency vs. luminance, and d) external quantum efficiency vs. luminanceof Pd3O3 devices in the structure: ITO/HATCN(10 nm)/ NPD(40 nm)/TrisPCz (0 or 10nm)/2% Pd3O3:mCBP(25 nm)/BAlq(10 nm)/BPyTP(40 nm)/LiF/Al with no TrisPCz (circles) and 10nm TrisPCz (squares).

Where mCBP was selected as a host for both higher efficiencies and longer operational lifetimes. Excimers were found to form more readily in mCBP than mCPy, possibly due to solid solubility effect as has been reported previously, and a low concentration of 2% was needed to balance the emission. The resulting emission spectra are given in Figure 49 (a). Device 5, with a TrisPCz blocking layer, showed a nearly balanced emission spectrum resulting in color coordinates of (0.33, 0.44) and a CRI of 63. There is also emission in the 400-450nm range that was not present in the 10% doped devices indicating some leakage processes in this device. Consequently, a peak efficiency of only

5.4% was achieved (Figure 50). For Device 6, which has no TrisPCz blocker, the emission between 400-450 increases substantially due to energy transfer into the NPD layer, dropping the peak efficiency down to only 1.8%. However, the additional blue emission did improve the CRI to 80 and CIE coordinates of (0.27, 0.30).

The device operational lifetime at accelerated testing conditions of 20mA/cm2 were also collected for these 2% doped devices. The resulting LT70 were 28h. for Device 5 and 117h. for Device 6; nearly a third on those with a 10% dopant concentration. Approximated lifetimes at 1000 cd/m2 are only 86 h and 70 h. for Devices 5 and 6, respectively. These results reflect the challenge in balancing color, efficiency, and operational stability when molecular aggregation is too favorable and the optimal emission color of white OLED is realized at a low dopant concentration [125] Thus, the modification of Pd3O3 molecular geometry to improve the solubility of this complex in the host matrix is necessary and research efforts toward this goal are currently underway.

Table 6 Summary of device performance for Pd3O3 based devices.

| Device | CRI | CIE | EQE (%) | | PE (lm/W) | | $L_0$ ($cd/m^2$) | $LT_{70}$ | |
|---|---|---|---|---|---|---|---|---|---|
| | | | peak | 1000cd/$m^2$ | peak | 1000cd/$m^2$ | | @$L_0$ | @1000cd/$m^2$ |
| 1 | 48 | (0.48,0.50) | 19.9 | 14.6 | 60.5 | 30.8 | 5043 | 63 | 986 |
| 2 | 57 | (0.47,0.46) | 5.7 | 3.1 | 15.1 | 5 | 1560 | 294 | 626 |
| 3 | 48 | (0.42,0.52) | 16.2 | 11.1 | 51.2 | 24.5 | 4991 | 50 | 769 |
| 4 | 56 | (0.41,0.48) | 4.1 | 3.1 | 12.5 | 5.7 | 1743 | 251 | 645 |
| 5 | 63 | (0.33,0.44) | 5.4 | 3.8 | 12 | 5.4 | 1930 | 28 | 86 |
| 6 | 80 | (0.27,0.30) | 1.9 | -- | 3.4 | -- | 740 | 117 | 70 |

### 3.3.4 Red, Green, and Blue Tetradentate Platinum Phosphorescent Emitters for Efficient White OLEDs

There is a wide range of approaches to achieve high color quality with white organic light emitting diodes. These include multiple emissive materials within a device, striped regions of red, green, and blue emission, combination of fluorescent and

phosphorescent emission, or the combination of monomer and excimer emission from square planar metal complexes.[127-130, 89,] Of these various options, the combination of three emissive dopants has typically been favored due to the ability to obtain a broad spectrum of high-quality white light by controlling the relative contribution of each emissive material to optimize CIE coordinates and CRI value. In particular, the use of multiple emissive layers (EMLs) to separate the red, green and blue emissive dopants has seen success in minimizing interaction between emitters to achieve balanced color quality and high efficiencies.[94,131] However, the efficiency, color quality, and stability of these devices are still far from commercial application.[94, 132-135] Therefore more improvements must be made in both materials design and device architectures, especially through the development of new emissive materials.

To date, much of the research into emissive materials has focused on iridium-based complexes, for which external quantum efficiencies (EQE) of 25% and higher have been reported for emission ranging across the whole visible spectrum. Iridium complexes also tend to have a shorter radiative decay time, which makes it easier to achieve higher efficiency with low roll-off. Platinum complexes, on the other hand, have received significantly less attention for WOLED applications, despite recent reports of performance and color purity equivalent or superior to their iridium analogs.[112, 136] The square planar ligand coordination of Pt complexes also allows the design of rigid tetradentate metal complexes, which shortens radiative decay process and increases the photoluminescence quantum efficiency. Thus, due to their potential for high performance and desirable color quality, platinum complexes for WOLEDs should be vigorously investigated as alternative emissive materials for the lighting applications. In this report,

the development of WOLEDs utilizing red, green, and blue Pt-based phosphorescent emitters is described. Furthermore, the charge transport and energy transfer processes for WOLEDs employing multiple platinum-based emitters are studied. Ultimately, a WOLED with the CRI value of 80, CIE coordinates of (0.35, 0.35), maximum external quantum efficiency (EQE) of 21.0%, and maximum power efficiency (PE) of 41 lm/W is obtained. Such a performance is comparable to the state-of-the-art of WOLEDs employing multiple Ir-based phosphorescent emitters.[117, 138] To the best of author's knowledge, this work is the first report of multiple Pt-based emitting layer WOLED that demonstrates the peak EQE of 21.0%.

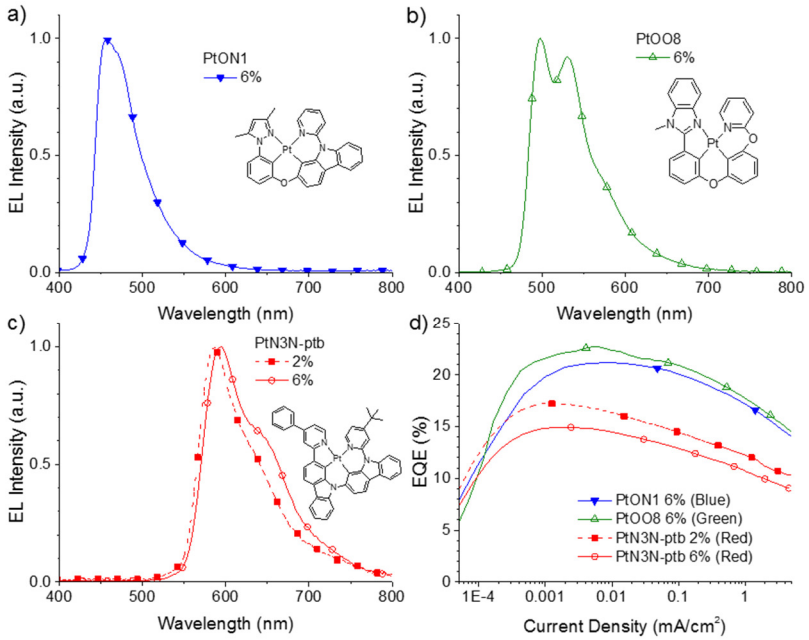


Figure 51. (a)-(c) EL spectra and d) plots of EQE vs. current density of OLEDs with a device structure of ITO/ HATCN/ NPD/ TAPC/ emitter: 26mCPy(25nm)/ DPPS/ BmPyPB/ LiF/ Al. The emitters used are a) PtON1 (blue), b) PtOO8 (green), and c) PtN3N-ptb (red). Inset figures are molecular structures of emitters used. The corresponding molecular structures of each emitter are presented in the inset of Figures.

Monochromatic devices using each individual emitter are fabricated in a general structure of ITO/ HATCN/ NPD/ TAPC/ 26mCPy: x% emitter (25nm)/ DPPS/ BmPyPB/ LiF/ Al. The plots of electroluminescence (EL) spectra as a function of wavelength, plots of EQE vs. current density, and the corresponding molecular structures of each emitter are shown in Figure 51. Peak external quantum efficiency (EQE) values of 17%, 23%, and 21% are achieved for 2% PtN3N-ptb, 6% PtOO8, and 6% PtON1 doped devices respectively. The device with 6% PtON1 doping concentration exhibits a deep blue emission spectrum, which covers much of the blue region necessary to achieve high CRI value. The device employing 6 % PtOO8 doping concentration shows an emission peak at 498 nm and a secondary emission peak at 530 nm to provide an appropriate green color. The emission spectra of the 2% PtN3N-ptb doped device peaks at 588 nm but

drops off sharply, missing a significant portion of the red spectrum beyond 650nm. Upon increasing the dopant concentration of PtN3N-ptb from 2% to 6%, its spectrum is broadened and red-shifted to a peak wavelength of 593 nm, due to a rise in the vibronic emission sideband. This vibronic emission is desirable to include more of the red spectrum for a high-quality white light. A linear combination of the emission intensities of the three emitters suggests that the use of 2% PtN3N-ptb emissive layer would lead to a maximum possible CRI value of 79, while the use of 6% PtN3N-ptb emissive layer would lead to a maximum possible CRI value of 82, neglecting interactions between the emitters or optical interference effects.[139,140] However, the increase in the dopant concentration of PtN3N-ptb based red OLED decreases the peak EQE to 15%. Thus, the PtN3N-ptb concentration poses a trade-off between optimizing the device efficiency and the color quality.

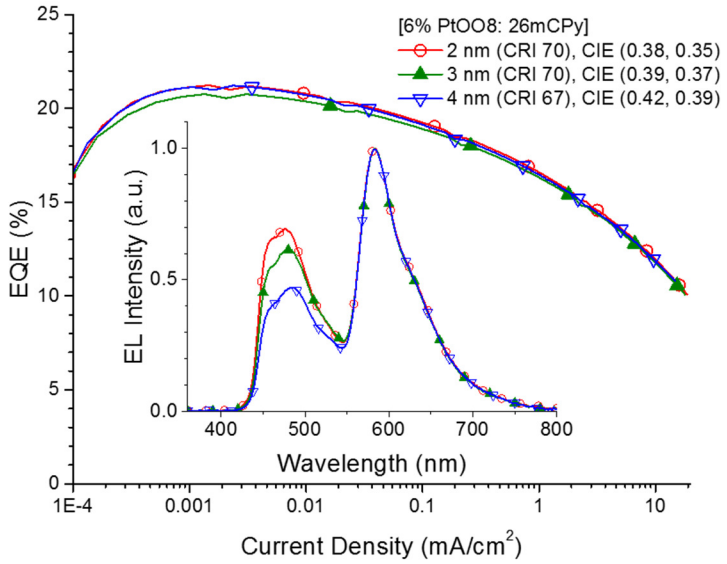


Figure 52. EL spectra (inset) and the plots of EQE vs. current density of WOLEDs with a device structure of ITO/ HATCN/ NPD/ TAPC/ 6% PtON1: 26mCPy (20nm)/ 6% PtOO8: 26mCPy (x nm)/ 2% PtN3N-ptb: 26mCPy (3 nm)/ DPPS/ BmPyPB/ LiF/ Al. The thickness of 6% PtOO8: 26mCPy layer was varied in the range of 2 – 4 nm. The EL spectra are normalized to the PtN3N-ptb emission peak.

WOLEDs are fabricated with three emissive layers in the stacking order of 6% PtON1:26mCPy/ 6% PtOO8:26mCPy/ 2% PtN3N-ptb:26mCPy, termed Structure I: ITO/ HATCN/ NPD/ TAPC/ 6% PtON1: 26mCPy (20nm)/ 6% PtOO8: 26mCPy (**x**)/ 2% PtN3N-ptb: 26mCPy (3nm)/ DPPS/ BmPyPB/ LiF/ Al, where x is 2, 3, 4 nm. In Structure I, a thin (3nm), lightly doped (2%) PtN3N-ptb layer is deposited nearest to the DPPS interface, while a 6% PtOO8 doped layer is inserted between PtON1 and PtN3N-ptb doped layers to add the green portion of the visible spectrum. In order to examine the effect of the PtOO8 layer on the device performance, the thickness of 6% PtOO8 layer is varied from 2 nm to 4 nm, while the thicknesses of PtON1 and PtN3N-ptb doped layers are fixed to 20nm and 3nm, respectively. The resulting EL spectra and EQE vs. current density curves are given in Figure 52. The EQE and PE of the devices show minimal variation with increasing the thickness of the 6% PtOO8 doped layer with peak EQE

ranging from 20.8% to 21.2%, and peak PE of 43 to 45 lm/W. Despite the high overall efficiencies, there is a minimal PtOO8 contribution to the emission spectrum, resulting an unsatisfactory CRI value of 70. The low contribution of PtOO8 layer is likely due to a high rate of energy transfer from PtOO8 complex ($E_T$ = 2.5 eV) to nearby PtN3N-ptb complex ($E_T$ = 2.1 eV).[132] Moreover, as the thickness of the PtOO8 layer increases from 2nm to 4 nm, the blue emission of PtON1 complex decreases, and then results in the change of the CIE coordinates from (0.38, 0.35) to (0.42, 0.39) and the decrease of CRI value from 70 to 67, respectively. The decrease in the PtON1 emission can be explained regarding the depth of a recombination zone. When a recombination zone is formed at an interface between an emissive layer and a charge blocking layer, typically, the depth of a recombination zone is known to be less than 10 nm. Thus, when the recombination zone is formed at the interface between the PtN3N-ptb emissive layer and the hole blocking layer of DPPS, with increasing the thickness of PtOO8 layer, the PtON1 layer is pushed away from the recombination zone, in turn, results in the decreased emission of PtON1 complex.

Conclution

A series of tetradentate platinum complexes and palladium complexes are synthesized and used for single doped white OLED applications and RGB white OLED applications. Devices employing all of the developed platinum based emitters demonstrated impressively high external quantum efficiencies within the range of 22%-27% for all concentrations between 2% and 16%. And the palladium complexes Pd3O3 devices fabricated in a stable device structures achieved nearly 1000h. at 1000cd/m2 without any outcoupling enhancement while simultaneously achieving peak external quantum

efficiencies of 19.9% and power efficiencies over 60 lm/W. The RGB OLED device employing all platinum based complaex emitters with 6% PtN3N-ptb(red)/6% PtON1(blue)/6% PtOO8(green) stacking order of emissive layers demonstrates CIE coordinates of (0.35, 0.35) and CRI value of 80, peak Power Efficiency (PE) of 41 lm/W, and maximum External Quantum Efficiency (EQE) of 21.0%.

# CHAPTER 4

# TETRADENTATE PLATINUM AND PALLADIUM COMPLEXES FOR STABLE AND EFFICIENT BLUE OLEDS

## 4.1 Introduction

Phosphorescent metal complexes are under heavy investigation as emitters for energy efficient and cost effective display and solid state lighting applications.[136, 141-143] Their success stems from their ability to harvest 100% of electrogenerated singlet and triplet excitons.[144] Through diligent emitter and device design, efficient organic light emitting diodes (OLEDs) emitting across the visible spectrum have been achieved with electron to photon conversion efficiencies approaching 100%.[145-149] However, the development of efficient blue OLEDs that also have high device operational stability remains a significant challenge.[150] This deficiency is one of the major remaining obstacles for widespread commercialization of energy efficient OLEDs. Thus, overcoming such a hurdle will have an incredible impact on next generation display and white lighting technologies.

The development of blue emitters has primarily focused on the design of Ir complexes with high emission efficiency and deep blue color.[151-153] Recently, rapid progress has also been made in the development of efficient deep blue OLEDs employing Pt complexes,[136,154-156] which, in some cases, have demonstrated superior performance to their Ir analogs with efficiencies as high as 24.8% and CIE coordinates of (0.148, 0.079) as shown for the recently reported emitter PtON7-dtb.[157] In either case, this progress has largely been achieved through the judicious design of high triplet energy cyclometalating ligands following well understood color tuning strategies.

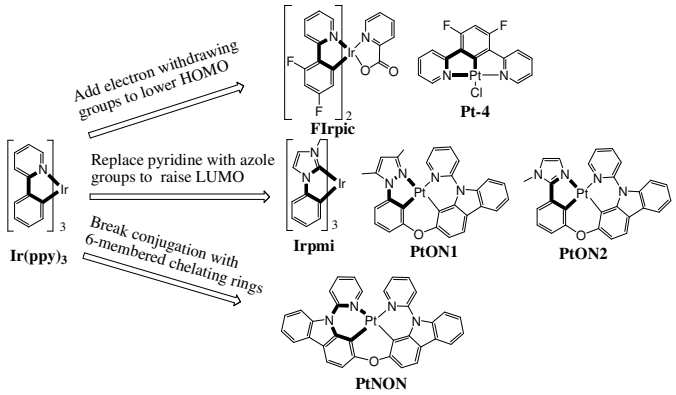


Figure 53. Color tuning strategies for blue emitters. The thick line was used to illustrate both 5-membered and 6-membered metal chelation rings as part of chromophores for phosphorescent metal complexes.

Using the prototypical phoshporescent complex fac-Ir(ppy)$_3$ as a starting point, the green emission color can be sufficiently blue shifted through the modification of the phenyl-pyridine cyclometalating ligand through two complimentary strategies as shown in the top two pathways of Figure 53. Firstly, the emission energy can be blue-shifted by lowering the energy of the highest occupied molecular orbital (HOMO) through adding electron withdrawing groups on the phenyl ring, as is used in the most widely reported blue emitters, such as FIrpic, FIr6, FPt, and Pt4.[158-160] While this strategy successfully shifts the emission while affording high efficiencies, the poor electrochemical stability of fluorine containing emitters results in rapid degradation of blue OLEDs as exemplified by the low operational lifetime for FIrpic.[161] The other current strategy is to raise the energy of the lowest unoccupied molecular orbital (LUMO) by replacing the 6-membered pyridine ring with a 5-membered azole groups such as pyrazole, triazole, methylimidazole, or methylimidazole-carbene as is the case for many of the state of the art efficient deep blue emitting metal complexes.[34, 111, 117] Through this second route, deep blue emission and high efficiencies have been acheived with devices of PtON1

reaching a peak EQE of 25.2% and CIE coordinates of (0.15, 0.13).[92] Nevertheless, the operational stability of these emitters is dramatically less than their phenyl-pyridine analogs. In either case, much is still unknown about the underlying mechanism behind the low operational stabilities of blue phosphorescent emitters with azole based or fluorinated cyclometalating ligands, but, nearly all of the existing studies indicate operational lifetimes that are orders of magnitude lower than their green or red emitting phenyl-pyridine based analogs.[112,162]

In the first part of this chapter, we demonstrate an alternative strategy for deep blue emission by designing a ligand that breaks the conjugation between the donor and acceptor portions of the cyclometalating ligand. This is achieved by replacing the typical 5-membered metal chelation rings with 6-membered rings (Bottom of Scheme 1). 6-membered chelation rings allows high energy emission to be achieved while retaining a design motif that is well aligned with electrochemically stable materials and opens up a new class of emissive materials for blue phosphorescent OLED applications. A Pt complex with carbazolyl-pyridine cyclometalating ligands, PtNON, achieved a peak external quantum efficiency of 24.4 % and CIE coordinates of (0.18, 0.31) in a device structure designed for charge confinement. Furthermore, devices architectures using known stable components with PtNON achieved an operational lifetime of 89 hours to 70% initial luminance at 3145 cd/m$^2$. This corresponds to over 30,000 hours at 100cd/m$^2$ or 600 hours at 1000cd/m$^2$ while also retaining moderate efficiencies over 10%. This is among the highest device operational lifetimes for an emissive Pt complex and is, to the author's knowledge, the first literature report of long lifetimes for blue phosphorescent emitters with high triplet energy (i.e. over 2.8 eV).

Also, from the experience of the Pd complex in chapter 2, which demonstrates its potential for stable, efficient, and simplified white OLED. a new blue emitting palladium complex Pd2O2 will also be discussed in the second part of this chapter.

4.2 Synthesis and Structural Characterization

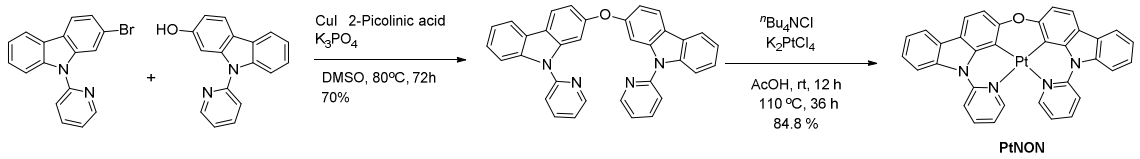


Figure 54 Synthetic route for PtNON

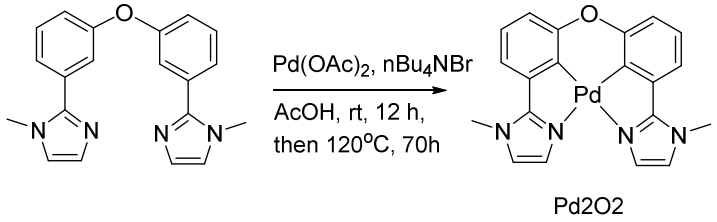


Figure 55 Synthetic route for Pd2O2

9-(pyridin-2-yl)-2-(9-(pyridin-2-yl)-9H-carbazol-2-yloxy)-9H-carbazole :

To a 100 mL three-neck round-bottom flask were added 9-(pyridin-2-yl)-9H-carbazol-2-ol (260 mg, 0.92 mmol), 2-bromo-9-(pyridin-2-yl)-9H-carbazole (356 mg, 1.13 mmol), CuI(17.5 mg, 0.092 mmol), 2-picolinic acid (22.6 mg, 0.183 mmol), and K3PO4(391 mg, 1.83 mmol), the flask was evacuated and backfilled with nitrogen for three times and DMSO (5 mL) was added under the protection of nitrogen, the reaction mixture was stirred at 80 ºC under nitrogen for 72 hours. After cooling to room temperature, the mixture was poured into 100 mL of water and extracted with ethyl acetate (20 mL*3), the combined organic layer was dried with anhydrous Na2SO4 and concentrated under

reduced pressure. Purification by column chromatography (dichloromethane: methanol 20:1) afford the desired product as white solid (322 mg, 70%) 1H NMR (DMSO-d6, 400 MHz): δ 7.06 (dd, J = 8.4 Hz, 2.0 Hz, 2 H), 7.33 (t, J = 7.6 Hz, 2 H), 7.40-7.46(m, 4 H), 7.51(d, J = 1.6 Hz, 2 H), 7.76(d, J = 8 Hz, 4 H), 8.03-8.09 (m, 2 H), 8.18-8.26 (m, 4 H), ), 8.63-8.66 (m, 2 H).

Synthesis of platinum(II) 9-(pyridin-2-yl)-2-(9-(pyridin-2-yl)-9H-carbazol-2-yloxy)-9H-carbazole PtNON: 9-(pyridin-2-yl)-2-(9-(pyridin-2-yl)-9H-carbazol-2-yloxy)-9H-carbazole(240mg, 0.48mmol), K2PtCl4(208mg, 0.50mmol), and n-Bu4NBr(15.4mg, 0.048mmol) were charged into a 100ml three-neck round-bottom flask, then 30ml acetic acid was added. The mixture was bubbled with nitrogen for 30 minutes then stirred at ambient temperature for 12 hours. The mixture was heated in an oil bath at a temperature of 110 $^{o}$C for another 36 hours. 100ml of water was added after the mixture was cooled down to room temperature. The precipitate was collected through filtration, washed with water for three times then dried in air. The collected solid was purified through column chromatography on silica gel using dichloromethane as eluent to afford the desired platinum complex PtNON as a bright yellow solid 280 mg in 85% yield. 1H NMR (DMSO-d6, 400 MHz): δ 7.16 (d, J = 8.0 Hz, 2 H), 7.25-7.30 (m, 2 H), 7.39 (t, J = 7 Hz, 2 H), 7.46(t, J = 7.6, 2H), 7.89 (d, J = 8.0 Hz, 2 H), 8.05(d, J = 8.0 Hz, 2 H), 8.13-8.18(m, 6 H), 9.0(d, J = 5.2 Hz, 2 H). 13C NMR (100 MHz, DMSO-d6, δ): 93.99, 111.8, 114.3, 115.3, 116.0, 116.5, 119.7, 120.4, 122.8, 124.3, 127.7, 137.5, 139.8, 142.3, 147.8, 151.3, 152.0; MS (MALDI-TOF) m/z: [M]+ Calcd for C34H20N4OPt 695.13, Found 695.23.

Anal. calcd for C34H20N4OPt: C, 58.70, H, 2.90, N, 8.05; Found: C 57.98, H 3.05, N 7.88.

Synthesis of 1-methyl-2-(3-(3-(1-methyl-1*H*-imidazol-2-yl)phenoxy)phenyl)-1*H*-imidazole (Pd2O2).

1-methyl-2-(3-(3-(1-methyl-1*H*-imidazol-2-yl)phenoxy)phenyl)-1*H*-imidazole (478 mg, 1.45 mmol), $Pd(OAc)_2$ (348 mg, 1.55 mmol), and n-$Bu_4NBr$(48 mg, 0.149 mmol) were added into a 100ml three-neck round-bottom flask, then 30ml acetic acid was added. The mixture was bubbled with nitrogen for 30 minutes then stirred at ambient temperature for 12 hours. The mixture was heated in an oil bath at a temperature of 110 $^oC$ for another 72 hours. 100 ml of water was added after the mixture was cooled down to room temperature. The precipitate was collected through filtration, washed with water for three times then dried in air. The collected solid was purified through column chromatography on silica gel using dichloromethane as eluent to afford the desired Palladium complex Pd2O2 as a light yellow solid 425 mg in 68% yield. 1H NMR (DMSO-d6, 400 MHz): ):

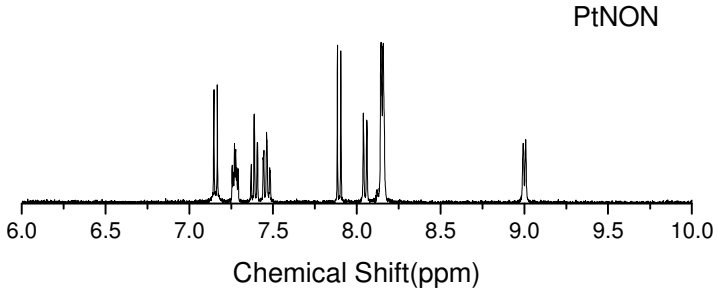


Figure 56 $^1H$ NMR spectra of PtNON (400 MHz, DMSO-d6).

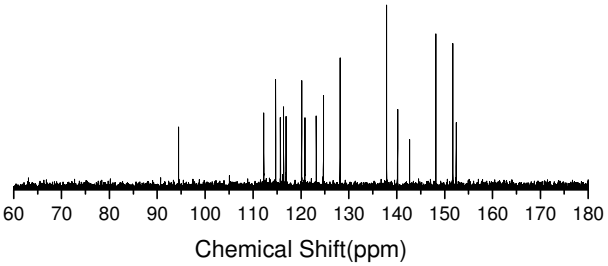


Figure 57: $^{13}C$ NMR spectra of PtNON (100 MHz, DMSO-d6).

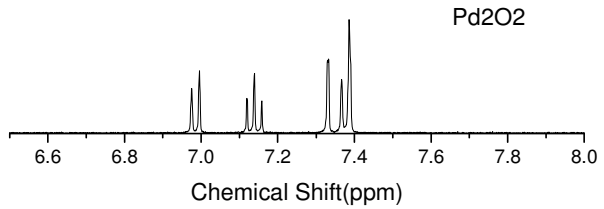


Figure 58 $^{1}H$ NMR spectra of Pd2O2 (400 MHz, DMSO-d6).

4.3 Result and Discussion

4.3.1 Electrochemical Properties

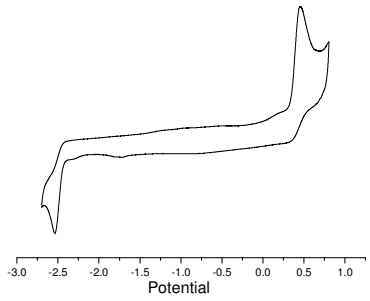


Figure 59 Cyclic voltammetry analysis of PtNON in dimethylformamide with a scan rate of 100 mV/s. Voltages are referenced to the ferrocene/ferrocenium peak

The electrochemical properties of PtNON was examined using cyclic voltammetry (Figure 59) and differential pulsed voltammetry. And PtNON exhibit reversible oxidation processes. The oxidation and reduction potentials are 0.37V and -2.83V vs. Fc/Fc+ respectively for PtNON. Compared with oxidation and reduction potentials of 0.32V and 2.69V for $Ir(ppy)_3$, PtNON has larger band gap becasuse of breaking of the conjugation compared to the green emission of phenyl pyridine based complexes.

### 4.3.2 Photophysical Properties

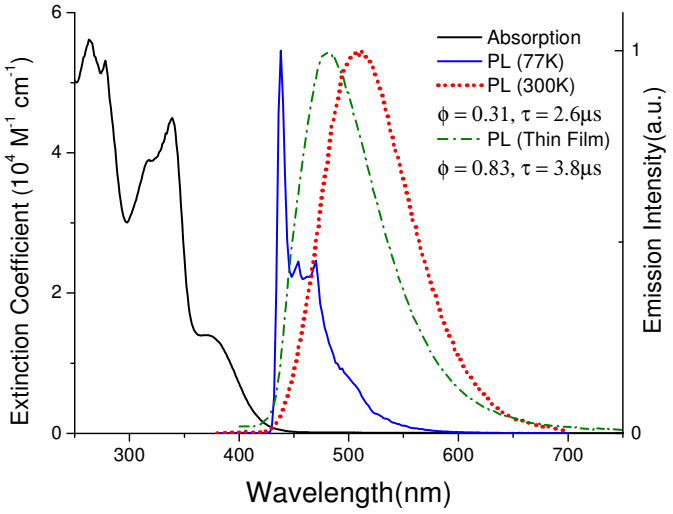


Figure 60 Absorption, emission spectra of PtNON in 2-methyl tetrahyrdofuran at 77K, in a solution of dichloromethane at room temperature and in a doped PMMA thin film at room temperature.

The absorption spectrum shows high intensity bands below 300nm attributed to $^1\pi$-$\pi^*$ transitions on the carbazolyl-pyridine cyclometalating ligands and the bands between 300-420nm are attributed to metal to ligand charge transfer transitions ($^1$MLCT). The strength and shape of the transitions are very similar to those observed for other tetradentate Pt complexes such as PtON1 and PtON7.[109] The emission spectra of PtNON at 77K in 2-methyl tetrahydrofuran, given in Figure 60, shows a deep blue emission peaking at 438nm with small sideband peaks at 454 nm and 470 nm respectively, indicating an estimated triplet energy of 2.83 eV for PtNON molecule. This deep blue emission illustrates the shift achieved by breaking of the conjugation compared to the green emission of phenyl pyridine based complexes. At room temperature in a solution of dichloromethane, the emission spectrum of PtNON is significantly broadened and red-shifted, forming a structureless emission band centered at 508nm. The PLQY of PtNON in DCM is 31% with a luminescent lifetime of 2.6 μs. However, upon casting PtNON in a

5% doped PMMA thin film the PLQY reaches a high value of 83%, and the luminescent lifetime of PtNON remains as short as 3.76μs, making it highly desirable as a phosphorescent emitter for OLED applications. The photoluminescent spectrum from the thin film also shows a broad emission band albeit at a higher energy with a peak of 474nm. The strong MLCT absorption bands and the broad emission at room temperature in solution and thin film both strongly indicate strong $^{1}$MLCT/$^{3}$MLCT characters in the lowest triplet state of PtNON.

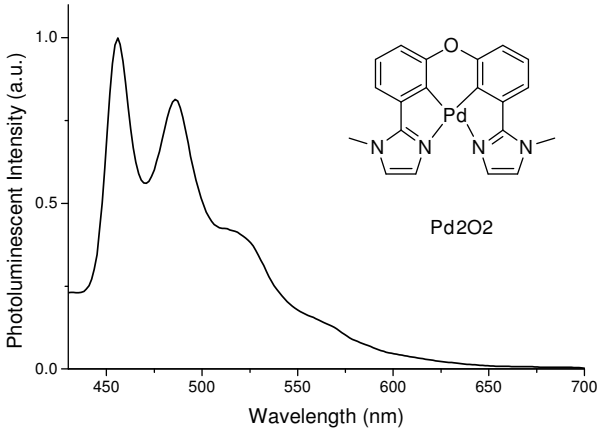


Figure 61 Room temperature emission spectrum of Pd2O2 in a solution of dichloromethane. The molecular structure of Pd2O2 is given in the inset to the plot.

The photoluminescent emission spectrum of Pd2O2 (Figure 61) in a solution of dichloromethane showed a dramatic blue shift of 40nm compared to its platinum analog Pt2O2, which is a potential planar deep blue emitting palladium complex. This blue color could provide a much higher CRI that Pt2O2 in a white device due to its deep blue color.

4.3.3 Tetradentate Pt(II) complexes with 6-membered chelate rings for stable and efficient blue OLEDs

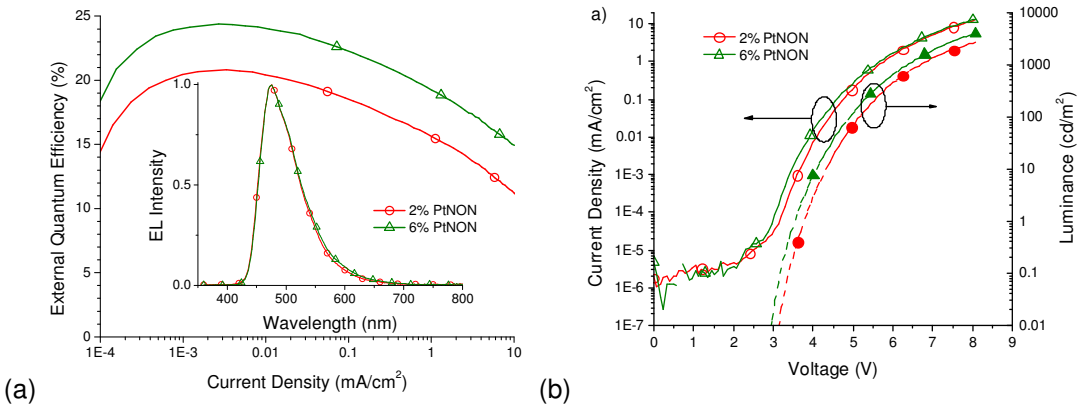


Figure 62 (a) External quantum efficiency versus current density and electroluminescent spectra (inset) and (b) J-V (left) and luminance-V characteristics for PtNON devices with 2% (circles) and 6% (triangles) doping concentrations in the structure: ITO/HATCN/NPD/ TAPC/x% PtNON: 26mCPy/DPPS/BmPyPB/LiF/Al.

To the evaluate the utility of PtNON in a device setting, OLEDs were fabricated in the charge and exciton confining structure: ITO/HATCN (10nm)/NPD (40nm)/TAPC(10 nm)/x% PtNON: 26mCPy (25nm) /DPPS (10nm)/BmPyPB (40nm)/LiF/Al where HATCN is 1,4,5,8,9,11-hexaazatriphenylene-hexacarbonitrile, NPD is N,N'-diphyenyl-N,N'-bis(1-naphthyl)-1,1'-biphenyl-4,4"-diamine, TAPC is di-[4-(N,N-di-toylyl-amino)-phyenyl]cyclohexane, 26mCPy is 2,6-bis(N-carbazolyl) pyridine, DPPS is diphenyl-bis[4-(pyridin-3-yl)phenyl]silane, and BmPyPB is 1,3-bis[3, 5-di(pyridin-3-yl)phenyl]benzene.[164-168] The EQE for PtNON devices with 2% and 6% (w/w) dopant concentrations are given in Figure 62. The external quantum efficiency for the 2% device peaks at 20.8% remaining at 17.2% at 100cd/m$^2$ indicating efficient energy transfer from the host to the dopant molecules despite the high triplet energy of PtNON (over 2.8 eV). The efficiency is improved at higher doping concentrations (6% PtNON:26mCPy) to 24.4 % and retains a high efficiency of 21.2 % at 100 cd/m$^2$. These high efficiencies are comparable to the best reported blue Ir and Pt complexes with 5-membered heterocycles

(such as PtON1) or fluorinated ligands (Such as FIrpic) reported in the literature.[147,149] The emission spectra show broad, structureless emission with an onset at 420 nm and a peak at 476 nm for both devices. This ultimately results in a sky blue emission with CIE coordinates of (0.18, 0.31) and (0.18, 0.32) for the 2% doped and 6% doped devices respectively. The apparent lack of excimer or dimer emission for PtNON is attributed to the non-planar geometry of the complex (Figure 63).[107] Furthermore, it is promising that a substantial portion of the emission falls within the range of 420-470 nm which is helpful for achieving desirable color coordinates for broad white devices. Nevertheless, the broad emission character precludes PtNON from achieving exclusive deep blue emission without optical modification such as microcavity structures. Thus, more work is needed to narrow and blue-shift the peak emission of the emitter to resemble the 77K spectrum more closely.

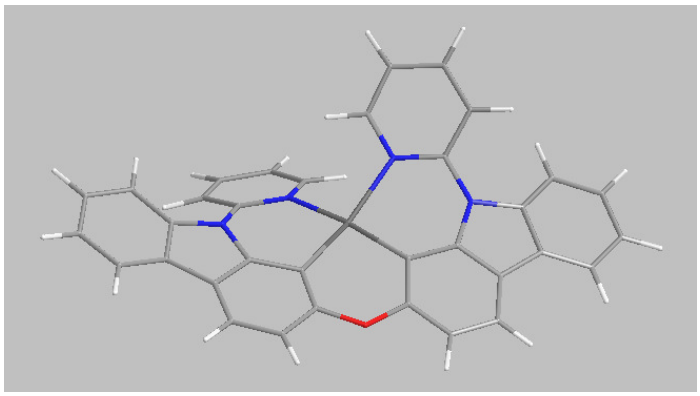

Figure 63 Chemical 3D drawing of optimized molecular geometry for PtNON based on DFT calculation.

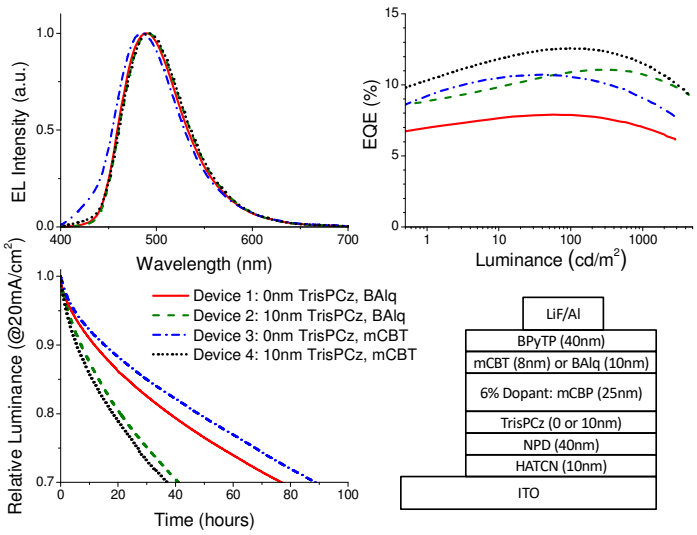


Figure 64 (a) Electroluminescent spectra, (b) external quantum efficiency versus luminance, c) device operational lifetime at a constant driving current of 20mA/cm$^2$, and d) an illustration of the structure for PtNON devices

Due to the electrochemical instability of the charge blocking materials TAPC and DPPS,[109] a new structure with stable host and transporting materials is necessary. Devices were fabricated in four operationally stable structures shown in Figure 64d.[110,113]

Device 1: HATCN/NPD/EML/BAlq/BPyTP/LiF/Al

Device 2: HATCN/NPD/TrisPCz/EML/BAlq/BPyTP/LiF/ Al

Device 3: HATCN/NPD/EML/mCBT/BPyTP/LiF/ Al

Device 4: HATCN/NPD/TrisPCz/EML/mCBT/BPyTP/LiF/ Al

Where the EML is 6% PtNON:mCBP and TrisPCz is 9,9′,9″-triphenyl-9H,9′H,9″H-3,3′:6′3″-tercarbazole, mCBP is 3,3-Di(9H-carbazol-9-yl)biphenyl, BAlq is bis(2-methyl-8-quinolinolato) (biphenyl-4-olato)aluminum, mCBT is 9,9′-(2,8-dibenzothiophenediyl)bis-9*H*-carbazole, and BpyTP is 2,7-di(2,2′-bipyridin-5-yl)triphenylene. The chemical structure, the estimated triplet energy, the HOMO and LUMO energy levels of each selected functional materials are also provided in the

supplemental materials (Figure 65).

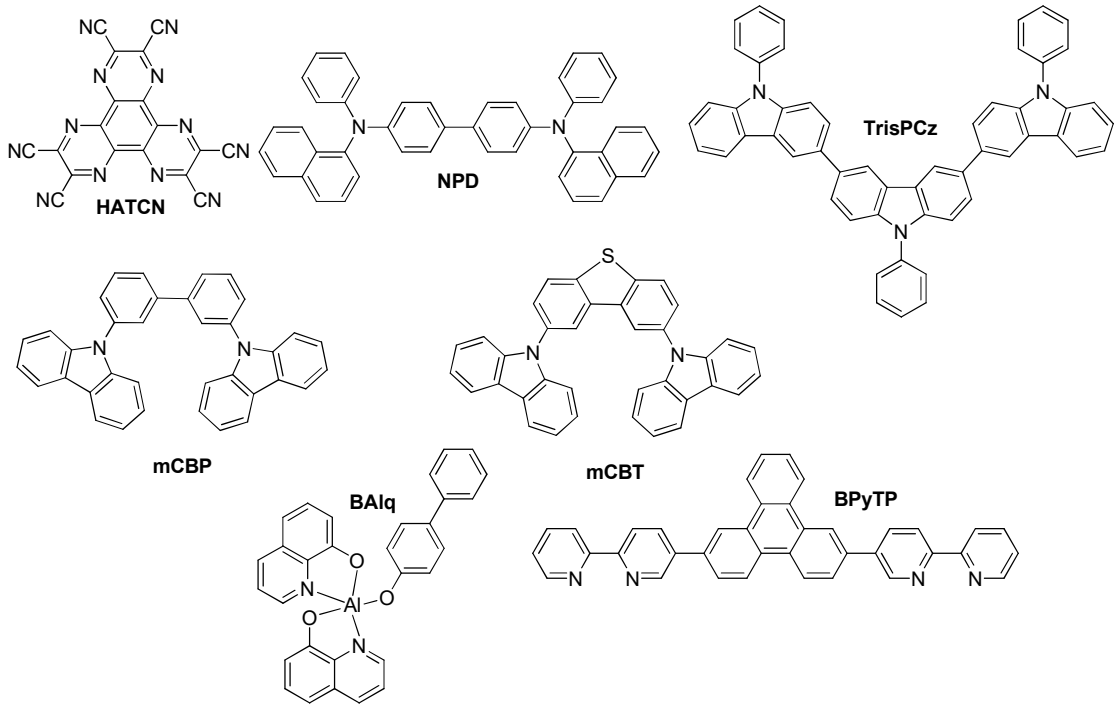


| Material | LUMO(eV) | HOMO (eV) | $E_T$ (eV) |
|---|---|---|---|
| **HATCN** | -5.5 | -9.5 | |
| **NPD** | -2.4 | -5.5 | 2.3 |
| **TrisPCz** | -2.1 | -5.6 | 2.7 |
| **mCBP** | -2.4 | -6.0 | 2.9 |
| **mCBT** | -2.5 | -6.0 | 2.9 |
| **Balq** | -2.6 | -5.6 | |
| **BPyTP** | -2.7 | -5.7 | |
| **PtNON** | -2.6 | -5.5 | -2.83 |

Figure 65 Chemical structures (top) and energy levels of selected materials (bottom) used in this study. The HOMO and LUMO enegy levels of PtNON were based on the redox values measured in the solution of DMF. $E_{ox}$ = 0.37V and $E_{red}$ = -2.47 V vs $Fc/Fc^+$.

Device 1, which employs a stable device structure using a BAlq hole blocking layer, shows a dramatic drop in peak EQE to 7.9% (shown in Figure 64b) as is common for a non-blocked structure. However, upon adding a TrisPCz electron blocking layer, the efficiency increases to over 11%, due to improved charge confinement. Furthermore, by replacing BAlq with the higher bandgap mCBT layer, the peak EQE increases to 10.7%

and 12.6% for devices with and without a TrisPCz layer. This can possibly be attributed to the enhanced exciton blocking capabilities of the mCBT material. Nevertheless, the efficiencies of all the stable devices are much lower than the intial exciton confining structure, as a result of exciton quenching at either electron or hole blocking layers; a persistent problem in OLEDs with emitters of such high triplet energies. The EL spectra are approximately the same for all the devices with the exception of Device 3 which showed increased emission between 400-425nm, attributed to emission from the BPyTP layer caused by hole leakage through the mCBT layer. Due to the broad emission character, the color coordinates of $CIE_x$= 0.17±0.01, $CIE_y$= 0.39±0.01 lie within the sky blue region of the visible spectrum which are slightly less blue than those of the efficient device structure and can be attributed to subtle changes in the interaction with the host matrix.[170]

PtNON devices driven at a constant current of 20mA/cm$^2$ until 70% of their initial luminance ($LT_{70}$) is reached. The initial voltage at 20mA/cm$^2$ was between 6.0V and 6.3V for all four devices. Device 1 had an $LT_{70}$ of 77 h at an initial luminance ($L_0$) of 2820 cd/m$^2$. This approximately corresponds to 550 h at 1000cd/m$^2$ and 22,500 h at 100cd/m$^2$ using the using the formula $LT(L_1)=LT(L_0)(L_0/L_1)^{1.7}$ where $L_1$ is the desired luminance of 1000 or 100 cd/m$^2$.[24] The addition of TrisPCz nearly halves the nominal lifetime to 41h for Device 2 but the higher initial brightness of 4393 cd/m$^2$ results in a slight increase in the estimated lifetimes for practical luminances. Replacement of BAlq with mCBT led to the most significant increase in lifetime with a nominal value of 89h. at an initial luminance of 3145 cd/m$^2$ resulting in estimated lifetimes of 624h. at 100cd/m$^2$ and over 30,000h. at 100cd/m$^2$. It is extremely encouraging that such long

operational lifetimes can be achieved for PtNON despite the emitter's intrinsically high triplet energy. The achievement of both over 10% external quantum efficiency and $LT_{70}$ over 30,000 hours at a practical luminance of 100cd/m$^2$ for blue devices is a substantial improvement over any other previously reported blue device.[150]

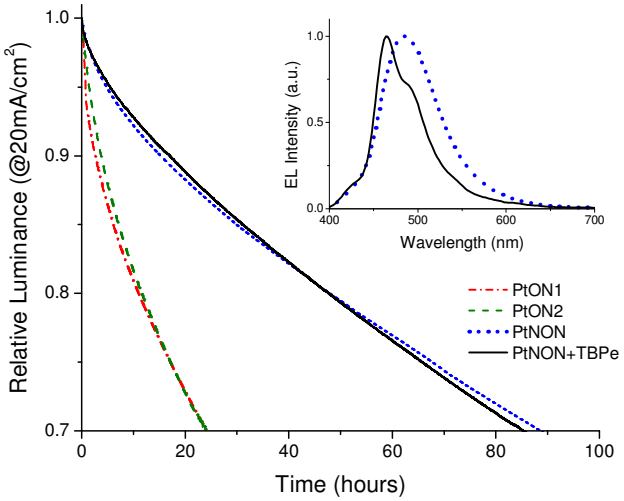


Figure 66 Electroluminescent intensity versus operational time at a constant driving current of 20mA/cm$^2$ for devices of PtON1, PtON2, PtNON, and a codoped device with 6% PtNON and 1% TBPe in the structure ITO/HATCN/NPD/6% dopant: mCBP/mCBT/BPyTP/LiF/Al. The EL spectra of PtNON device and a codoped PtNON:TBPe (6%:1%) device are given in the inset.

To further illustrate the significance of this improvement, comparison devices employing the efficient deep blue and sky blue emitters, PtON1 and PtON2, were fabricated in same structure as Device 3.[105] The efficiencies of both these devices were substantially lower than all of those employing PtNON (Table 7). This is likely due to poor charge confinement or poor charge trapping for these emitters. Nominal lifetimes of only 24h. were achieved for both PtON1 ($L_0$=787 cd/m$^2$) and PtON2 ($L_0$=1490 cd/m$^2$) resulting in estimated lifetimes at 100 cd/m$^2$ that were 10 to 30 times lower than those of PtNON (Figure 67). Application of these emitters in the other stable structures showed similarly

low device operational lifetimes (Supporting Information). The device operational lifetimes for PtNON are also much greater than those for the previously reported blue device employing Pt7O7 which achieved an $LT_{70}$ of only 39hrs at 650 cd/m$^2$. These results clarify the importance of emitter design to acheive long operational stabilities. Further optimization of the structure for PtNON devices may improve both the efficiency and operational lifetimes even further.[171]

Table 7 Device performance of PtNON, PtON1, and PtON2

| | | | EQE (%) | | | | Lifetime (hours) | | |
|---|---|---|---|---|---|---|---|---|---|
| Device | Dopant | CIE | Peak | 100cd/m$^2$ | 1000cd/m$^2$ | Lo (cd/m$^2$) | L= $L_0$ | L=1000cd/m$^2$ | L=100cd/m$^2$ |
| 1 | PtNON | (0.17, 0.38) | 7.9 | 7.9 | 7 | 2820 | 77 | 449 | 22486 |
| 2 | PtNON | (0.18, 0.40) | 11.1 | 10.9 | 10.8 | 4393 | 41 | 508 | 25438 |
| 3 | PtNON | (0.17, 0.32) | 10.7 | 10.5 | 9.1 | 3145 | 89 | 624 | 31286 |
| 4 | PtNON | (0.18, 0.39) | 12.6 | 12.6 | 11.5 | 4381 | 37 | 456 | 22849 |
| 3 | PtON1 | (0.14, 0.18) | 3.2 | 3.2 | N/A | 787 | 24 | 16 | 801 |
| 3 | PtON2 | (0.16, 0.30) | 6.1 | 5.3 | 4.1 | 1490 | 24 | 47 | 2369 |
| 3 | PtNON | (0.15, 0.21) | 9.8 | 9.7 | 8.2 | 2257 | 85 | 340 | 16999 |

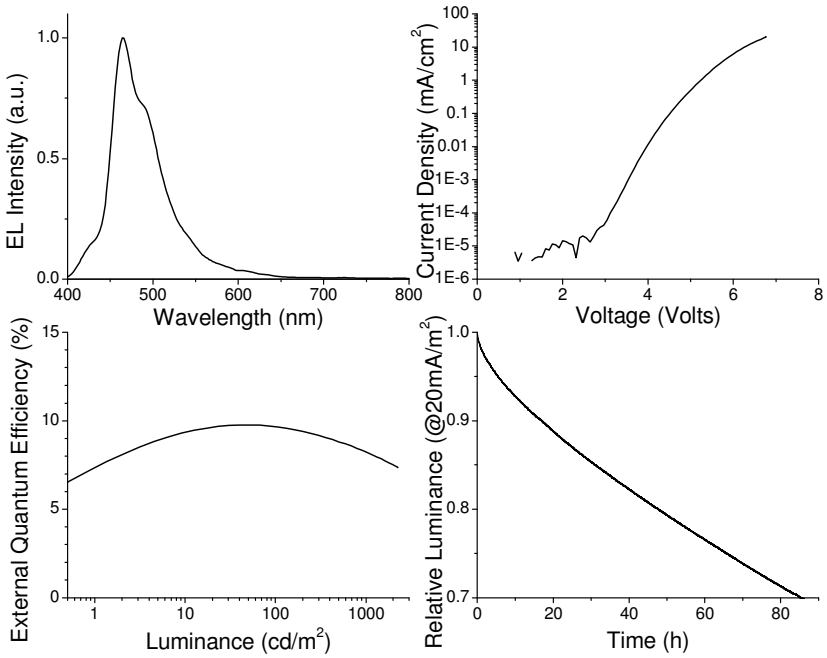


Figure 67 (a) Electroluminescent spectra, (b) current density versus voltage, (c) external quantum efficiency versus luminance and (d) electroluminescent intensity versus operational time at a constant driving current of 20mA/cm$^2$ for devices in the structure: HATCN/NPD/EML/mCBT/BPyTP/LiF/Al where the EML is: 6% PtNON and 1% TBPe codoped in mCBP.

Despite the high triplet energy of PtNON, the broad and red-shifted emission at room temperature prevents PtNON from being effective as an emitter for deep blue OLEDs. However, PtNON can be used to harvest triplet excitons with and subsequently transfer the energy to a fluorescent emitter with high emission energy.[172] Devices were fabricated in the same structure of Device 3 with an EML consisting of mCBP doped with 6% PtNON and 1% 2,5,8,11-Tetra-tert-butylperylene (TBPe), a known efficient fluorescent blue emitter.[173] As shown in Figure 4, the EL spectrum takes on the narrow blue emission character of the fluorescent emitter rather than the broad emission characteristics of PtNON, indicating effective energy transfer to the fluorescent dopant. The emission peak shifts to 464nm yielding blue emission with CIE coordinates of (0.15,0.21). This

dramatic shift in color is achieved while maintaining similar efficiencies with a peak at 9.8% and remaining at 8.2% at 1000cd/m$^2$ (Figure 67). The similar efficiencies suggest that PtNON is still effectively harvesting the triplet excitons then transferring the energy to the TBPe molecules. Such a strategy highlights the utility of the high triplet energy of PtNON to be compatible with a deep blue fluorescent emitter. Furthermore, the operational lifetime of this device was also measured at an accelerated constant driving current of 20mA/cm$^2$. The $LT_{70}$ of the co-doped device was 85h. at an $L_0$=2257cd/m$^2$ corresponding to nearly 17,000 h. at 100cd/m$^2$. Further manipulation of the EML to modify the exciton harvesting and energy transfer process may yield even greater efficiencies and lifetime. Furthermore, the emission color in this structure can be easily tuned through the use of various other known fluorescent emitters, thus, this strategy remains an active research focus.

4.2.4 Tetradentate Pd(II) complexes for efficient blue OLEDs

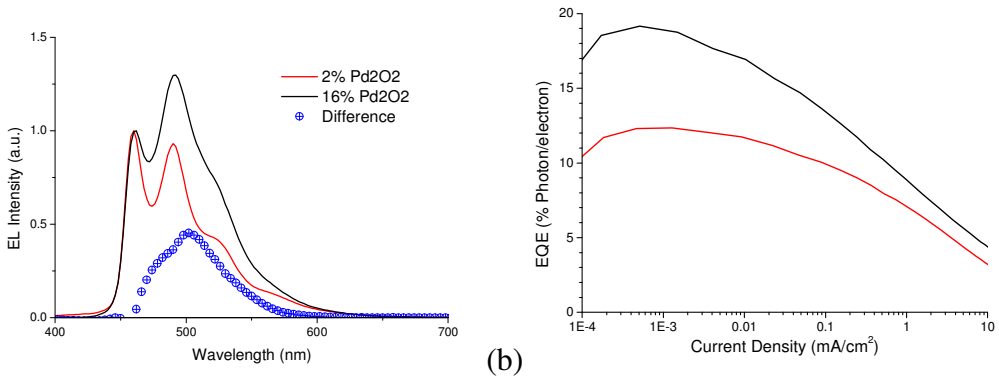


(a) (b)

Figure 68 (a) EL spectra for 2% Pd2O2(red), 16% Pd2O2(black), and the difference (blue circles) and (b) external quantum efficiency vs. current density for the device ITO/HATCN(10 nm)/NPD(40 nm)/TAPC(10nm)/ x% Pd2O2:26mCPy (25 nm)/DPPS(10 nm)/BmPyPB(30 nm)/LiF/Al.

Devices employing Pd2O2 were fabricated in the structure HATCN/NPD/TAPC/ x% Pd2O2:26mCPy/ DPPS/ BmPyPb/ LiF/ Al for dopant concentrations of 2% and 16%

with results shown in Figure 68. The devices exhibited peak external quantum efficiencies of 12.3% and 19.1% for the 2% doped and 16% doped devices which are among the highest reported for OLEDs employing palladium emitters. When the concentration increases there is significant broadening and a dramatic increase in the intensity of a peak centered at about 500nm relative to the monomer emission. This is illustrated by taking the difference between the two emission spectra which shows a broad increase in emission spectrum between 450 and 550 indicating the presence of excimer formation, which emits at 500nm at the elevated concentration. The high energy of the excimer species and the low intensity at such a high concentration may be related to the palladium metal center and is under continued investigation.

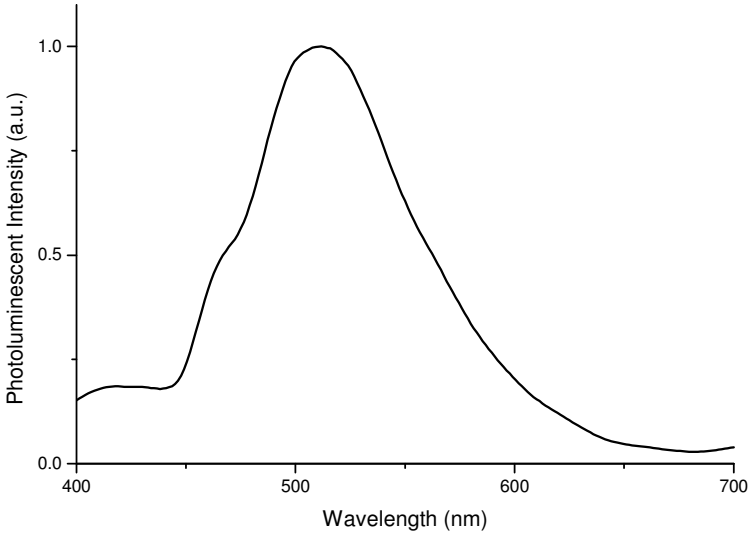


Figure 69 Emission spectrum of 50% Pd2O2 doped 26mCPy film at room temperature.

To further illustrate the existence of excimer emission in the devices, the photoluminescence emission spectrum of a thin film of 50% Pd2O2 doped in 26mCPy is shown in Figure 69. It is apparent that at these very high concentrations, the broad

emission is almost exclusively from excimer emitting species peaking at 500nm, where the small shoulder between 400-450nm is likely due to poor energy transfer to the high energy Pd2O2 complex at such high concentrations. These results demonstrate the potential for Pd complexes to be used as effecting emitters for single doped white OLEDs and are particularly encouraging for their deep blue emission properties.

Conclusion

tetradentate platinum and palladium complexes as  deep blue emission materials. The platinum complex PtNON, achieved a peak external quantum efficiency of 24.4 % and CIE coordinates of (0.18, 0.31) in a device structure designed for charge confinement and the palladium complexes Pd2O2 exhibited peak external quantum efficiency of up to 19.2%. which are among the highest reported for OLEDs employing palladium emitters

REFERENCES


1.J. Nelson, The physics of Solar Cell, imperial College Press, 2003

2.B. G. Gregg, Phys. Chem. B 2003, 107, 4688-4698

3.M.A. Green. K. Emery, Y. Hishikawa, W. Warta, E.D. Dunlop. prog. Photovolt: Res. Appl. 2016; 24:905–913

4.J. Nelson, Curr. Opinion Solid State Mater. Sci. 2002, 6, 87

5.G. Yu, J. Gao, J. C. Hummelen, F. Wudl, A. J. Heeger, Science 1995, 270, 1789-1791.

6.J. J. M. Halls, C. A. Walsh, N. C. Greenham, E. A. Marseglia, R. H. Friend, S. C. Moratti, A. B. Holmes, Nature 1995, 376,498.

7.S. E. Gledhill, B. Scott, B. A. Gregg, J. Mater. Res. 2005, 20 3167–3179

8.J. M. Nunzi, .Physique 2002, 3, 523

9.C. J. Brabec, G. Zerza, G. Cerullo, S. D. Silvestri, S. Luzzati, J. C. Hummelen, S. Sariciftci. Chem. Phys. Lett. 2001, 340, 232-236

10.E. V. Emelianova, M. van der Auweraer, and H. Bässlerhys. J. Chem. Phys. 2003, 119, 3952.

11.M. C. Scharber, D. Mühlbacher, M. Koppe, P. Denk, C. Waldauf, A. J. Heeger, C. J. Brabec. Adv. Mater. 2006, 18, 789-794 .

12.Y.Y. Liang, L. P. Yu, Acc. Chem. Res. 2010, 43, 1227-1236

13.Y-J. Cheng, S-H. Yang, C- Hsu, Chem. Rev. 2009, 109, 5868-5923

14.Y.Y. Liang, L. P. Yu,. Polym. Rev. 2010, 50, 454-473

15.D. Chen, F. Liu, C. Wang, A. Nakahara, T. P. Russell, Nano Lett. 2011, 11, 2071-2078

16.J. H. Seo, A. Gutacker, Y. Sun, H.B. Wu, F. Huang, Y. Cao, U. Scherf, A. J. Heeger, G. C. Bazan, J. Am. Chem. Soc. 2011, 133, 8416–8419

17.L. Huo, J. Hou, S. Zhang, H.-Y. Chen, Y. Yang, Angew. Chem. 2010, 122, 1542 –1545

18.Y. Y. Liang, Y. Wu, D. Feng, S.-T. Tsai, H.-J. Son, G. Li, L.P. Yu,. J. Am. Chem. Soc. 2009, 131, 56–57

19.P. Peumans, S. R. Forrest. Appl. Phys. Lett. 2001, 79, 126

20.Y. Yao, C Shi, G. Li, V. Shrotriya, Q. Pei, Y. Yang, Appl. Phys. Lett. 2006, 88, 153507

21.I. Kim, H. M. Haverinen, Z. Wang, S. Madakuni, Y. Kim, J. Li, G. E. Jabbour, Chem. Mater. 2009, 21, 4256–4260

22.I. Kim, H. M. Haverinen, J Li, G. E. Jabbour, Appl. Mater. Interfaces 2010, 2, 1390

23.C. W. Tang, A. C. Albrecht, J. Chem. Phys. 1975, 62, 2139

24.Onsager, L. Phys. Rev. 1938, 54, 554.

25.J. Xue, S. Uchida, B. P. Rand, S. R. ForrestAppl. Phys. Lett. 2004, 84, 3013

26. J. Xue, B. P. Rand, S. Uchida, Stephen R. Forrest. Adv. Mater. 2005, 17, 66.

27.K. L. Mutolo, E. I. Mayo ,B. P. Rand ,S. R. Forrest, M. E. Thompson, J. Am. Chem. Soc. 2006, 128, 8108-8109

28.J. Meiss, A. Merten, M. Hein, C. Schuenemann, S. Schäfer, M. Tietze, C. Uhrich, M. Pfeiffer, K. Leo, M. Riede, Adv. Funct. Mater. 2012, 22, 405–414

29.Mertens, R. In The OLED Handbook; Metalgrass: Herzerlia, Israel, 2011; , pp 106.

30.C. W. Tang, Appl. Phys. Lett. 1987, 51, 913

31.Fukuda M., Sawada K., Morita S., Yoshino K., Synthetic Metals, 41 (1991) 855.

32.T. Forster,. Discussions of the Faraday Society, 1959,27, 7-17

33.M. A. Baldo, S. R. Forrest, Physical Review B, 2000, 62, 10958

34.V. Adamovich, J. Brooks, A. Tamayo, A. M. Alexander, P. I. Djurovich, B. W. D' Andrade, C. Adachi, S. R. Forrest, M. E. Thompson, New J. Chem. 2002, 26, 1171

35.B.W. D' Andrade, J. Brooks, V. Adamovich,; M.E. Thompson; S.R. Forrest, Adv. Mater. 2002, 14, 1032-1036;

36.T. Fleetham,; J. Ecton; Z. Wang; N. Bakken, J. Li, Adv. Mater. 2013, 25, 2573–2576

37.C. W. Tang, Appl Phys Lett, 1986, 48:183

38.F. Padinger, R. S Rittberger, N. S. Sariciftci, Adv Funct Mater, 2003, 13:85

39.S. Reineke, F. Lindner, G. Schwartz, N. Seidler, K. Walzer, B. Lüssem, K. Leo, Nature, 2009, 459, 234

40. P. Peumans, S. R. Forrest, Appl. Phys. Lett. ,2001, 79, 126

41. S. Mathew, A.Yella, P. Gao, R. H. Baker, B. F. E. Curchod, N. Ashari-Astani, I. Tavernelli, U. Rothlisberger, M. K. Nazeeruddin, M. Grätzel, Nature Chemistry 2014, 6, 242–247

42.A. Yella1, H.-W. Lee, H. N. Tsao, C. Yi, A. K. Chandiran, M..K. Nazeeruddin, E. W. G. D, C.-Y Yeh, S. M. Zakeeruddin, M. Grätzel1, Science , 2011, 334,629-634:

43.Y. Xie,Y. Tang, W. Wu, Y. Wang, J. Liu, X. Li, H. Tian, W.-H. Zhu, .J. Am. Chem. Soc., 2015, 137 (44), 14055–14058

44.P. A. Barrett, R. P. Linstead; G. A. P. Tuey, J. M. Robertson, J. Chem. Soc. 1939, 1809−1820

45.P.A. Barrett, J. Chem. Soc. 1940, 1079-1092

46.C C. Leznoff, N B. McKeown, J. Org. Chem. 1990, 55, 2186-2190

47.N. E. Galanin , L. A. Yakubov, G. P. Shaposhnikov, Russ. J. Org. Chem. 2009, 45, 1024–1030;

48.N. E. Galanin, E. V. Kudrik, G. P. Shaposhnikov, Russ. Chem. Bull. 2008, 57, 1595–1610

49. N. E. Gala- nin, L. A. Yakubov, G. P. Shaposhnikov, Russ. J. Gen. Chem. 2008, 78, 1802–1807

50.L. A. Yakubov, N. E. Galanin, G. P. Shaposhnikov, N. S. Lebedeva, E. A. Mal'kova, Russ. J. Gen. Chem. 2008, 78, 1255– 1259;

51.A. N. Cammidge, I. Chambrier, M. J. Cook, D. L. Hughes, M. Rahman, L. Sosa-Vargas, Chem. Eur. J. 2011, 17, 3136 – 3146

52.W. J. Youngblood, J. Org. Chem., 2006, 71, 3345

53.J. Alzeer, P. J. C. Rotha, N. W. Luedtke, Chem. Commun., 2009, 1970–1971

54.E. D. Becker and R. B. Bradley, J. Chem. Phys., 1959, 31, 1413.

55.Esposito, J. N.; Sutton, L. E.; Kenney, M. E. Inorg. Chem. 1967,6, 1116.

56. Janson, T. R.; Kane, A. R.; Sullivan, J. F.; Knox, K.; Kenney, M. E. J. Am. Chem. Soc. 1969, 91, 5210;

57. Maskasky, J. E.; Mooney, J. R.; Kenney, M. E. J. Am. Chem. Soc.1972, 94, 2132..

58.Koyama, T.; Suzuki, T.; Hanabusa, K.; Shirai, H.; Kobayashi, N.Inorg. Chim. Acta 1994, 218, 41.

59. M. A. Filatov, A. V. Cheprakov, I. P. Beletskaya, Eur. J. Org. Chem. 2007, 3468–3475

60.Kevin M. Smith, Porphyrins and Metalloporphyrins, Elsevier Science Ltd, New York, 1975

61.N. Kobayashi,; M. Togashi,; T. Osa,; K. Ishii,; S. Yamauchi,; H. Hino. J. Am. Chem. Soc. 1996, 118, 1073

62.I. Kim,; H. M. Haverinen,; J. Li,; G. E. Jabbour,. Appl. Mater. Interfaces 2010, 2, 1390-1394

63.Y. Shao; Y. Yang, Adv. Mater. 2005, 17, 2841.

64.I. Kim; H. M. Haverinen,; Z. Wang,; S. Madakuni,; Y. Kim, J. Li,; G. E. Jabbour, Chem. Mater. 2009, 21, 4256-4260

65.J. G. Bunzli and S. V. Eliseeva, J. of Rare Earths 2010, 28 (6), 824-842

66.S. M. Borisov, G. Zenkl, and I. Klimant, ACS Appli.Mater. & Interfaces 2010, 2 (2), 366-374 .

67.B. Wang, L. Zhang, B. Li, Y. Li, Y. Shi, T. Shi, Sens. and Actuat. B: Chemical 2013, 190, 93-100

68.Z. Q. Chen, F. Ding, Z. Q. Bian, C. H. Huang, Org. Elect. 2010, 11 (3), 369-376

69.E. L. Williams, J. Li, and G. E. Jabbour, App. Phys. Lett. 2006, 89 (8), 083506

70. Y. Xuan, G. Qian, Z. Wang, D. Ma, Thin Sol. Films 2008, 516 (21), 7891-7893

71.C. Borek, K. Hanson, P. I Djurovich, M. E. Thompson, K. Aznavour, R. Bau, Y. Sun, S. R. Forrest, J. Brooks, L. Michalski et al., Angew. Chemie 2007, 119 (7), 1127-1130

72.S. M. Borisov, G. Nuss, W. Haas, R. Saf, M. Schmuck, I. Klimant, J. of Photochem. and Photobio. A: Chem. 2009, 201, 128-135

73.N. Su, F. Meng, J. Chen, Y. Wang, H. Tan, S. Su, W. Zhu, Dyes and Pig. 2016, 128, 68-74 .

74.Y. Sun, C. Borek, K. Hanson, P. I. Djurovich, M. E. Thompson, J. Brooks, J. J. Brown, S. R. Forrest, Appl. Phys. Lett. 2007, 90 (21), 213503

75.E. Rossi, L. Murphy, P. L. Brothwood, A. Colombo, C. Dragnetti, D. Roberto, R. Ugo, M. Cocchi, J. A. G. Williams, J. Mater. Chem., 2011, 21, 15501-15510

76.S. Kesarkar, W. Mróz, M. Penconi, M. Pasini, S. Destri, M. Cazzaniga, D. Ceresoli, P. R. Mussini, C. Baldoli, U. Giovanella, et al., Ange. Chemie 128 (8), 2016, 2764-2768

77.H. Y. Chen, C. H. Yang, Y. Chi, Y. M. Cheng, Y. S. Yeh, P. T. Chou, H. Y. Hsieh, C. S. Liu, S. M. Peng, G. H. Lee, Can. J. Chem. 2006, 84, 309-318

78.J. L. Liao, Y. Chi, S. H. Liu, G. H. Lee, P. T. Chou, H. X. Huang, Y. D. Su, C. H. Chang, J. S. Lin, M. R. Tseng, Inorg. Chem., 2014, 53, 9366-9374

79.J. L. Liao, Y. Chi, C. C. Yeh, H. C. Kao, C. H. Chang, M. A. Fox, P. J. Low, G. H. Lee, J. Mater. Chem. C, 2015, 3, 4910-4920

80.J. R. Sommer, R. T. Farley, K. R. Graham, Y. Yang, J. R. Reynolds, J. Xue, K. S. Schanze, ACS App. Mater. & Interfaces, 2009, 2, 274-278

81.T. C. Rosenow, K. Walzer, and K. Leo, J. of Appl. Phys. 2008, 4, 043105

82.F. So, J. Kido, P. Burrows, MRS Bull. 2008, 33, 663

83..-H. Jou, S.-M. Shen, C.-R. Lin, Y.-S. Wang, Y.-C. Chou, S.-Z. Chen, Y.-C. Jou, Org. Electron. 2011, 12, 865.

84. B.W. D'Andrade, R. J. Holmes, S. R. Forrest, Adv. Mater. 2004, 16, 624;

85. R. S. Deshpande, V. Bulovic, S. R. Forrest, Appl. Phys. Lett. 1999, 75, 888;

86. X. Gong, S. Wang, D. Moses, G. C. Bazan, A. J. Heeger, Adv. Mater. 2005, 17, 2053;

87.Y. Zhao, J. Chen, D. Ma, Appl. Phys. Lett. 2011, 99, 163303;

88. Y.-S. Park, J.-W. Kang, D. M. Kang, J.-W. Park, Y.-H. Kim, S.-K. Kwon, J.-J. Kim, Adv. Mater. 2008, 20, 1957;

89.H. Sasabe, J. Takamatsu, T. Motoyama, S. Watanabe, G. Wagenblast, N. Langer, O. Molt, E. Fuchs, C. Lennartz, J. Kido, Adv. Mater. 2010, 22, 5003.

90.Y. Sun, N. C. Giebink, H. Kanno, B. Ma, M. E. Thompson, S. R. Forrest, Nature 2006, 440, 908;

91. B.-P. Yan, C. C. C. Cheung, S. C. F. Kui, H.-F. Xiang, V. A. L. Roy, S.-J. Xu, C.-M. Che, Adv. Mater. 2007, 19, 3599;

92.G. Schwartz, M. Pfeiffer, S. Reineke, K. Walzer, K. Leo, Adv. Mater. 2007, 19, 3672;

93. G. Schwartz, S. Reineke, T. C. Rosenow, K. Walzer, K. Leo, Adv. Funct, Mater. 2009, 19, 1319.

94.S. Reineke, F. Lindner, G. Schwartz, N. Seidler, K. Walzer, B. Lüssem, K. Leo, Nature 2009, 459, 234

95.B.W. D'Andrade, M.E. Thompson, S.R. Forrest, Adv. Mater. 2002, 14, 147.

96.B. W. D'Andrade, S.R. Forrest, Adv. Mater. 2004, 16, 1585

97.J. Kalinowski, M. Cocchi, L. Murphy, J.A.G. Williams, V. Fattori, Chem. Phys. 2010, 378, 47;

98.S. C. F. Kui, P. K. Chow, G. S. M. Tong, S.-L. Lai, G. Cheng, C.-C. Kwok, K.-H. Low, M. Y. Ko, C.-M. Che, Chem Eur. J. 2013, 19, 69.

99.E.L. Williams, K. Haavisto, J. Li, G.E. Jabbour, Adv. Mater. 2007,19, 197

100.X. Yang, Z. Wang, S. Madakuni, J. Li, G. E. Jabbour, Adv. Mater. 2008, 20, 2405

101.N. Bakken, Z. Wang, J. Li, J. Photon. Energy 2012, 2, 021203

102.T. Fleetham, Z. Wang, J. Li, Org. Electon. 2012, 13, 1430

103. N. C. Giebink, B. W. DAndrade, M. S. Weaver, P. B. Mackenzie, J. J. Brown, M. E. Thompson, S. R. Forrest, J. Appl. Phys. 2008, 103, 044501

104.V. Sivasubramaniam, F. Brodkorb, S. Hanning, H. P. Loebl, V. Elsbergen, H. Boerner, U. Scherf, M. Kreyenschmidt, J. Fluorine Chem. 2009,130, 640.

105.J. Ecton, T. Fleetham, X. Hang, J. Li, SID Int. Symp. Dig. Tec. 2013, 44, 152

106.G. Li, T. Fleetham, J. Li, Adv. Mater. 2014, 18, 2931–2936

107.E. Turner, N. Bakken, J. Li, Inorg. Chem.2013,52, 7344

108.M. Segal, C. Mulder, K. Celebi, M. Singh, K. Rivoire, S. Difley, T. Van Voorhis, M.A. Baldo, Proc. SPIE, 6999 2008, 699912-1

109.X. Hang, T. Fleetham, E. Turner, J. Brooks, J. Li, Angew. Chemie. Int. Ed. 2013, 52, 6753-6756.

110.R.C. Kwong, M.R. Nugent, L. Michalski, T. Ngo, K. Rajan, Y-J. Tung, M. S. Weaver, T.X. Zhou, M. Hack, M.E. Thompson, S.R. Forrest, J. J. Brown, Appl. Phys. Lett. 2002, 81, 162

111.Féry, C., Racine, B., Vaufrey, D., Doyeux, H., Cinà S. Appl. Phys. Lett. 2005, 87, 213502.

112.Fukagawa, H., Shimizu, T., Hanashima, H., Osada, Y., Suzuki, M., Fujikake, H., Adv. Mater. 2012, 24, 5099

113.H. Nakanotani, K. Masui, J. Nishide, T.Shibata, C. Adachi, Sci. Rep. 2013, 3, 2127.

114.B. Ma , J. Li , P. I. Djurovich , M. Yousufuddin , R. Bau , M. E. Thompson, J. Am. Chem. Soc. 2005, 127, 28-29

115.R. Wang, D. Liu, H. Ren, T. Zhang, H. Yin, G. Liu, J. Li, Adv. Mater. 2011, 23, 2823

116.P. K. Chow, C. Ma, W.-P. To, G. S. M. Tong, S.-L. Lai, S. C. F. Kui, W.-M. Kwok, C.-M. Che, Angew. Chem. Int. Ed. 2013, 52, 11775 –11779;

117.K. Li, G. Cheng, C. Ma, X. Guan, W.-M. Kwok, Y. Chen, W. Lu, C.-M. Che, Chem. Sci. 2013, 4, 2630-2644

118.Z.-Q. Zhu, T. Fleetham, E. Turner, J. Li, Adv. Mater. 2015, 15, 2533–2537

119.S.-W. Lai, T.-C. Cheung, M. C. W. Chan, K.-K. Cheung, S.-M.Peng, C.-M. Che, Inorg. Chem. 2000, 39, 255 – 262;

120.S. Roy, S. Pramanik, T. Ghorui, K. Pramanik, RSC Adv. 2015, 5, 22544-22559

121.T. Fleetham, L. Haung, J. Li, Adv. Funct. Mater. 2014, 24, 6066-6073

122.E. Turner, N. Bakken, J. Li, Inorg. Chem. 2013, 52, 7344-7351

123.S. J. Farley, D. L. Rochester, A. L. Thompson, J. A. K. Howard, J. A. G. Williams, Inorg. Chem. 2005, 44, 9690–9703

124.G. Li, T. Fleetham, E. Turner, X.-C. Hang, J. Li, Adv. Opt. Mater. 2015, 3, 390–397

125.T. Higuchi, H. Nakanotani, C. Adachi, Adv. Mater. 2015, 27, 2019–2023

126.J. Kido, M. Kimura, K. Nagai, Science. 1995, 267 1332–1334

127.M.C. Gather, A. Köhnen, A. Falcou, H. Becker, K. Meerholz , Adv. Funct. Mater. 2007, 17 191–200

128.Y.-L. Chang, Y. Song, Z. Wang, M.G. Helander, J. Qiu, L. Chai, et al., Adv. Funct. Mater, 2013, 23, 705–712

129.R. Wang, D. Liu, H. Ren, T. Zhang, H. Yin, G. Liu, et al Adv. Mater. 2011. 23, 2823–2827

130.Chen, G. Tan, W.-Y. Wong, H.-S. Kwok, Adv. Funct. Mater. 2013, 21, 3785–3793

131.Q. Wang, J. Ding, D. Ma, Y. Cheng, L. Wang, F. Wang, Adv. Mater. 2009, 21, 2397–2401

132.Y. Sun, N.C. Giebink, H. Kanno, B. Ma, M.E. Thompson, S.R. Forrest, , Nature. 2006, 440 908–912.

133.Y.-L. Chang, Z.B. Wang, M.G. Helander, J. Qiu, D.P. Puzzo, Z.H. Lu , Organic Electronics. 2012, 13, 925–931

134.J.-K. Bin, N.-S. Cho, J.-I. Hong,, Adv. Mater. 2012, 24, 2911–2915

135.D. Volz, M. Wallesch, C. Fléchon, M. Danz, A. Verma, J.M. Navarro, et al., Green Chem. 2015, 17, 1988–2011

136.J. Kalinowski, V. Fattori, M. Cocchi, J. A. G. Williams, Coord. Chem. Rev. 2011, 255, 2401

137.K. Li, G. Cheng, C. Ma, X. Guan, W.-M. Kwok, Y. Chen, et al.,Chemical Science. 2013, 4 ,2630

138.X. Wang, Y.-L. Chang, J.-S. Lu, T. Zhang, Z.-H. Lu, S. Wang, Adv. Funct. Mater. 2013, 1911-1927

139.Y. Ohno, Opt. Eng. 2005, 44 , 111302

140.H. Ries, I. Leike, J. Muschaweck, Opt. Eng. 2004 , 43 , 1531–1536

141.M. A. Baldo, D. F. O'Brien, Y. You, A. Shoustikov, S. Sibley, M. E. Thompson and S. R. Forrest, Nature, 1998, 395, 151-154;

142.S. Lamansky, P. Djurovich, D. Murphy, F. Abdel-Razzaq, R. Kwong, I. Tsyba, M. Bortz, B. Mui, R. Bau, M. E. Thompson, Inorg. Chem. 2001, 40, 1704;

143.J. Brooks, Y. Babayan, S. Lamansky, P. I. Djurovich, I. Tsyba, R. Bau, M. E. Thompson, Inorg. Chem. 2002, 41, 3055

144.M. A. Baldo and D. F. O'Brien, M. E. Thompson, S. R. Forrest, Phys. Rev. B, 1999, 60, 14422-14428

145.C. Adachi, M. A. Baldo, M. E. Thompson and S. R. Forrest, J. Appl. Phys, 2001, 90, 5048-5051;

146.K. Udagawa, H. Sasabe, C. Cai , J. Kido, Adv. Mater. 2014, 26, 5062–5066

147.C. W. Lee, J. Y. Lee, Adv. Mater. 2013, 25, 5450–5454

148.S.-Y. Kim, W.-I. Jeong, C. Mayr, Y.-S. Park, K.-H. Kim, J.-H. Lee, C.-K. Moon, W. Brütting, J.-J. Kim, Adv. Funct. Mater. 2013, 23, 3896-3900

149.D. H. Kim, N. S. Cho, H.-Y. Oh, J. H. Yang, W. S. Jeon, J. S. Park, M. C. Suh, J. H. Kwon, Adv. Mater. 2011, 23, 2721–2726

150.K. S. Yook, J. Y. Lee, Adv. Mater. 2012, 24, 3169-3190

151.S. Haneder, E. DaComo, J. Feldmann, J. M. Lupton, C. Lennartz, P. Erk, E. Fuchs, O. Molt, I. Munster, C. Schildknecht, G. Wagenblast, Adv. Mater. 2008, 20, 3325

152.C. -F Chang, Y. -M. Cheng, Y. Chi, Y. -C. Chiu, C. -C. Lin, G. -H. Lee, P. -T. Chou, C. -C. Chen, C. -H. Chang, C. -C. Wu, Angew. Chem. Int. Ed. 2008, 47, 4542;

153.S. O. Jeon , S. E. Jang , H. S. Son, J. Y. Lee, Adv. Mater. 2011, 23, 1436;

154.S. C. F. Kui, P. K. Chow, G. Cheng, C. -C. Kwok, C. L. Kwong, K. -H. Low, C. -M. Che, Chem. Comm. 2013, 49, 1497;

155.D. A. K. Vezzu, J. C. Deaton, J. S. Jones, L. Bartolotti, C. F. Harris, A. P. Marchetti, M. Kondakova, R. D. Pike, S. Huo, Inorg. Chem. 2010, 49, 5107;

156.K. Feng, C. Zuniga, Y. D. Zhang, D. Kim, S. Barlow, S. R. Marder, J. L. Bredas, M. Weck, Macromolecules 2009, 42, 6855.

157.T. Fleetham, G. Li, L. Wen, J. Li, Adv. Mater. 2014, 2, 7116-7121

158.S. Tokito, T. Iijima, Y. Suzuri, H. Kita, T. Tsuzuki, F. Sato, Appl. Phys. Lett. 2003, 83, 569;

159.R. J.Holmes, B. W. D.' Andrade, S. R.Forrest. ,X. Ren, J. Li, M. E.Thompson, Appl. Phys. Lett.2003, 83,3818;

160.X. Yang, F. Wu, H. Haverinen, J. Li, C. Cheng, G.E. Jabbour, Appl. Phys. Lett., 2011, 98, 033302

161.R. Seifert, I. Rabelo de Moraes, S. Scholz, M. C. Gather, B. Lussem, K. Leo, Org. Electron. 2013, 14, 115-123

162.V S. H. Kim, J. Jang, J. Y. Lee, Appl. Phys. Lett. 2007, 90, 203511;

163. Fukagawa, H., Shimizu, T., Hanashima, H., Osada, Y., Suzuki, M., Fujikake, H., Adv. Mater. 2012, 24, 5099

164.L., Xiao, S-J., Su, Y.,Agata, H., Lan, J., Kido, Adv. Mater. 2009, 21, 1271;

165.H. Sasabe, E. Gonmori,T. Chiba, Y.J. Li, D. Tanaka, S.-J. Su, T. Takeda, Y-J. Pu, K. Nakayama, J. Kido, Chem. Mater. 2008, 20, 5951;

166. N. Chopra, J. S. Swensen, E. Polikarpov, L. Cosimbescu, F. So, A. B. Padmaperuma, Appl. Phys. Lett. 2010, 97, 033304;

167.R. Meerheim, S. Scholz, S. Olthof, G. Schwartz, S. Reineke, K. Walzer, K. Leo, J. Appl. Phys. 2008, 104, 014510;

168. G. Li, J. Ecton, B. O'Brien, J. Li,, Org. Electon. 2014, 15, 1862-1867.

169. D. H. Kim, N. S. Cho, H.-Y. Oh, J. H. Yang, W. S. Jeon, J. S. Park, M. C. Suh, J. H. Kwon, Adv. Mater. 2011, 23, 2721–2726.

170.V. Bulović, R. Deshpande, M. E. Thompson, S. R. Forrest, Chem. Phys. Lett. 1999, 308, 317

171.Y. Zhang, J. Lee, S. R. Forrest, Nat. Comm. 2014, 5, 5008

172.M. A. Baldo, M. E. Thompson, S. R. Forrest, Nature, 2000, 403, 750-753

173.H. Nakanotani, T. Higuchi, T. Furukawa, K. Masui, K. Morimoto, M. Numata, H. Tanaka, Y. Sagara, T. Yasuda, C. Adachi, Nat. Comm. 2014, 5, 4016